UNIVERSITY OF LONDON THESIS

Degree PhD Year 2006 Name of Author BELL
Thomas Alexander

COPYRIGHT

This is a thesis accepted for a Higher Degree of the University of London. It is an unpublished typescript and the copyright is held by the author. All persons consulting the thesis must read and abide by the Copyright Declaration below.

COPYRIGHT DECLARATION

I recognise that the copyright of the above-described thesis rests with the author and that no quotation from it or information derived from it may be published without the prior written consent of the author.

LOAN

Theses may not be lent to individuals, but the University Library may lend a copy to approved libraries within the United Kingdom, for consultation solely on the premises of those libraries. Application should be made to: The Theses Section, University of London Library, Senate House, Malet Street, London WC1E 7HU.

REPRODUCTION

University of London theses may not be reproduced without explicit written permission from the University of London Library. Enquiries should be addressed to the Theses Section of the Library. Regulations concerning reproduction vary according to the date of acceptance of the thesis and are listed below as guidelines.

A. Before 1962. Permission granted only upon the prior written consent of the author. (The University Library will provide addresses where possible).

B. 1962 - 1974. In many cases the author has agreed to permit copying upon completion of a Copyright Declaration.

C. 1975 - 1988. Most theses may be copied upon completion of a Copyright Declaration.

D. 1989 onwards. Most theses may be copied.

This thesis comes within category D.

☐ This copy has been deposited in the Library of _____

☐ This copy has been deposited in the University of London Library, Senate House, Malet Street, London WC1E 7HU.

Photon-Dominated Regions: Development of a Time-Dependent Model and Application to Astrophysical Problems

Thomas Alexander Bell

Thesis submitted for the Degree of Doctor of Philosophy
of the University of London

Department of Physics & Astronomy
UNIVERSITY COLLEGE LONDON

October 2006

ProQuest LLC
789 East Eisenhower Parkway
P.O. Box 1346
Ann Arbor, MI 48106-1346

I, Thomas Bell, confirm that the work presented in this thesis is my own. Where information has been derived from other sources, I confirm that this has been indicated in the thesis.

ABSTRACT

Photon-dominated regions occur in many regions of astrophysical interest and an understanding of their underlying chemical and physical processes can provide an insight into the conditions within them. This thesis describes the development and implementation of a time-dependent version of the UCL_PDR model, including comprehensive benchmarking as part of an international effort to understand the differences between individual models and improve their agreement in key areas.

The code has been applied to calculate theoretical values of the CO-to-H_2 conversion factor, X_{CO}, to investigate its sensitivity to physical parameter variation. X_{CO} is found to vary significantly from its canonical value under certain conditions and by over an order of magnitude in the case of high density or low metallicity. By fitting observed line intensity ratios in a sample of nearby galaxies, PDR models have been constructed to represent the conditions found in a range of galaxy types. These are used to derive appropriate values of X_{CO} for such objects and to investigate the possibility of using higher transition lines of CO as more reliable mass tracers in these environments.

A parameter space search has also been conducted using the model to look for conditions that produce significant column densities of H_2 with low levels of emission that would be undetectable or overlooked by current surveys. A plausible region of parameter space is found to produce such molecular dark matter, capable of concealing significant masses of gas that may form reservoirs for future star formation.

Additional applications of the UCL_PDR model are discussed, including a study of the chemistry within transient microstructure in the diffuse interstellar medium and models of the time-dependent expansion of a molecular shell around a massive star cluster, applied to observations of the central starburst in M 82.

ACKNOWLEDGEMENTS

There are many people I would like to thank for helping me to reach this point. First and foremost, I am indebted to my supervisor, Serena Viti, for her constant support and encouragement over the past three years, for replying to frantic emails at odd hours of the weekend, and for putting up with my near total lack of organisational skills. Without her help and guidance, I would never have reached this point. Similar thanks go to David Williams, who has encouraged me at every step of the way and has always found positive things to say about my efforts, even when they have been lacking. His advice has been invaluable and his kindness a great comfort in difficult times.

To all my friends, both at UCL and beyond, I owe too many thanks to fully express here. Suffice it to say, without your love, friendship and support, I would not have made it this far. You have made the last three years some of my happiest and I will always be grateful. Suffice it to say, too, that without your friendship, I would have surely finished this PhD much sooner; all those misspent hours in pubs, theatres, restaurants, gigs and so on I blame on you. But it has been fun. Always.

Finally, I would like to thank you, Mum and Dad, for never questioning my choices about what to make of my life, and for your unwavering encouragement, advice (even when I refused to take it) and love. And for always moaning at me to get a haircut.

CONTENTS

LIST OF FIGURES

LIST OF TABLES

CHAPTER 1

INTRODUCTION

1.1 Photon-dominated regions

The tenuous gas and dust that fills the space within galaxies shares a symbiotic relationship with its stellar inhabitants. It is this interstellar medium (ISM) that fuels the process of star formation, collapsing to the point of nuclear ignition and giving birth to stars, and it is these stars that shape and enrich the ISM, sculpting the gas and dust with their winds and radiation and yielding up their metal-rich content when they die. This complex and cyclic interaction between stars and their surroundings can lead to spectacular cosmic vistas (an example of which can be seen in Figure 1.1) and is ultimately responsible for the evolution of the galaxies in which they reside. An understanding of the processes at work within the ISM and, in particular, within regions of ongoing star formation can provide answers to questions such as, how is star formation initiated and regulated? where and when will it will occur? do stars form in isolation or in groups? and what distribution of stellar masses will be produced? On larger scales, the structure and dynamics of the ISM determines the overall star formation rate of the host galaxy and therefore its global properties.

One key aspect of this interaction is the role played by starlight in governing the physical and chemical structure of the ISM. Specifically, regions of predominantly neutral gas and dust that are illuminated by far-ultraviolet (FUV; $6 < h\nu < 13.6$ eV) radiation are referred to as *photon-dominated regions*[1] (PDRs). By studying PDRs, we hope to understand the effects of FUV photons on the chemistry, thermal balance and structure of the neutral ISM in galaxies. Since the bulk of the ISM is in neutral form, comprising the warm and cold neutral medium (WNM and CNM,

[1] The term "photodissociation regions" is also used to describe such phenomena; the preferred choice of nomenclature is somewhat arbitrary.

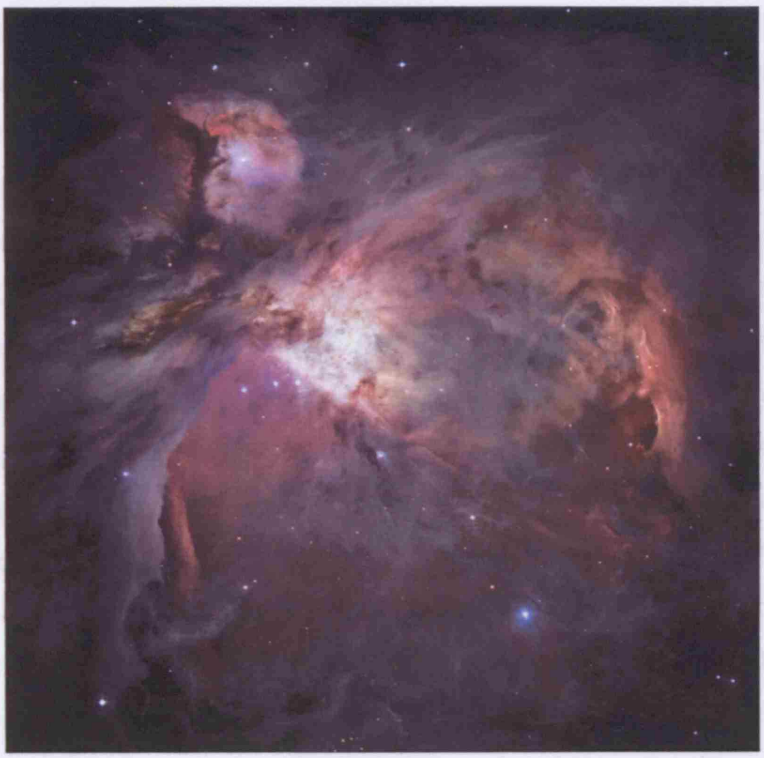

Figure 1.1: The Orion Nebula (M 42, NGC 1976). Colour composite mosaic obtained with the *Hubble Space Telescope* (*HST*) Advanced Camera for Surveys (ACS) and the ESO La Silla 2.2m. Colours are: Hα red/orange; z, i red; V green; B blue (ACS). Hα, [S II] red; [O III] green; B blue (La Silla). *Credit: NASA, ESA, M. Robberto (STSci/ESA).*

respectively) and the molecular clouds that are the birthplaces of stars, the study of PDRs can tell us much about the conditions within star-forming regions and help to answer some of the questions posed in the previous paragraph. PDRs are also responsible for much of the infrared emission from galaxies. Information about the gas and dust within a galaxy is encoded in that emission, which, if correctly interpreted, can divulge the conditions within these distant and often exotic objects. Note also that the source of the FUV photons need not be restricted to stars. The accretion of material onto supermassive black holes in active galactic nuclei (AGN) produces strong ultraviolet and X-ray emission that impacts the surrounding gas and dust, creating large PDRs, or their X-ray equivalent, *X-ray-dominated regions* (XDRs). Examination of these extreme environments can provide insight into the dynamics at their centres.

The study of PDRs has its origins in the absorption line studies of cool, dilute and fairly transparent regions called "diffuse interstellar clouds". From the beginning of the 20th century,

observations of optical absorption lines toward bright stars have revealed the presence of absorbing atoms (Na and Ca^+; Hartmann 1904; Heger 1919) and molecules (CH, CN and CH^+; Swings & Rosenfeld 1937; McKellar 1940; Douglas & Herzberg 1941, respectively) residing not in the stellar photospheres, but in the intervening material along the line of sight, the diffuse clouds. These observations prompted Bates & Spitzer (1951) to consider possible formation and destruction mechanisms for CH and CH^+, the first theoretical study of its kind. Thirty years later, rocket-based experiments and the launch of the *Copernicus* satellite in 1972 allowed the first observations of ultraviolet absorption lines in diffuse clouds and led to the discovery of rotationally excited molecular hydrogen (H_2), which was found to be abundant within the clouds (Carruthers 1970; Smith 1973; Spitzer et al. 1973; Spitzer & Jenkins 1975). The subsequent detection of other molecules in absorption, such as HD, CO, OH and C_2, added to the chemical inventory. Motivated by the wealth of observational data now available, theoretical models of diffuse clouds developed rapidly in the 1970s (Glassgold & Langer 1974, 1975; Black & Dalgarno 1976, 1977), building upon previous models of H_2 formation and destruction (e.g. Gould & Salpeter 1963; Stecher & Williams 1967; Hollenbach et al. 1971) and attempting to reproduce the observed abundances by considering the attenuation of the ultraviolet radiation, the heating and cooling of the gas and somewhat limited chemistry. Other models addressing the absorption studies of thicker "translucent clouds" considered a more complex chemistry, leading to the formation of polyatomic molecules.

Almost a decade later, observations of infrared (IR) emission from dense molecular clouds, opaque to UV and optical light, stimulated the study and modelling of PDRs present at their surfaces. In particular, airborne observations of the far-infrared (FIR) atomic fine structure lines [C II] 158 μm and [O I] 63 μm toward massive star-forming regions in the Orion Nebula (M42; Melnick et al. 1979; Storey et al. 1979; Russell et al. 1980) and Omega Nebula (M17; Melnick et al. 1979; Russell et al. 1981) showed strong emission in these lines at positions adjacent to H II regions. However, these lines were dwarfed by the extreme luminosity detected in the FIR continuum, resulting from the absorption and re-emission of starlight by dust. These mainly neutral, IR-luminous regions were therefore interpreted as being subject to FUV fluxes generated by nearby O stars[2]. With this in mind, Tielens & Hollenbach (1985a,b) constructed theoretical models of dense gas exposed to high FUV fluxes, applying them to the observations of the Orion PDR with

[2]Only massive O- and B-type stars emit photons capable of ionizing atomic hydrogen ($h\nu \geq 13.6$ eV, the Lyman limit). As a result, these stars create H II regions around them when embedded in their parent clouds. PDRs lie at the interface of these H II regions with the surrounding neutral gas, where absorption by ionized hydrogen has effectively removed all photons above the Lyman limit and only the FUV flux remains.

much success. Their models included an extensive network of chemical reactions and detailed treatment of the heating, cooling and emission within the gas. They were able to show that 0.1–1% of the FUV energy absorbed by dust grains produced energetic photoelectrons that were ejected from the grains, heating the gas and causing the intense emission observed in the fine structure lines as the gas tried to cool. This prompted further study of PDRs under a variety of conditions that were generally quite different from the diffuse light and gas that characterized early models (e.g. van Dishoeck & Black 1988; Sternberg & Dalgarno 1989; Hollenbach et al. 1991; Le Bourlot et al. 1993a; Sternberg & Dalgarno 1995; Kaufman et al. 1999; Le Petit et al. 2006).

The last twenty years has seen rapid growth in this area of research. Models are steadily growing in complexity, benefitting from increasingly accurate and extensive laboratory and theoretical data. Observations of the atomic fine structure and molecular lines within PDRs have been revolutionised by advances in FIR and submillimetre astronomy, the launch of the *Infrared Space Observatory* (*ISO*) in 1995 and first light on the James Clerk Maxwell Telescope (JCMT) in 1987 being just two of the milestones of this era. Together, these developments have paved the way for a greater understanding of the gaseous, dusty space that we inhabit.

PDRs represent a vast range of conditions that can be found in all reaches of space, from thin veils of gas and dust under the ambient glow of interstellar light to dense clouds caught in the glare of young, hot stars; from the natal cocoons surrounding newborn stars to the death throes of planetary nebulae in the harsh light of their central sources. Given such a diverse range of applications, PDR models are versatile tools indeed.

The work presented here concerns the development of a model capable of simulating the time-dependent evolution of photon-dominated regions and its application to relevant astrophysical problems. Chapter 2 describes the model and its participation in a recent benchmarking effort involving established PDR codes, presenting the outcome of a variety of test cases. The model is then used in Chapters 3 and 4 to examine the reliability of the CO-to-H_2 conversion factor, $X_{\rm CO}$, as a tracer of molecular mass and derive appropriate values of the conversion factor for specific galaxy types. The possibility of hidden molecular gas is addressed in Chapter 5, using the time-dependent PDR model to place constraints on the physical conditions such molecular dark matter might possess. Chapter 6 describes two other applications of the PDR code; an investigation of the time-dependent chemistry within diffuse interstellar microstructure and modelling of an expanding shell of gas and dust around a massive star cluster, applied to the starburst in M 82. Finally, some concluding remarks are made on the work as a whole in Chapter 7, with some proposals for its future direction.

The rest of this chapter is devoted to introducing the main features of PDRs and some of the important mechanisms at work within them, including a discussion of the typical chemistry arising in dense PDRs.

1.2 Physical and chemical processes in PDRs

The physical and chemical processes that determine the structure of photon-dominated regions are many and varied, but are all linked in some way to the incident far-ultraviolet radiation. The gas is thermally coupled to the FUV field, albeit rather indirectly, the chemistry is driven by photoionization and photodissocation reactions, and the radiative transfer of the FUV photons affects the survival of the two most important molecular species, H_2 and CO.

To a first approximation, the conditions within a PDR may be completely described by two key parameters; the number density of hydrogen nuclei in the cloud (in cm^{-3}) and the flux of FUV photons striking its surface (in erg s^{-1} cm^{-2}). The number density is given by $n = n(H) + 2n(H_2)$, where $n(H)$ and $n(H_2)$ are the number densities of atomic and molecular hydrogen, respectively. Densities in PDRs range from $n \approx 0.25$ cm^{-3} in the warm neutral medium to $n \gtrsim 10^7$ cm^{-3} in regions of massive star formation.

In an attempt to characterize the "typical" interstellar radiation field (ISRF), Habing (1968) observed O and B stars along many lines of sight and determined the average flux in the wavelength range 912 Å $< \lambda <$ 2400 Å to be 1.6×10^{-3} erg s^{-1} cm^{-2}. This standard radiation field has been adopted in the calculation of many quantities relevant to the study of PDRs and it is convenient to express the FUV flux in terms of the Habing field, multiplied by some factor G_0. The ultraviolet ISRF shortwards of 2000 Å given by Draine (1978) is also often used in PDR models, particularly when determining the rates of photoreactions, whose cross sections have been evaluated by integration over the spectral energy distribution (SED) of the Draine field. The average flux of the Draine field is related to that of the Habing field by $\chi = 1.7\,G_0$. Incident FUV fluxes can range from $G_0 \lesssim 1$ for clouds illuminated by the local ISRF to $G_0 \gtrsim 10^6$ for PDRs located close to O stars.

1.3 Penetration of far-ultraviolet radiation

As the name suggests, photon-dominated regions derive their structure primarily from the penetration of FUV photons into their interiors. Dust grains provide the major source of continuum opacity in interstellar clouds and attenuate the incident radiation field by selectively absorbing and

scattering light at visible and ultraviolet wavelengths. The radiative transfer of FUV radiation in a dusty medium has been studied in detail for many scenarios, but for the most part, the assumption of homogeneity and a simplified geometry are sufficient for the modelling of PDRs. The importance of the cloud geometry will be discussed in Section 2.2.2, but for now we will restrict our attention to the penetration of FUV radiation into a one-dimensional plane-parallel slab, which will hopefully allow a clearer understanding of the processes taking place within the PDR, and in any case is the common assumption made by the majority of PDR models. The "surface" of the PDR is then the point at which the FUV radiation first comes into contact with the neutral gas and is perpendicular to the path the light will take as it permeates the cloud. Flannery et al. (1980) solved the radiative transfer equation for plane-parallel slabs of various thicknesses and showed that the mean intensity is given by

$$G_0(A_V, \lambda) = G_0(0) \exp(-k\xi_\lambda A_V)\,, \tag{1.1}$$

where $G_0(0)$ is the intensity of the unattenuated radiation field at the PDR surface, k depends on the scattering properties of the dust grains (see below), ξ_λ is the ratio of the extinction at wavelength λ to that in the visual ($\lambda_V \sim 5550$ Å), and A_V is the visual extinction measured from the surface of the slab. To first order, k is given by the diffusion approximation (Flannery et al. 1980),

$$k = \sqrt{3(1-\omega)(1-\omega g)}\,, \tag{1.2}$$

in which ω is the albedo of the dust grains and g is the scattering phase function (i.e., the mean cosine of the scattering angle, $\langle \cos\theta \rangle$). The visual extinction is related to the dust properties by

$$A_V = 1.086\,\tau_V = 1.086 \int_0^z n_{\rm gr} Q_{\rm ext} \langle \sigma_{\rm gr} \rangle \, {\rm d}z'\,, \tag{1.3}$$

where τ_V is the optical depth in the visual, $n_{\rm gr}$ is the number density of dust grains (in cm^{-3}), $Q_{\rm ext}$ is the ratio of the grain visual extinction cross section to its geometric cross section, $\langle \sigma_{\rm gr} \rangle$ is the average grain geometric cross section (in cm^2) and z is the distance into the slab (in cm), measured from, and perpendicular to, the surface. For thin clouds, a correction factor has to be included in equation (1.1) to allow for photons penetrating from the far side of the cloud.

The intensity of the radiation field inside an interstellar cloud is therefore largely determined by the absorption and scattering properties adopted for the dust grains and, unfortunately, these are by no means certain. Their values are based either upon "average" properties measured directly for a limited number of lines of sight through diffuse interstellar clouds (Savage & Mathis 1979; Mathis 1990), or upon models that fit these "average" properties (e.g. Draine & Lee 1984). Even within

this limited sample, there is evidence for variation between clouds (Cardelli et al. 1989). The ratio of total to selective extinction,

$$R_V = \frac{A_V}{E(B-V)}, \tag{1.4}$$

is a common measure of the slope of the wavelength-dependent extinction curve in the optical and can be used to determine an approximate extinction law (Cardelli et al. 1989). Observed values of R_V are known to vary quite significantly from one sightline to another (Welty & Fowler 1992; Fitzpatrick 1999), with typical values of $R_V \approx 3.1$ observed for diffuse clouds and larger values of $\approx$ 5–6 for dense molecular clouds. Using H Lyman-α emission and UV absorption lines of H_2 to determine the column densities of atomic and molecular hydrogen, and thus the total column density of hydrogen nuclei, $N_{\rm H} = N({\rm H}) + 2N({\rm H_2})$, along lines of sight through diffuse clouds, Bohlin et al. (1978) found

$$N_{\rm H}/E(B-V) = 5.8 \times 10^{21}\ {\rm cm^{-2}\,mag^{-1}}, \tag{1.5}$$

$$N_{\rm H}/A_V \approx 1.9 \times 10^{21}\ {\rm cm^{-2}\,mag^{-1}} \quad \text{for} \quad R_V = 3.1\,. \tag{1.6}$$

These values are still widely used today to calculate the A_V–depth relation (since $N_{\rm H} = \int n\,{\rm d}z = nz$ for a slab of constant density), but one must bear in mind that the observations were necessarily limited to diffuse cloud lines of sight and may not apply to dense molecular clouds. The FUV radiation is also subject to attenuation by H_2 and CO line absorption, which are discussed in Sections 1.4.2 and 1.4.3.

1.4 PDR chemistry

The attenuation of the FUV flux with distance into the PDR gives rise to a characteristic depth-dependent chemical structure, separated into distinct zones within which the chemistry is controlled by specific sets of gas-phase reactions involving key atomic species whose ionization potentials lie below the Lyman limit, causing them to be photoionized by the incident radiation. As the intensity of destructive photons diminishes, these atoms are able to make the transition from ionic to neutral form, before becoming bound into molecules at greater depths. The sizes and locations of the (partially overlapping) chemical zones depend on the key PDR parameters, n and G_0, on the gas-phase elemental abundances and on the cosmic-ray particle flux.

Molecular hydrogen plays a crucial role in PDR chemistry, and in astrochemistry as a whole, initiating many of the key reaction sequences and controlling the transition from predominantly

atomic to predominantly molecular gas. We will therefore consider the formation and photodissociation of H_2 in detail in the next two sections. Carbon monoxide (CO) is also important in PDR chemistry and its photodissociation requires careful consideration as well, as is discussed in Section 1.4.3.

1.4.1 H_2 formation

One might naïvely suppose that molecular hydrogen is most often produced by the direct radiative association of hydrogen atoms,

$$\mathrm{H} + \mathrm{H} \rightarrow \mathrm{H}_2 + h\nu, \tag{1.7}$$

however, this reaction is extremely slow under typical interstellar conditions (Gould & Salpeter 1963), the reason being that the emitted photon, required to stabilise the association of the two ground state atoms, results from a transition that is strongly forbidden (from the repulsive triplet state to the ground electronic state of the H_2 molecule, $b\,^3\Sigma_u^+ \rightarrow X\,^1\Sigma_g^+$). The radiative recombination of an H atom in the ground state with an H atom in an excited state can proceed via allowed transitions, but the fraction of atoms in excited states is small and this process can also generally be neglected. The three-body reaction, $3\mathrm{H} \rightarrow \mathrm{H}_2 + \mathrm{H}$, is inefficient at number densities $n < 10^{10}$ cm^{-3} and can be disregarded in the interstellar medium.

Molecular hydrogen may be formed in the gas phase by radiative association followed by associative detachment (McDowell 1961; de Jong 1972),

$$\begin{aligned} \mathrm{H} + e^- &\rightarrow \mathrm{H}^- + h\nu \\ \mathrm{H}^- + \mathrm{H} &\rightarrow \mathrm{H}_2 + e^- \end{aligned} \tag{1.8}$$

in which the electron acts as a catalyst. However, this process is only efficient when the electron density is high and the radiation field which dissociates H^- is weak (Dalgarno & McCray 1973). Since the H^- radical can be destroyed by near-IR light, which suffers less attenuation by dust grains than visible light, this process only becomes important deep within clouds ($A_V \gg 5$ mag).

Gould & Salpeter (1963) were the first to model the formation of molecular hydrogen by recombination of H atoms on the surface of interstellar dust grains, a mechanism first suggested by van de Hulst in 1948. In this process, the dust grain acts as the stabilising "third body" that carries away some of the 4.5 eV of excess energy from the formation of the molecule. Briefly stated, the mechanism is as follows. Hydrogen atoms striking a grain become trapped on the surface with a certain probability, either due to van der Waals forces (physical adsorption, or physisorption), or by

the formation of chemical bonds (chemisorption). Once on the grain, adsorbed H atoms (adatoms) are able to move across the surface with some degree of mobility, which is dependent on the strength of their bond to the surface, and will spend some average time $t_{\rm H}$ on the surface (residence time) before returning to the gas phase. If, during that time, two H adatoms meet, either by both "hopping" to the same adsorption site (the so-called Langmuir-Hinshelwood mechanism), or by a passing H atom in the gas becoming trapped in the adsorption site of a pre-existing adatom (the Eley-Rideal mechanism), they will interact and form a hydrogen molecule. The newly created molecule is less strongly bound to the grain surface and quickly desorbs. The excess energy resulting from the formation process is shared between the molecule, which is injected into the gas in an excited state with some amount of kinetic energy, and the grain, which carries the energy away through lattice vibrations.

Initially, Gould & Salpeter (1963) considered recombination of physisorbed H atoms on featureless "dirty" ice surfaces and found it to be efficient for grain temperatures below 10–20 K. Knaap et al. (1966) repeated the calculation including the zero-point energy of the absorbed atoms and concluded that grain temperatures below 5–8 K are required for the process to be effective. Hollenbach & Salpeter (1970, 1971), recognising that such a small temperature range would severely limit the importance of grain catalysed H_2 formation, extended the treatment to irregular surfaces with H atoms bound to lattice-defect sites or impurities having adsorption energies exceeding that of normal physisorption. They obtained recombination efficiencies of $\simeq 1$ for grain temperatures below a critical value of 40–50 K.

The H_2 formation rate per unit volume, averaged over the grain size distribution, that was originally derived by Hollenbach & Salpeter (1970, 1971) can be written

$$R_{\rm f} = \frac{1}{2} S(T, T_{\rm d}) \eta(T_{\rm d}) n_{\rm gr} n({\rm H}) \langle \sigma_{\rm gr} \rangle \langle v_{\rm H} \rangle \qquad [{\rm cm^{-3}\,s^{-1}}], \tag{1.9}$$

where $S(T, T_{\rm d})$ is the probability that a hydrogen atom with temperature T, colliding with a dust grain of temperature $T_{\rm d}$, will stick to the surface (generally called the sticking coefficient); $\eta(T_{\rm d})$ is the probability that a trapped grain will traverse the grain surface, find another H adatom and recombine, the H_2 molecule subsequently evaporating from the grain surface; $n_{\rm gr}$ is the number density of dust grains (in ${\rm cm^{-3}}$); $n({\rm H})$ is the number density of H atoms (in ${\rm cm^{-3}}$); $\langle \sigma_{\rm gr} \rangle$ is the average grain geometric cross section (in ${\rm cm^2}$); and $\langle v_{\rm H} \rangle$ is the mean thermal speed of H atoms in the gas (in ${\rm cm\,s^{-1}}$). Typically, $n_{\rm gr} \langle \sigma_{\rm gr} \rangle \sim (10^{-21}\,{\rm cm^2}) n$ (recall that n is the number density of hydrogen nuclei) and $\langle v_{\rm H} \rangle \sim 10^4 \sqrt{T}\,{\rm cm\,s^{-1}}$. Equation (1.9) then becomes

$$R_{\rm f} \sim 3 \times 10^{-18} S(T, T_{\rm d}) \eta(T_{\rm d}) \sqrt{T} n\, n({\rm H}) \qquad [{\rm cm^{-3}\,s^{-1}}]. \tag{1.10}$$

Observational support for the validity of this rate was provided by Jura (1974), who compared observed abundances of H and H_2 to derive empirical formation and destruction rates for H_2, giving a formation rate of $R_f \sim 10^{-17}$ cm^{-3} s^{-1} at a temperature of 100 K.

At sufficiently low temperatures, S and $\eta \sim 1$, but both tend to decrease with rising temperature; the H atoms move at greater speed and are more likely to bounce off the surface than stick, the adatoms have a shorter residence time and may evaporate before they can recombine. Estimating the temperature-dependence of S and η is therefore crucial in order to derive reliable formation rates under varying conditions.

Recent emphasis has been on laboratory work, which in general supports the viability of the H_2 formation mechanism, though there is still some debate about the temperatures for which it is efficient. Overall, whilst the mechanisms governing H_2 formation on dust grains are now fairly well understood at the low temperatures typical of dark clouds, the formation rate at the higher grain temperatures found in PDRs is rather uncertain. Given this uncertainty, a simple approximation for the rate is often assumed.

1.4.2 H_2 photodissociation

Spitzer (1948) first pointed out that molecular hydrogen is effectively shielded from direct photodissociation in neutral regions, since the photodissociation continuum (14.7 eV) and photoionization continuum (15.4 eV) of H_2 lie above the Lyman limit (13.6 eV). Therefore, whilst H_2 is rapidly destroyed in H II regions, another means of photodestruction is required in PDRs. It was Solomon (1965, cited in Field et al. 1966) who suggested an efficient alternative route for the photodissociation of H_2; a two-step process of absorption via electronic transitions from the ground state ($X\,^1\Sigma_g^+$) to the Lyman ($B\,^1\Sigma_u^+$; 11.2 eV) or Werner ($C\,^1\Pi_u$; 12.3 eV) bands, followed by radiative decay to the vibrational continuum of the ground electronic state and dissociation of the molecule. Stecher & Williams (1967) later introduced a formal description of this mechanism and calculated its rate. The process is shown schematically in Figure 1.2 and may be summarized by the equation

$$H_2(X\,^1\Sigma_g^+, v = 0) \xrightarrow{h\nu} H_2(B\,^1\Sigma_u^+, v = v') \xrightarrow{h\nu'} H_2(X\,^1\Sigma_g^+, v = v'') \qquad (1.11)$$

for the case of Lyman band absorption, where v is the vibrational level of the molecule. This process leads to dissociation if $v'' > 14$ (the vibrational continuum). If instead radiative decay leaves the molecule in a vibrationally excited, but bound, level of the ground electronic state ($2 \leq v'' \leq 14$), subsequent absorption of another FUV photon can lead to direct photoionization or

photodissociation,

$$H_2(X\,^1\Sigma_g^+, v = v'' \leq 14) \xrightarrow{h\nu} \begin{cases} H_2^+ + e^- \\ H + H \end{cases} \tag{1.12}$$

The spontaneous radiative dissociation mechanism shown in equation (1.11) is now understood to dominate the photodestruction of H_2 in neutral interstellar clouds. For the standard Draine ISRF, the total unattenuated photodissociation rate of molecular hydrogen, summed over all relevant absorption lines, is $\sim 5 \times 10^{-11}$ s^{-1}. Absorption in the Lyman band dominates, with transitions in the Werner band generally contributing little to the photodissociation rate.

Because this mechanism is initiated by line rather than continuous absorption, increasing optical depth in the H_2 lines results in a decreasing rate of dissociation, so that hydrogen molecules in the outer part of the cloud shield the hydrogen molecules at greater depths from the dissociating radiation. This "self-shielding" can, under certain conditions, exceed the attenuation due to scattering and absorption of photons by dust grains. Hollenbach et al. (1971) showed that H_2 photodissociation is controlled by the self-shielding function,

$$\theta_i = \frac{\int_{-\infty}^{\infty} \sigma_i(\nu) \exp[-N_i \sigma_i(\nu)] d\nu}{\int_{-\infty}^{\infty} \sigma_i(\nu) d\nu}, \tag{1.13}$$

where the subscript i refers to a particular transition in the Lyman or Werner systems; $\sigma_i(\nu)$ is the cross section for excitation (in cm^2) and N_i is the column density of molecular hydrogen in the lower state of the transition (in cm^{-2}) along the line of sight to the surface. At the surface of the cloud $\theta_i = 1$ and H_2 is photodissociated by the unattenuated FUV radiation. As the column density of absorbing molecules increases, the radiation field is attenuated in the line and $\theta_i \rightarrow 0$ as $N_i \rightarrow \infty$, reducing the photodissociation rate accordingly. The self-shielding function may alternatively be expressed as (Federman et al. 1979)

$$\theta_i = \frac{dW_i}{d(N_i \sigma_i)}, \tag{1.14}$$

where W_i is the equivalent width for the ith transition,

$$W_i(N_i) = \int \{1 - \exp[-N_i \sigma_i(\nu)]\} d\nu. \tag{1.15}$$

These expressions have been evaluated numerically for the total self-shielding summed over all transitions by a number of groups (e.g. Federman et al. 1979; van Dishoeck & Black 1986; Draine & Bertoldi 1996) and analytic approximations have been derived to fit the results. Such analytic formulae have been shown to be reliable in most situations and are used extensively in PDR models.

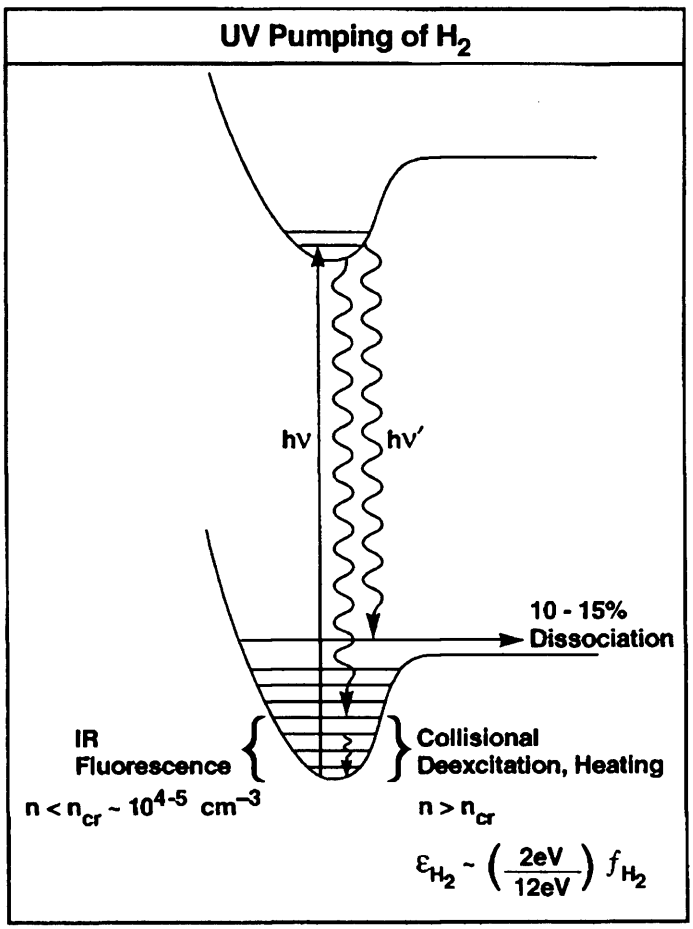

Figure 1.2: The two-step photodissociation of H_2: absorption of FUV photons ($912 \leq \lambda \leq 1108$ Å) in the Lyman and Werner bands, followed by radiative decay to the vibrational continuum ($v'' > 14$) of the ground electronic state. This occurs in 10–15% of the cases, the majority of decays leading to a vibrationally excited molecule in the ground electronic state. *Source: Hollenbach & Tielens (1999)*

In addition to self-shielding, overlap of atomic hydrogen lines with the Lyman and Werner bands of H_2 also contributes to the attenuation of the photodissociation rate, although this is only significant in the line wings, becoming important at greater cloud depths. The wavelength range 912 Å $\leq \lambda \leq$ 1110 Å contains the Lyman-β, γ, δ, ... lines of atomic hydrogen, at 1025.72 Å, 972.54 Å, 949.75 Å, ... Since PDRs can possess large column densities of atomic hydrogen, these lines may suppress absorption in some of the H_2 transitions. The calculation of line overlap effects requires that the wavelength-dependent penetration of the radiation field be treated explicitly, through the detailed computation of radiative transfer within the cloud, and this has been examined in detail by a number of authors (van Dishoeck & Black 1986; Abgrall et al. 1992; Le Bourlot et al. 1993a; Draine & Bertoldi 1996; Lee et al. 1996). Lee et al. (1996) have produced tables of shielding coefficients that can be used to obtain reliable estimates of the H_2 photodissociation rate without the need for computationally expensive radiative transfer calculations.

1.4.3 Carbon photoreactions

In a manner similar to that of molecular hydrogen, the photodissociation of CO proceeds indirectly by absorption in predissociating lines to an excited electronic state, followed by transition to a repulsive electronic state and dissociation. Since this process is again initiated by line absorption, self-shielding is important, but unlike H_2 photodissociation, overlap with atomic hydrogen and H_2 lines plays a significant role, due to the large optical depths in the H_2 lines. The photodissociation rate of CO rapidly declines once molecular hydrogen is abundant and the depth of the C II/C/CO transition layer is therefore linked to that of the H/H_2 transition layer when H_2 self-shielding is more important than attenuation by dust. Again, detailed radiative transfer in the CO absorption lines is required to calculate the full effects of self-shielding and line overlap. van Dishoeck & Black (1988); Lee et al. (1996) have carried out such calculations and present tables of shielding coefficients that may be used to calculate the photodissociation rate with reasonable accuracy and significantly less computational demand.

Carbon has an ionization potential of 11.26 eV and so is photoionized by the FUV radiation. Since the photoionization of carbon proceeds via line absorption, it is subject to self-shielding effects in much the same way as molecular hydrogen. However, its low abundance means that the lines do not become optically thick, and the contribution of self-shielding to the total shielding is generally small. Carbon absorption lines also overlap with those of molecular hydrogen. H_2 therefore provides effective shielding, since its lines become optically thick. Shielding due to absorption in the Lyman lines of atomic hydrogen is negligible. Kamp & Bertoldi (2000) derived

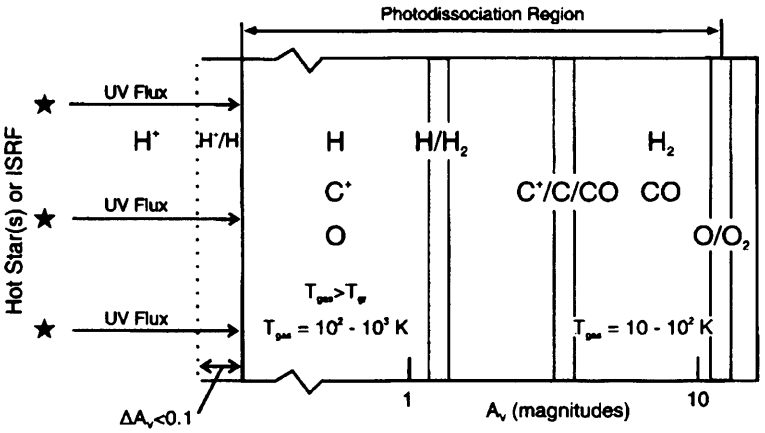

Figure 1.3: A schematic diagram of a photon-dominated region. The PDR is illuminated from the left and extends from the predominantly atomic surface region to the point where O_2 is no longer appreciably photodissociated ($A_V \approx 10$ mag). *Source: Hollenbach & Tielens (1999).*

the total shielding of the FUV radiation appropriate for the photoionization of carbon, including contributions from dust extinction, neutral carbon absorption and overlapping H_2 lines,

$$\tau = \tau_{\rm uv} + a_{\rm C} N({\rm C}) + 0.9\, T^{0.27} \left[N({\rm H_2}) / 10^{22}\ {\rm cm}^{-2} \right]^{0.45}, \tag{1.16}$$

where $\tau_{\rm uv}$ is the dust optical depth in the FUV, $a_{\rm C} \approx 1.1 \times 10^{-17}$ cm^2 is the FUV-averaged carbon ionization cross section (from Osterbrock 1989), T is the gas temperature, and $N({\rm C})$ and $N({\rm H_2})$ are the column densities (in cm^{-2}) of neutral carbon atoms and hydrogen molecules, respectively, as measured from the surface of the PDR.

Despite this shielding, photoionization maintains high abundances of singly ionized carbon to considerable depths within the PDR. The C^+/C balance is dominated by photoionization and radiative recombination, with the scales shifting in favour of recombination as the FUV radiation diminishes. This is the location of the C II/C/CO transition layer, in which the neutral carbon abundance peaks, before dropping off at greater depths as carbon becomes locked into the stable CO molecule, through the "burning" of CH and CH_2 radicals by atomic oxygen.

1.4.4 PDR chemical zones

The various chemically-distinct zones that arise in dense PDRs are now discussed, in order of increasing depth from the surface of the PDR. The spatial structure of these zones is depicted in Figure 1.3.

H I zone

At the surface of the PDR, ionized hydrogen swiftly recombines once all photons above the Lyman limit are absorbed, whilst molecular hydrogen is rapidly photodissociated in the harsh FUV radiation. The surface layer therefore consists mainly of atomic hydrogen, with all carbon, sulphur and silicon in singly ionized form (because their ionization potentials are below the Lyman limit) and all oxygen and nitrogen in atomic form.

H/H_2 transition layer

Further into the cloud, the FUV flux begins to drops off and the formation of H_2 starts to win the battle against photodissociation. An H/H_2 transition layer appears beyond the H I zone as the dominant form of hydrogen shifts from atomic to molecular with increasing depth. Photodissociation and photoionization still maintain large abundances of O, N, C^+, S^+ and Si^+. The H/H_2 transition layer plays an important role in the PDR chemistry since further reaction networks are initiated once molecular hydrogen becomes abundant. In dense PDRs the gas in the outer regions can become hot and the combination of high gas temperatures and rising H_2 density initiates a set of endothermic reactions,

$$\begin{aligned} O + H_2 &\rightarrow OH + H \\ C^+ + H_2 &\rightarrow CH^+ + H \\ N + H_2 &\rightarrow NH + H \\ S^+ + H_2 &\rightarrow SH^+ + H, \end{aligned}$$

whose products may subsequently be photodissociated or undergo the reverse reactions or, in the case of CH^+ and SH^+, suffer dissociative recombination. When the H_2 density becomes large, these reactions can produce high abundances of OH and CH^+ in the H/H_2 transition layer, where the high temperatures necessary for the endothermic reactions to proceed efficiently can be maintained. Hydrogen molecules left in vibrationally excited states following FUV absorption (denoted by H_2^*) may also be sufficiently energetic to overcome the endothermicities of these reactions, becoming important in low density PDRs where the temperature is lower.

The high abundance of the OH radical then gives rise to a series of fast ion-molecule reactions

that produce the molecular ions SO^+, CO^+, HCO^+ and HOC^+,

$$S^+ + OH \rightarrow SO^+ + H$$
$$C^+ + OH \rightarrow CO^+ + H$$
$$CO^+ + H_2 \rightarrow HCO^+ + H$$
$$CO^+ + H_2 \rightarrow HOC^+ + H$$

and a series of slower neutral-neutral reactions that produce the molecules NO, O_2 and H_2O,

$$N + OH \rightarrow NO + H$$
$$O + OH \rightarrow O_2 + H$$
$$H_2 + OH \rightarrow H_2O + H$$

all of which can be subsequently destroyed by photodissociation. The molecular ions can also be destroyed by dissociative recombination or reactions with H_2, and water can be destroyed by reacting with H to produce H_2 and OH again. The dissociative recombination of HCO^+ and charge transfer between CO^+ and H are important formation routes for CO, which can be formed efficiently in the outer cloud layers, where the electron density is high due to photoionization of carbon and sulphur, and hydrogen is still mainly atomic,

$$HCO^+ + e \rightarrow CO + H$$
$$CO^+ + H \rightarrow CO + H^+$$

C II zone

The photoionization of atomic carbon by FUV photons,

$$C + h\nu \rightarrow C^+ + e,$$

produces a cloud layer of singly ionized carbon. This layer generally extends to a greater depth than the H I zone, since the self-shielding of H_2 allows it to survive nearer the cloud surface, resulting in a C II zone beyond the H I zone within which carbon is ionized but hydrogen is fully molecular. The C II zone is cooler than the H/H_2 transition layer and the endothermic reactions that produce abundant OH, CH^+ and NH near the surface are much less efficient here. Typically, the C II zone lies between visual extinctions $1 \lesssim A_V \lesssim 2$ mag.

As you might expect, the chemistry within the C II zone is generally initiated by reactions

involving C^+. In particular, carbon-bearing radicals are produced by the sequence

$$C^+ + H_2^* \rightarrow CH^+ + H$$
$$C^+ + H_2 \rightarrow CH_2^+ + h\nu$$
$$CH^+ + H_2 \rightarrow CH_2^+ + H$$
$$CH_2^+ + H_2 \rightarrow CH_3^+ + H$$
$$CH_3^+ + e \rightarrow CH_2 + H$$
$$CH_3^+ + e \rightarrow CH + H_2$$
$$CH_2^+ + e \rightarrow CH + H$$

CH and CH_2 are destroyed by photodissociation and so reach their peak abundances at the inner (i.e. deeper) edge of the C II zone, where the FUV flux is reduced and the C^+ density is still large. As we head deeper into the cloud, the C^+ density declines and so too do the abundances of the carbon radicals. They are also lost through insertion reactions that lead to the formation of complex hydrocarbons (by complex, we mean up to several carbon atoms in size, e.g. C_2H),

$$CH_n + C^+ \rightarrow C_2H_{n-1}^+ + H$$

The hydrocarbons that are produced are susceptible to photodissociation and so their abundances also peak at the inner edge of the C II zone.

Continuing inwards, the FUV radiation is further diminished and the C^+ undergoes radiative recombination and charge transfer with atomic sulphur,

$$C^+ + S \rightarrow C + S^+$$

causing the density of neutral atomic carbon to become significant beyond the inner edge of the C II zone.

C II/C/CO transition layer

The UV radiation has now become severely attenuated at these depths and carbon makes the transition from a singly ionized state to being locked in the stable molecule CO. Between these two states, the carbon is in neutral atomic form and can attain high abundances in the transition layer beyond the C II zone. Photodissociation of CH also contributes to the neutral carbon abundance, which is itself then driven into stable CO molecules via neutral-neutral reactions at depths beyond the C II zone,

$$CH + O \rightarrow CO + H$$
$$CH_2 + O \rightarrow CO + H_2$$

At greater depths, carbon is predominantly in CO and the atomic carbon abundance drops rapidly.

S II zone

Photoionization of atomic sulphur by FUV photons,

$$S + h\nu \rightarrow S^+ + e,$$

maintains a layer of singly ionized sulphur that is directly analogous to that of carbon. However, sulphur has a lower ionization potential than carbon (10.4 eV, rather than 11.3 ev) and is less abundant (by over an order of magnitude), so remains in S^+ to a greater depth than the C II zone. An S II zone therefore exists beyond the C II zone, in which sulphur is singly ionized but carbon is neutral (and hydrogen is fully molecular). Charge transfer between C^+ and S also contributes to the extended layer of ionized sulphur and high densities of neutral carbon can be maintained across the transition from C II to S II zone. For dense PDRs, the S II zone usually lies between $2 \lesssim A_V \lesssim 4$ mag.

Beyond the S II zone the sulphur is in neutral form, maintained by photodestruction of sulphur bearing molecules, radiative recombination of S^+ and charge transfer with silicon. At these depths, the FUV radiation is severely attenuated and the electron density becomes small. PDR chemistry now gives way to the well-established ion-molecule chemistry of dark clouds (Prasad & Huntress 1980; Herbst & Leung 1989), with cosmic-ray ionization driving most reaction sequences. However, oxygen remains in atomic form deep into the cloud and reactions with molecular ions become competitive. At large depths ($A_V \gtrsim 8$ mag), all but a small fraction of hydrogen is in H_2, carbon is mostly locked in the stable CO molecule, SO and SO_2 become the dominant forms of sulphur and oxygen forms O_2 via reactions with OH.

1.5 Heating and cooling mechanisms

1.5.1 Photoelectric heating

Direct coupling of non-ionizing photons to a predominantly neutral gas is generally inefficient due to the low opacity of the gas. Absorption by interstellar dust grains therefore plays an important role in transferring energy from the starlight to the gas. The mechanism by which this energy transfer takes place is the photoelectric ejection of electrons from dust grains and PAHs, which subsequently transfer their kinetic energy to the gas, providing an important heating source. FUV photons absorbed by a dust grain produce mobile electrons that can diffuse through the grain, reach the surface and, if sufficiently energetic, overcome the work function W of the grain and any Coulomb potential ϕ_c caused by a positive grain charge, to be ejected into the gas with excess

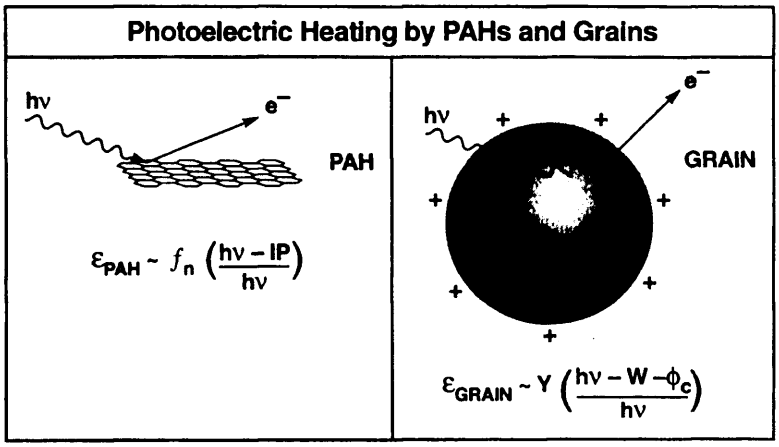

Figure 1.4: The photoelectric heating mechanism: FUV photons are absorbed by interstellar grains and PAHs and energetic electrons are ejected into the gas with excess kinetic energy. *Source: Hollenbach & Tielens (1999).*

kinetic energy. This kinetic energy will then be converted to thermal energy of the gas via inelastic collisions.

The efficiency ϵ of the photoelectric effect on a grain, or the fraction of energy imparted to grains by absorption of FUV photons that contributes to the gas heating, is the product of the photoelectric yield Y (the probability that an electron will be ejected following the absorption of a photon) and the fraction of photon energy carried away as kinetic energy by the electron,

$$\epsilon \sim Y \left(\frac{h\nu - W - \phi_c}{h\nu} \right). \tag{1.17}$$

Bakes & Tielens (1994) modelled in detail the photoelectric heating of interstellar gas by PAHs and very small grains (VSGs), in addition to larger grains. They considered a size distribution of graphitic grains extending down into the molecular domain and evaluated the net heating rate, taking into account grain charging, multiple ionization stages of the grains and recombination of electrons with grains. They found that heating was dominated by PAHs and small grains and derived a simple analytical expression for the photoelectric heating efficiency that is dependent only on G_0, T and n_e. It should be noted, however, that the photoelectric yield Y and efficiency ϵ of the photoelectric effect still remain somewhat uncertain parameters.

1.5.2 H_2 FUV pumping

Molecular hydrogen is subject to electronic excitation through line absorption of FUV photons in the Lyman and Werner bands, as described in Section 1.4.2. This FUV "pumping" is followed

by spontaneous UV fluorescence to the ground electronic state, with 10–15% of molecules left in the vibrational continuum and dissociating, and 85–90% of molecules left in a vibrationally excited bound state. These excited hydrogen molecules (H_2^*) typically possess $E_{\rm vib} \sim 2$ eV of internal vibrational energy and cascade to the ground vibrational state by emission of IR photons when the gas is at sufficiently low density. This leads to the characteristic far-red and near-IR rovibrational spectrum observed towards many diffuse clouds. However, at higher densities, it is collisional de-excitation, rather than radiative decay, that returns the excited molecules to a thermalised rovibrational state. This process heats the gas (see Figure 1.2) and provides an efficient coupling to the FUV photons when H_2 self-shielding outweighs dust extinction, as is the case for $G_0/n \lesssim 0.04$ cm^3 (Draine & Bertoldi 1996).

The critical density at which collisional de-excitation becomes important is dictated by the rate of collisions with atomic hydrogen, the main collision partner for H_2, and is typically $n_{\rm cr} \sim 10^4$–10^5 cm^{-3}, depending on the gas temperature (Martin & Mandy 1995; Martin et al. 1996). Above the critical density, vibrationally excited molecules lose their internal energy through collisions, the H atoms carry away that energy and transfer it to the thermal energy of the gas. This heating mechanism is most efficient in the atomic H I zone nearest the surface, where the FUV pumping rate is highest and H_2 molecules undergo frequent collisional de-excitation with the abundant H atoms.

1.5.3 H_2 photodissociation

The 10–15% of hydrogen molecules that are dissociated following FUV pumping typically release 0.4 eV of internal energy per molecule and the heating rate due to this process is dictated by the rate of FUV pumping. Given that newly formed H_2 also imparts some of its formation energy to the gas, the rapid cycle of formation and photodestruction near the surface of the PDR can prove to be an effective heating mechanism when the FUV flux is high, maintaining high gas temperatures.

1.5.4 Carbon photoionization

Photoionization of neutral carbon atoms releases, on average, 1 eV per ionization and the heating rate associated with this process is simply proportional to the photoionization rate for neutral carbon (see Section 1.4.3). Its contribution to the overall heating rate is generally small and drops off rapidly at the C II/C I/CO transition layer.

1.5.5 Other heating mechanisms

Additional heating of the gas can result from collisions with warmer grains, cosmic-ray ionization and excitation, the decay of turbulence within the cloud and pumping of neutral oxygen to excited states by absorption of FIR emission from warm dust. However, the contribution to the total heating rate from these processes is generally small, only becoming important at large depths ($A_V \gtrsim 6$ mag; Tielens & Hollenbach 1985a).

Overall, photoelectric heating due to small grains and PAHs and collisional de-excitation of FUV pumped H_2 couple the gas heating to the incident FUV flux and dominate the heating in the outer region of the cloud. High densities lead to effective heating by FUV pumping nearest the surface, whilst photoelectric heating generally peaks slightly deeper into the cloud, since the high electron density at the cloud surface reduces the efficiency with which photoelectrons are ejected.

1.5.6 Cooling

The gas in PDRs cools by radiating away its thermal energy, primarily at far-infrared (FIR; 10 μm $< \lambda <$ 200 μm) and submillimetre (submm; 200 μm $< \lambda <$ 3 mm) wavelengths. Cooling is generally via the FIR fine structure lines, [C II] 158 μm, [O I] 63 μm and 146 μm, [C I] 609 μm and 370 μm, and [Si II] 35 μm, near-infrared H_2 rovibrational lines and molecular rotational lines, primarily of CO, but also of OH and H_2O. High densities and high G_0 can lead to gas temperatures at the PDR surface in excess of 5000 K. At these temperatures, significant cooling can occur in the [Fe II] 1.26 μm and 1.64 μm, [O I] 6300 Å, [S II] 6730 Å, and Lyman-α lines (Burton et al. 1990). At high densities, collisions between the hot gas and cooler dust grains may prove to be efficient at cooling the gas, whilst the impact on the dust temperature is negligible (Burke & Hollenbach 1983). The dust istelf cools efficiently through continuum emission in the FIR.

1.6 Diagnostic properties of PDR emission lines

Table 1.1 lists the most important cooling transitions arising in PDRs, their wavelengths, upper energy levels $E_{\rm upper}$ and critical densities[3] $n_{\rm cr}$. Spanning far-infrared, submillimetre and millimetre wavelengths, these lines can be used to derive the physical conditions in PDRs. In this section, the main diagnostic properties of these transitions are discussed.

[3]The critical density for a transition is the density at which collisional de-excitation balances spontaneous radiative de-excitation (Osterbrock 1974).

Table 1.1: Transition properties of the main PDR emission lines.

Species	Transition	Wavelength (μm)	$E_{\rm upper}/k$ (K)	Critical Density $n_{\rm cr}$ (cm^{-3})
[C II]	$^2P_{3/2} \rightarrow {}^2P_{1/2}$	157.74	92	3×10^3 [H]
[O I]	$^3P_1 \rightarrow {}^3P_2$	63.18	228	5×10^5 [H]
[O I]	$^3P_0 \rightarrow {}^3P_1$	145.52	326	1×10^5 [H]
[C I]	$^3P_1 \rightarrow {}^3P_0$	609.14	24	5×10^2 [H]
[C I]	$^3P_2 \rightarrow {}^3P_1$	369.87	63	3×10^3 [H]
CO	$J = 1 \rightarrow 0$	2600.78	6	3×10^3 [H_2]
CO	$J = 2 \rightarrow 1$	1300.39	17	1×10^4 [H_2]
CO	$J = 3 \rightarrow 2$	867.00	33	5×10^4 [H_2]
CO	$J = 6 \rightarrow 5$	433.56	116	4×10^5 [H_2]

[C II] 158 μm

The FIR fine structure transition of C^+ at 158 μm is the dominant cooling line in the warm neutral ISM (Dalgarno & McCray 1972). Carbon has a lower ionization potential (11.26 eV) than hydrogen, so is predominantly in the form of C^+ in the surface layers of PDRs, where photoionization of neutral carbon is effective (see Section 1.4). This C^+ zone can often extend to depths of $A_V \leq 4$ mag. The [C II] 158 μm line is reasonably easy to excite, with a transition energy of 92 K, making C^+ an efficient coolant at the typical temperatures ($30 < T < 10^4$ K) found within the warm neutral gas of PDRs. Under these conditions, the 158 μm line is excited by collisions with hydrogen atoms and, to a lesser extent, with hydrogen molecules. As we will see, the [C II] emission can be used in conjunction with the [O I] fine structure lines and the FIR continuum emission to constrain the density n and incident FUV flux G_0 in the neutral gas (e.g. Wolfire et al. 1990; Kaufman et al. 1999). However, [C II] emission occurs in both ionized and neutral gas, and the individual contribution from each component must be determined before the line can be used as a diagnostic of the conditions in the neutral PDR gas.

[O I] 63 & 145 μm

Oxygen has an ionization potential of 13.62 eV, slightly above that of hydrogen. This means that atomic oxygen is found exclusively in neutral regions and first appears just beyond the location of

the H II/H I transition. The incident FUV radiation maintains a significant abundance of atomic oxygen deep into the cloud through photodestruction of CO and O_2. All oxygen not incorporated into CO can remain in atomic form to depths as large as $A_V = 10$ mag under strong FUV fluxes (Sternberg & Dalgarno 1995). O I possesses two fine structure transitions at 63 and 145 μm (see Table 1.1). The 63 μm transition has an excitation energy corresponding to 228 K and a critical density of about 5×10^5 cm^{-3} (at $T \sim 300$ K), so emits primarily in warm and dense gas. After [C II], the [O I] 63 μm transition is the main coolant in PDRs. The 145 μm line has an excitation energy of 326 K, almost 100 K higher than that of the 63 μm line, so the ratio of the two line intensities [O I] 145 μm/[O I] 63 μm is sensitive to the gas temperature for $T \lesssim 300$ K. Since the strength of the FUV radiation field governs the heating of the gas, this line ratio is therefore a diagnostic of the incident FUV flux G_0. Both transitions have similar critical densities, so the line ratio is relatively insensitive to density, although it does show a gradual decrease for $n > 10^5$ cm^{-3} (Kaufman et al. 1999). In many cases, however, the 63 μm line is found to be optically thick in PDRs (e.g. Stacey et al. 1993), whilst the 145 μm line is, by contrast, optically thin under almost all conditions. The [O I] 145 μm/[O I] 63 μm line ratio may therefore be an indicator of optical depth in the 63 μm line.

[O I] and [C II] line ratios

Since the energy required to excite the [O I] 63 μm transition is somewhat higher than for [C II], the line intensity ratio [O I] 63 μm/[C II] 158 μm is expected to increase with gas temperature and hence higher FUV flux G_0. PDR models predict that for $n > 10^3$ cm^{-3} the line ratio increases with both G_0 and n, due to the different critical densities of the two transitions (Wolfire et al. 1990; Kaufman et al. 1999). However, observations of the two fine structure lines in a large sample of galaxies show the ratio to be correlated with the FIR continuum colour, suggesting that the ratio is most sensitive to G_0, since the FIR colour depends on the dust temperature and therefore on G_0 alone. The gas heating efficiency is given by the line-to-continuum intensity ratio ([O I] 63 μm + [C II] 158 μm)/FIR. This is because the two fine structure lines are the principal coolants, whose combined emission strength matches the heating rate of the gas at thermal equilibrium, whilst the FIR continuum intensity results from the absorption and re-emission of the FUV flux by dust grains, thus representing the total energy injected into the PDR by the incident radiation field. The heating is generally dominated by the grain photoelectric effect and since the efficiency of this mechanism is dependent on the ratio G_0/n (Bakes & Tielens 1994), the intensity ratio is also sensitive to G_0/n. The photoelectric heating efficiency falls with increasing G_0/n and the ([O I] 63 μm + [C II]

158 μm)/FIR ratio is observed to follow this trend. For $G_0/n \lesssim 3 \times 10^{-3}$ cm^{-3}, however, this relationship breaks down because [C I] and CO line emission become effective at cooling the gas in the outer regions of the PDR and the [O I]63 μm and [C II] 158 μm lines no longer account for the total cooling.

The various diagnostic line ratios discussed above can be used in combination to constrain the physical properties (i.e. n and G_0) within a region by comparing observed line intensity ratios to PDR model predictions. Such a procedure is carried out in Chapter 4.

CHAPTER 2

DEVELOPING AND BENCHMARKING THE UCL_PDR CODE

This chapter describes the main features of the UCL_PDR code, used throughout this thesis to produce PDR models for the various studies presented. Its involvement in an international PDR benchmarking effort is reviewed. As a result of the benchmarking, the reliability of the UCL_PDR code is confirmed and its suitability for subsequent projects is established.

2.1 Description of the UCL_PDR code

The UCL_PDR code is a time- and depth-dependent PDR model, solving the chemistry, thermal balance and radiative transfer self-consistently within a cloud (these computations are described in detail in Sections 2.1.4, 2.1.5 and 2.1.7). This yields the abundances of each species included in the chemical network and their associated column densities, the emissivities and integrated intensities of the emission lines considered and the gas and dust temperatures, all of which are functions of depth z and time t. The cloud geometry is discussed in Section 2.1.1, but may be summarized as follows; the cloud is treated as a one-dimensional, semi-infinite slab of gas, illuminated by a unidirectional flux of FUV photons incident upon its outer surface. The code loops through all depth-steps for a given time-step before advancing to the next time-step (although the opposite sequence is also possible). An adaptive grid of depth-steps is used in the model, such that the variation in the H_2 self-shielding function (calculated using the approximation of Draine & Bertoldi 1996) is small between depth points ($<10\%$). This ensures that changes in chemical abundances are fully resolved.

At each depth-step, the code calculates the attenuation of the FUV field before beginning an iterative cycle to determine the gas temperature at which the total heating and cooling rates are equal (to within some error tolerance), i.e., the condition of thermal balance is satisfied. For each iteration, the chemistry is first calculated, based on the gas temperature and attenuated FUV flux, after which the heating and cooling rates are computed, together with the radiative transfer in the emission lines, using the revised chemical abundances. The difference between the total heating and cooling rates is then used to derive a new gas temperature and the cycle repeats, beginning again with the calculation of revised chemical abundances. Once the thermal balance criteria have been met, the chemical, physical and emission properties calculated at the appropriate temperature are stored to file and the code advances to the next depth- or time-step. Each of these key computational steps is outlined in Sections 2.1.3–2.1.7 below.

2.1.1 Model geometry

The cloud is modelled assuming one-dimensional plane-parallel geometry and a semi-infinite cloud size, meaning that the cloud is infinitely thick in both the inward direction normal to the cloud surface and the transverse direction along the surface, such that radiation entering or leaving the cloud does so only through the front, envisaged to appear face-on to the observer. The FUV radiation incident upon its surface is unidirectional and strikes the cloud perpendicular to its surface. Distances within the one-dimensional structure are measured along the z-axis, normal to the surface and increasing with depth into the cloud. The various geometries employed by PDR codes are discussed in more detail in Section 2.2.2.

2.1.2 Physical cloud properties

The main free parameters in the UCL_PDR code that describe the physical properties of the model cloud are the number density of hydrogen nuclei, $n = n(\mathrm{H}) + 2n(\mathrm{H_2})$ cm^{-3} (see Section 1.2); the flux of FUV photons incident upon the surface, G_0 times the Habing field or χ times the Draine field (see below); the rate of H_2 ionization by cosmic-rays, ζ (s^{-1}); the metallicity, $Z/Z_\odot$ (see Section 2.1.8); the turbulent Doppler velocity, v_{turb} (km s^{-1}), sometimes designated by δv_{D}; and the gas-phase elemental abundances, relative to total hydrogen nuclei, $X(i) = n(i)/n$, where $n(i)$ is the number density of species i (cm^{-3}). These parameters and typical values appropriate to PDRs are summarized in Table 2.1. The code reads these values from a separate input parameter file upon execution, allowing many different parameter files to be used in succession to construct a grid

Table 2.1: Free parameters describing the physical cloud properties in the UCL_PDR code.

Parameter		Typical Values
Number density of hydrogen nuclei	n	10–10^7 cm^{-3}
Incident FUV flux	G_0 or χ	0.1–10^6 Habing or Draine
Cosmic-ray ionization rate	ζ	1–5 $\times$ 10^{-17} s^{-1}
Metallicity (relative to Solar)	$Z/Z_\odot$	1
Turbulent Doppler velocity	$v_{\rm turb}$	1–3 km s^{-1}

Table 2.2: Gas-phase elemental abundances used in the UCL_PDR code (relative to total hydrogen nuclei).

He	7.5×10^{-2}	C	1.4×10^{-4}	N	6.5×10^{-5}
O	3.2×10^{-4}	Na	8.8×10^{-7}	Mg	5.1×10^{-6}
Si	8.2×10^{-7}	S	1.4×10^{-6}	Cl	1.1×10^{-7}
Ca	5.7×10^{-10}	Fe	3.6×10^{-7}		

of models for parameter space searches (see, e.g., Chapter 5). The standard gas-phase elemental abundances used in the UCL_PDR code are listed in Table 2.2 and are taken from Savage & Sembach (1996), Sofia et al. (1997), Meyer et al. (1998), Snow et al. (2002) and Knauth et al. (2003). These elemental abundances have been used in all models, unless otherwise stated.

One of the main features of the UCL_PDR code is its ability to treat the conditions within the cloud time-dependently. As such, it is capable of handling time-varying physical parameters and can accept input files listing the various free parameters as a function of time. The code is also able to model clouds with arbitrary density profiles, either supplied externally as a function of cloud depth or determined within the code as a function of, e.g., constant pressure. Such versatility makes the code applicable to a wide variety of astrophysical phenomena, one example of which is the application of the UCL_PDR code to modelling an expanding shell of molecular gas surrounding a starburst region in M 82 (discussed in Chapter 6).

2.1.3 FUV radiation and attenuation

The FUV field incident upon the cloud surface is assumed to be the standard interstellar radiation field determined by Habing (1968), multiplied by a free parameter G_0, corresponding to a flux of 1.6×10^3 erg s^{-1} cm^{-2} when $G_0 = 1$. The FUV field may be equivalently expressed in terms of the Draine (1978) ISRF by introducing a scaling factor of 1.7. The FUV flux expressed in this way is then determined by a free parameter $\chi = G_0/1.7$. In the interests of speed, the UCL_PDR code does not explicitly treat the wavelength-dependence of the FUV field, using instead analytical formulae that describe the attenuation of the field through various line and continuum processes, evaluated for the spectral energy distribution of the Habing or Draine field.

The attenuation of FUV radiation inside the cloud is dominated in the continuum by dust grains, which scatter and absorb the light, subsequently re-emitting it at infrared wavelengths (see Section 1.3), whilst absorption in the Lyman and Werner bands of molecular hydrogen dominates the line attenuation of the FUV field, with additional contributions from atomic hydrogen, carbon and CO (see Section 1.4.2 for details). The attenuation by dust is treated in the UCL_PDR code using the formalism of Flannery et al. (1980), as described in Section 1.3, and is governed by the assumed properties of the dust grains. When calculating the attenuation of the FUV field, the distance into the cloud is expressed in terms of the visual extinction A_V ($\lambda_V \sim 5550$ Å) and is related to the cloud depth z through equation (1.3). Given the strength of the unattenuated FUV flux at the cloud surface, $G_0(A_V = 0)$, and the visual extinction at a particular cloud depth, the attenuated flux is calculated in the UCL_PDR code using equation (1.1),

$$G_0(A_V, \lambda) = G_0(A_V = 0) \exp(-k\xi_\lambda A_V),$$

with k and ξ_λ as described in Section 1.3. The UCL_PDR code allows the various dust properties to be specified as free parameters which can vary with cloud depth and time. However, the standard values adopted in the model, and in all the work that follows in this thesis, are listed in Table 2.3 and are assumed to be constant. Assuming a value of $\xi_\lambda = 2.4$ at 1000 Å and calculating k using equation (1.2) and the relevant properties in Table 2.3, the FUV radiation is therefore attenuated by a factor $\exp(-1.38\, A_V)$ at 1000 Å.

The attenuation of the FUV field in the Lyman and Werner bands of H_2 and the predissociating lines of CO are accounted for by the self-shielding functions for the two molecules. H_2 self-shielding is calculated in the UCL_PDR code using the single line approximation of Federman et al. (1979) and CO shielding is determined by performing a spline interpolation across the table of shielding factors presented by van Dishoeck & Black (1988), which include both H_2 shielding and

Table 2.3: Standard dust grain properties adopted in the UCL_PDR code.

Property		Standard Value
Radius	r_g	10^{-5} cm
Mass density	ρ_g	2 g cm^{-3}
Mass	m_g	$\frac{4}{3}\pi r_g^3 \rho_g \approx 8\times10^{-15}$ g
Number density	n_g	$2\times10^{-12}\,Zn$ cm^{-3}
Cross-section	σ_g	$\pi r_g^2 \approx 3\times10^{-10}$ cm^2
Albedo	ω	0.7
Mean scat. angle	g	0.9

CO self-shielding.

2.1.4 Chemistry

A comprehensive chemical network is used in the UCL_PDR code, containing 128 species, including nitrogen and sulphur-bearing molecules, and over 1700 reactions, including ion-molecule, photoionization and photodissociation reactions. Freeze-out of atoms and molecules onto grains and PAH chemistry are neglected. The reaction rates are taken from the UMIST99 database (Le Teuff et al. 2000), with some modifications introduced as part of the benchmarking effort (see Section 2.2). We adopt the grain surface H_2 formation rate of de Jong (1977):

$$R_f = 3 \times 10^{-18}\sqrt{T}\exp(-T/1000) \qquad [\mathrm{cm^3\,s^{-1}}]. \tag{2.1}$$

Self-shielding of H_2 against photodissociation is calculated using the single line approximation of Federman et al. (1979). The shielding factors of van Dishoeck & Black (1988) are adopted for CO. Neutral carbon shielding includes contributions from H_2, CO and C I, using the treatment of Kamp & Bertoldi (2000).

The gas is assumed to be initially in atomic form, with all metals possessing ionization potentials below 13.6 eV in singly ionized form. The chemical abundances are then computed at each depth-step by solving the set of ordinary differential equations describing the formation and destruction of each species in the chemical network for the duration of the current time-step. This is repeated at all time-steps, and the chemistry of the gas evolves accordingly.

2.1.5 Calculation of the thermal balance

The gas temperature is determined at each time- and depth-step using an iterative process to balance the total heating Γ (erg s^{-1} cm^{-3}) and cooling Λ (erg s^{-1} cm^{-3}) rates (discussed in the next two sections). The implicit assumption made in this approach is that the gas is always at thermal equilibrium. A modified version of Ridder's method (using the implementation of Press et al. 1992) is used to find the thermal balance. During the iteration cycle, thermal balance is considered to have been reached if the difference in the total heating and cooling rates is <0.5% or if the change in gas temperature between iterations is <0.1 K. In contrast, the dust temperature is calculated using the analytical expression of Hollenbach et al. (1991) and is a function of the incident FUV flux and the visual extinction at the current depth.

2.1.6 Heating mechanisms

The various heating mechanisms discussed in Section 1.5 are included in the UCL_PDR code using analytical treatments from a variety of sources. The heating rate due to photoejection of electrons from grains and PAHs is taken from Bakes & Tielens (1994), who include a size distribution of particles extending from large grains (~25 μm) to small (~5 Å) PAHs and account for the microphysics of small particles explicitly. A grain size distribution proportional to $a^{-3.5}$ (the so-called MRN distribution; Mathis et al. 1977) is assumed in the heating rate. Heating by collisional de-excitation of FUV-pumped H_2 is approximated using the formula of Hollenbach & McKee (1979) for a single excited pseudovibrational level of H_2^*. Heating due to the photodissociation of H_2 molecules is included using the rate derived by Tielens & Hollenbach (1985a). Cosmic-ray heating and exothermic reactions become significant deeper into the cloud and are also accounted for using the formulae of Tielens & Hollenbach (1985a). Heating due to C I photoionization (Kamp & van Zadelhoff 2001), H_2 formation (Kamp & van Zadelhoff 2001), gas-grain collisions (Burke & Hollenbach 1983) and turbulence (Black 1987) are also included in the calculation of thermal balance in the UCL_PDR code. Together, these processes govern the total heating within the cloud (erg s^{-1} cm^{-3}).

2.1.7 Radiative cooling

As discussed in Section 1.5, the gas in PDRs is mainly cooled through emission from collisionally excited atoms and molecules and by interactions with the cooler dust grains. The UCL_PDR code calculates the emission from the [O I], [C I] and [C II] fine structure lines and CO rotational lines

(up to $J = 11 \rightarrow 10$) at each depth- and time-step using the escape probability formalism of de Jong et al. (1980) to solve the equations of radiative transfer. Non-local thermodynamic equilibrium (non-LTE) level populations are determined by solving the equations of statistical equilibrium using the updated collisional rate coefficients from the recent PDR benchmarking effort for the atomic coolants, O, C and C^+ (see Section 2.2), and the rate coefficients for collisions of CO with H_2, H and He from Flower & Launay (1985), Green & Thaddeus (1976) and Green & Chapman (1978), respectively. The solution of the radiative transfer in the lines produces the emissivity Λ (erg s^{-1} cm^{-3}), intensity I (erg s^{-1} cm^{-2} sr^{-1}) and line opacity tau of each transition considered.

The contribution to the total cooling rate by H_2 emission is calculated using tabulated data from Martin et al. (1996). Lyman-α and O I 6300 Å metastable line emission are also considered (using the treatments of Tielens & Hollenbach 1985a; Sternberg & Dalgarno 1989, respectively). Cooling due to electron recombination onto positively charged grains is treated using the rate derived by Bakes & Tielens (1994).

2.1.8 Treatment of metallicity

The metallicity-dependence appears in several key processes in the UCL_PDR code. Elemental abundances of all metals are assumed to scale linearly with metallicity ($Z/Z_\odot$); the dust-to-gas mass ratio is also assumed to scale linearly with metallicity and takes a standard value of 10^{-2} at Solar metallicity. The formation rate of H_2 on grain surfaces and the grain photoelectric heating rate are assumed to scale linearly with metallicity.

2.1.9 Summary of the UCL_PDR code features

The UCL_PDR code represents a powerful tool for the study of interstellar gas under a wide variety of conditions. Its short computation times and time-dependent capability make it suitable for both parameter space studies and detailed modelling of phenomena that evolve rapidly with time. The code produces a large amount of useful output data, including the abundances and column densities of all the species contained in the chemical network, the line intensities and opacities of the main fine structure and CO rotational transitions and the gas and dust temperatures, all as a function of time and cloud depth. These data can then be compared with observations, in particular, the predicted intensities of the fine structure and CO emission lines, which can be used to infer the most appropriate cloud conditions for the observed region. Such a study is undertaken in Chapter 4.

2.2 Benchmarking the UCL_PDR code

2.2.1 The need for benchmarking

Growing interest in the study of PDRs has seen the development of a number of independent models over the last 30 years, each placing a slightly different emphasis on the treatment of physical and chemical processes within these regions. Whilst all models attempt to reproduce the most important PDR features, computational constraints preclude the detailed treatment of every aspect and some approximations must inevitably be made. The choice of which processes to treat explicitly and which to simplify for computational efficiency is largely motivated by the intended application of the code. Some models attempt to treat the microphysics of as many processes as possible, at the expense of lengthy computation. As we have already seen, PDRs are present in a diverse range of environments and some models are devoted to treating the specific combination of conditions that are characteristic of certain astronomical phenomena. The complexity of these codes and the individual choice of how to implement the various processes naturally results in a certain amount of disagreement between model results, and even characteristic features, such as the location of the H/H_2 transition layer, are found to vary from model to model. In addition, the nature of these processes are themselves sometimes under debate and there is some difference of opinion on the appropriate treatment.

The need for a consensus model and insight into the dependence of results upon the choice of treatment provide the motivation for this benchmarking effort. The primary goal is to arrive at a simplified PDR model with which each code included in the project can agree. Eleven groups have participated in the benchmark tests: the Aikawa group (Lee et al. 1996), the Bensch group (Bensch et al. 2003), the CLOUDY group (Ferland et al. 1998), the COSTAR group (Kamp & Bertoldi 2000), the HTBKW group (Kaufman et al. 1999), the KOSMA group (Röllig et al. 2006b), the Leiden group (Black 1987), the Meijerink group (Meijerink & Spaans 2005), the Meudon group (Le Petit et al. 2002), the Sternberg group (Sternberg & Dalgarno 1995) and the UCL_PDR group (Bell et al. 2006a). The majority of the benchmark testing was conducted during a workshop at the Leiden Observatory in April 2004.

In the next section, the common differences between PDR models are summarized. In Section 2.2.3 the modifications needed to adapt the UCL_PDR code to the standard benchmark models are described. Section 2.2.4 presents the results of the benchmarking tests and Section 2.2.5 discusses the overall agreement of the codes, the improvements that have been made to the UCL_PDR code as a result of the benchmarking work and further improvements that could be made in the

future.

2.2.2 Differences between PDR models

Despite the separate evolution of these models, they all contain a number of physical and chemical processes that are generally agreed to be necessary in order to reproduce the fundamental features of a PDR. First and foremost, the penetration of FUV radiation into the cloud must be determined, since it is the diminishing FUV flux that controls most aspects of the PDR chemistry and thermal structure. Some consideration of the chemistry is required, the photoreactions that drive it being particularly important, and the shielding of H_2 and CO must also be accounted for in some way, if the positions of the H/H_2 and C^+/C/CO transition layers are to be correctly predicted. In addition, whilst the assumption of constant temperature is valid when modelling dark clouds, the heating within PDRs is coupled to the FUV flux and so changes with depth, producing a varying gas temperature profile that influences the chemistry and emission line strengths. An effort to determine the gas temperature must therefore be made, typically through some form of the thermal balance procedure described in Section 2.1.5. This also requires a number of heating and cooling processes to be included in the model.

The calculation of these three key processes — FUV attenuation, photochemistry and thermal balance — are then generally accepted as the basis of all PDR models and are present in all but one of the codes involved in the benchmarking effort (the LEE96MOD code did not calculate the thermal balance at the time of the benchmarking workshop). This then establishes the common ground upon which each code is based. The choice of which additional physical effects to include and how best to implement them are motivated by the intended use of the model and introduce differences between the codes.

Model geometry

The first point of departure from this common ground lies in the choice of geometry adopted by each model to describe the PDR. The complexity of the problem means that the majority of models reduce the PDR to a one-dimensional structure; that is, one line of sight through the cloud, normal to its surface. All physical quantities are then expressed as a function of depth into the cloud. The last 5 years have seen the development of several models that go beyond the limitations of one-dimensionality, treating the structure of the PDR in either two or three dimensions. However, these models were not included in the benchmarking effort, primarily because they were in the

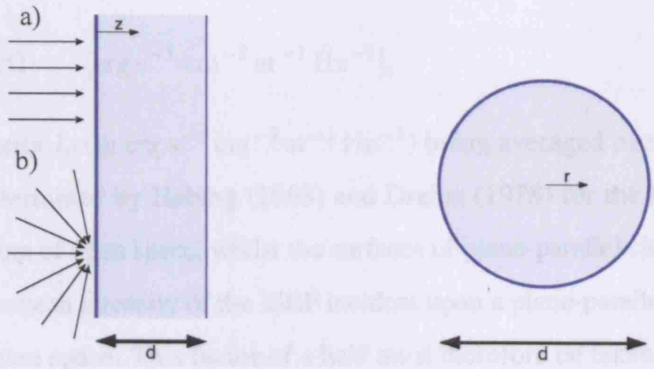

Figure 2.1: Common geometries adopted by PDR models. Plane-parallel (left) and spherical (right). The surface of either cloud can be illuminated by a) uni-directional or b) isotropic radiation. *Source: Röllig et al. (2006a).*

early stages of development at the time of the Leiden workshop. Within the community of one-dimensional models, there are two cloud geometries that are most commonly used, plane-parallel and spherical (see Figure 2.1). The majority of codes employ a plane-parallel geometry, with depth z measured perpendicular to the cloud surface. The additional assumption that the cloud is infinitely thick in the direction parallel to the surface simplifies the radiative transfer problem significantly. Plane-parallel clouds can be illuminated from either one side (semi-infinite) or both (finite) and the incident radiation can be either uni-directional or isotropic. In the case of semi-infinite plane parallel geometry, the cloud depth z reaches to infinity in the inwards direction and radiation can only enter or leave the cloud through the outer surface (at $z = 0$). Finite plane-parallel models allow radiation to pass through both the near and far sides of the cloud, making the calculation of the radiative transfer somewhat more complicated.

In the case of spherical geometry, one-dimensional models assume spherical symmetry and calculate the PDR properties along a radial line of sight. As with finite plane-parallel models, the transfer of radiation through the far side of the cloud must be accounted for. It is straightforward to calculate the penetration of isotropic FUV radiation into the spherical cloud, since the angular dependence of the radiative transfer vanishes, but the case of uni-directional FUV radiation is more complicated.

The incident FUV radiation field is often described in terms of the mean intensity (or energy

density), given by:

$$J_\nu = \frac{1}{4\pi} \int I_\nu \, d\Omega \qquad [\mathrm{erg\,s^{-1}\,cm^{-2}\,sr^{-1}\,Hz^{-1}}], \tag{2.2}$$

with the specific intensity I_ν (in $\mathrm{erg\,s^{-1}\,cm^{-2}\,sr^{-1}\,Hz^{-1}}$) being averaged over the solid angle Ω. The average fluxes determined by Habing (1968) and Draine (1978) for the ISRF are evaluated over the full 4π steradian of open space, whilst the surfaces of plane-parallel clouds are exposed to only 2π steradian. The mean intensity of the ISRF incident upon a plane-parallel cloud is therefore *half* that quoted for open space. This factor of a half must therefore be taken into account in all photoreaction rates.

The choice of uni-directional or isotropic incident FUV radiation has implications for the calculation of its attenuation by dust. The attenuation of FUV radiation (uni-directional or isotropic) was derived for both plane-parallel and spherical cloud geometries by Flannery et al. (1980) using the spherical harmonics method. The resulting expression for the case of a semi-infinite plane-parallel cloud was described in Section 1.3. Neglecting scattering, the attenuation of isotropic radiation in a spherical cloud is

$$J/J_0 = E_2(\tau) = \int_0^1 \frac{\exp\left(-\tau\mu\right)}{\mu^2} d\mu, \tag{2.3}$$

where τ is the optical depth of the dust, $\mu = \cos\theta$ is the cosine of the angle between the radiation direction and the line of sight and $J_0 = I_0(\mu) = \textit{constant}$ for isotropic radiation. In order to compare the results of spherical cloud models with those of plane-parallel models, it is necessary to rescale them to the same depth scale. This can be achieved by defining an *effective* visual extinction,

$$A_{V,\mathrm{eff}} = \frac{-\ln\left[E_2(k_{\mathrm{UV}} A_V)\right]}{k_{\mathrm{UV}}}, \tag{2.4}$$

where A_V is the visual extinction perpendicular to the surface in the spherical cloud model and $\tau_{\mathrm{UV}} = k_{\mathrm{UV}} A_V$. All benchmarking results are given in $A_{V,\mathrm{eff}}$ to allow models with both geometries to be directly compared.

Chemistry

The chemistry in PDRs plays a vital role in governing their temperature profiles and emission strengths, which conversely have an influence on the chemistry itself. The choice of which species and reactions to include in the chemical network therefore have a significant and sometimes unintuitive impact on the PDR properties, and can lead to very different results from otherwise similar models. Various factors guide these decisions, from computational constraints to specific

requirements for the intended application of the model. For example, the chemical processes relevant to PDRs in planetary nebulae are somewhat different to those in diffuse clouds.

Certain key species are known to have a critical effect on the chemistry. The inclusion of sulphur, for example, provides an important additional formation route for neutral carbon through charge transfer with C^+ near the location of the C^+/C/CO transition layer (Sternberg & Dalgarno 1995, see Section 1.4.4), in addition to contributing to the ionization fraction (electron density), particularly at greater depths where carbon is no longer ionized. Similarly, the inclusion of PAHs in the chemical network causes the transition from predominantly ionized to predominantly atomic carbon to occur nearer the surface (Bakes & Tielens 1998). The internal energy of vibrationally excited molecular hydrogen (H_2^*) may allow it to overcome the activation barrier of some endothermic reactions, with important consequences for the chemical structure of the outer region of the PDR. However, the efficiency of these reactions is generally unknown and the correct treatment of H_2^* chemistry is still uncertain.

In addition to the open question of which species and reactions to include, relevant rates for these reactions must also be determined. There are a number of comprehensive databases available that contain comprehensive sets of rate coefficients appropriate for conditions in interstellar space, primary examples being the UMIST (Millar et al. 1997; Le Teuff et al. 2000), NSM/OHIO (Wakelam et al. 2004) and Meudon (Le Bourlot et al. 1993a) databases. These draw upon the results of both experimental and theoretical work when compiling their datasets and, when rates are uncertain, can differ in the value they adopt. The photodissociation of H_2 and CO proceed via line absorption and increasing opacity in these lines results in effective shielding that must also be treated. The level of detail considered in calculating this effect is also a matter of choice and can vary from analytic approximation to explicit treatment of the wavelength-dependent absorption.

On a more fundamental level, PDR codes differ in whether they treat the chemistry time-dependently or, more commonly, calculate only steady-state solutions. The additional computational expense necessary to model the changing chemistry is repaid by the ability to consider phenomena that evolve on short time-scales. The addition of gas-grain and grain surface reactions, whilst being an important consideration, also introduces further uncertainties.

Treatment of dust grains

The presence of dust is central to many of the key processes in PDRs. It controls the attenuation of the incident FUV radiation continuum, provides a surface on which the formation of molecular hydrogen can proceed and thermally couples the gas to the FUV field through photoelectric heating

and gas-grain collisions. It is also responsible for the bulk of the FIR emission from PDRs and, deeper within the cloud, supports large reservoirs of material in the form of icy mantles that can undergo grain surface reactions. The precise nature of these dust grains is, however, still a matter of discussion; their absorption and scattering properties have only been estimated for a limited number of lines of sight, the efficiency of H_2 formation on grain surfaces is not well known at the gas and dust temperatures found in PDRs, the photoelectric yields for grains and PAHs are uncertain and the efficiency of the photoelectric heating mechanism is poorly constrained. Such uncertainties lead to the adoption of a variety of plausible values for the dust grain properties, introducing differences in the calculation of the FUV attenuation, location of the H/H_2 transition and heating of the gas. Additional considerations, such as the backscattering of FUV photons within the cloud, can cause further disagreement between models.

Heating and cooling

In addition to the uncertainties in the photoelectric heating mechanism, other heating rates are also open to debate. The level of detail with which these rates are calculated can also cause differences between codes. For example, in the case of collisional de-excitation of vibrationally excited H_2, a detailed treatment of the level populations shows that the lower transitions cool the gas at temperatures above 800 K. The cooling of the gas through line emission depends on the adopted collisional and radiative rates for the coolant species and on the calculation of the radiative transfer (see below). The treatment of some emission lines can prove particularly problematic, the [O I] 63 μm line being a prime example, becoming very optically thick under certain conditions and acting as both a heat source and a coolant. Obviously, the decision to include or exclude certain heating or cooling mechanisms will also lead to differences between codes.

Radiative transfer

Treatment of the wavelength-dependent radiative transfer, both in the incident FUV field and the emitted FIR/submm lines will produce different results to models that only consider the average extinction of the FUV field or integrated intensities of the emission lines, since various approximations must be made when treating the radiation field as a whole. For example, a full treatment of the shielding of H_2 and CO from photodissociation requires the wavelength-dependent absorption to be calculated (see Section 1.4.2). Whilst approximations for the shielding functions are in reasonably good agreement with the detailed treatment, there will inevitably be certain conditions under which the approximations break down. The calculation of line emission within the

PDR also depends upon the choice of collisional and radiative data, which may be obtained from a number of sources and therefore represents another possible source of disagreement between models.

Table 2.4: List of codes participating in the benchmarking effort.

Name	Authors	References
AIKAWA	H.-H. Lee, E. Herbst, G. Pineau des Forêts, J. Le Bourlot, Y. Aikawa, N. Kuboi	Lee et al. (1996)
CLOUDY	G. J. Ferland, P. van Hoof, N. P. Abel, G. Shaw	Ferland et al. (1998); Abel et al. (2005); Shaw et al. (2005)
COSTAR	I. Kamp, F. Bertoldi, G.-J. van Zadelhoff	Kamp & Bertoldi (2000); Kamp & van Zadelhoff (2001)
HTBKW	D. Hollenbach, A. G. G. M. Tielens, M. G. Burton, M. J. Kaufman, M. G. Wolfire	Tielens & Hollenbach (1985a); Kaufman et al. (1999); Wolfire et al. (2003)
KOSMA-τ	H. Störzer, J. Stutzki, A. Sternberg, B. Köster, M. Zielinsky, U. Leuenhagen, M. Röllig	Störzer et al. (1996); Bensch et al. (2003); Röllig et al. (2006b)
LEE96MOD	H.-H. Lee, E. Herbst, G. Pineau des Forêts, E. Roueff, J. Le Bourlot, O. Morata	Lee et al. (1996)
LEIDEN	J. Black, E. van Dishoeck, D. Jansen, B. Jonkheid	Black & van Dishoeck (1987); van Dishoeck & Black (1988); Jansen et al. (1995)
MEIJERINK	R. Meijerink, M. Spaans	Meijerink & Spaans (2005)
MEUDON	J. Le Bourlot, E. Roueff, F. Le Petit	Le Bourlot et al. (1993a); Le Petit et al. (2002, 2006)
STERNBERG	A. Sternberg, A. Dalgarno	Sternberg & Dalgarno (1989, 1995); Boger & Sternberg (2005)
UCL_PDR	T. Bell, S. Viti, W.-F. Thi	Taylor et al. (1993); Papadopoulos et al. (2002); Bell et al. (2006a)

2.2.3 Decription of the benchmark models

In total, eleven PDR codes participated in the benchmarking effort, both during and after the workshop in Leiden. These codes are listed in Table 2.4. They constitute the majority of PDR codes in use at the time of the workshop and represent contributions from all major international groups involved in this area of research.

To enable direct comparison of results from the participating codes, a set of 8 benchmark models were proposed. Each group was required to modify their code to use the standardized parameters prescribed by these models, necessarily reducing the complexity and sophistication of the code in the process. This simplification is needed in order to achieve some level of understanding of the differences between the codes. The intention was not to produce realistic models of real astronomical objects. Although many of the benchmark model parameters were decided prior to the Leiden workshop, in reality, this was an interactive process, ongoing over the course of the benchmarking effort, with additional specifications being included in the benchmark models as it became apparent that more constraints were needed in order to converge on similar results. This section describes the details of these 8 benchmark models.

Table 2.5 lists the physical parameters that were adopted for each model. The 8 models cover the principal region of parameter space occupied by PDRs, accounting for low and high densities (10^3 and $10^{5.5}$ cm^{-3}) and FUV fields (10 and 10^5 Draine). The models comprise two distinct sets; 4 isothermal models in which the gas and dust temperatures are fixed at 50 K and 20 K, respectively (models F1–F4, 'F' denoting fixed temperatures), and 4 models in which the temperature profiles are determined by solving the thermal balance explicitly at all depths (models V1–V4, 'V' denoting variable temperatures). The fixed temperature models allow the treatment of the FUV radiation, cloud geometry and chemistry to be compared, removing the additional uncertainties introduced by the thermal balance, heating and cooling routines and allowing the causes of disagreement between the codes to be more easily diagnosed. Once the differences between the codes have been fully understood for the fixed temperature models, the second set of models including calculation of the thermal balance allow the differences in the adopted heating and cooling functions to be assessed. Aside from the parameters listed in Table 2.5, the benchmark specifications are common to all 8 models and are outlined below.

Table 2.5: Parameter adopted for the eight benchmark models.

Parameter	F1	F2	F3	F4	V1	V2	V3	V4
n (cm^{-3})	10^3	10^3	$10^{5.5}$	$10^{5.5}$	10^3	10^3	$10^{5.5}$	$10^{5.5}$
χ (Draine)	10^1	10^5	10^1	10^5	10^1	10^5	10^1	10^5
$T_{\rm gas}$ (K)	50	50	50	50	Variable	Variable	Variable	Variable
$T_{\rm dust}$ (K)	20	20	20	20	Variable	Variable	Variable	Variable

Table 2.6: Species included in the chemical network for the benchmark models.

Benchmark Model Chemical Species
H, H^+, H_2, H_2^+, H_3^+, He, He^+, e^-
O, O^+, OH, OH^+, H_2O, H_2O^+, H_3O^+, O_2, O_2^+
C, C^+, CH, CH^+, CH_2, CH_2^+, CH_3, CH_3^+,
CH_4, CH_4^+, CH_5^+, CO, CO^+, HCO^+

Benchmark model geometry

All benchmark models assume a plane-parallel geometry with unidirectional radiation field and treat the cloud as a semi-infinite slab of constant density n (i.e. number density of hydrogen nuclei in cm^{-3}). As discussed in Section 2.2.2, the assumption of semi-infinite geometry affects the calculation of photoreaction rates, introducing a factor of $\frac{1}{2}$ because radiation impinges on only one side of the cloud. The UCL_PDR code already employs this geometry, so few modifications were necessary, however, some of the photorates did not previously include the factor of $\frac{1}{2}$ (most importantly, the C photoionization rate). This has been corrected so that all the photorates in the code are consistent with the assumed geometry. Codes that model the PDR as a spherical cloud approximated the plane-parallel, semi-infinite geometry by assuming a very large cloud radius, such that the surface of the cloud is effectively flat and infinitely large in directions perpendicular to the line of sight and that the cloud is very optically thick so that radiation only escapes through its front surface.

Benchmark chemistry

The creation of a standard set of chemical species and reactions that could be implemented by all codes was an important step in the benchmarking process, allowing the individual treatment of the photoreaction rates in each code to be examined in the model results. A restricted chemical network containing 30 species was therefore adopted for the benchmark models to simplify the chemistry whilst still allowing key PDR features, such as the C^+/C/CO transition, to be reproduced. The gas-phase abundances used in the models, relative to total number of hydrogen nuclei, are $X(\mathrm{He}) = 1.0 \times 10^{-1}$, $X(\mathrm{C}) = 1.0 \times 10^{-4}$ and $X(\mathrm{O}) = 3.0 \times 10^{-4}$. All other elements are excluded from the models. The chemical reaction rates are taken from the UMIST99 astrochemical database (Le Teuff et al. 2000), with some modifications suggested by A. Sternberg. The complete list of species is given in Table 2.6 and the full reaction rate file is available from the PDR benchmarking website (`http://www.ph1.uni-koeln.de/pdr-comparison`).

Grain surface chemistry, other than the formation of H_2, is neglected for the purposes of benchmarking to avoid the additional complications introduced by different treatments. Vibrationally excited H_2^* and PAHs are also excluded from the chemistry. The canonical rate coefficient for the formation of H_2 on grains is adopted, namely,

$$R_{\mathrm{f}} = 3 \times 10^{-18} \sqrt{T} \qquad [\mathrm{cm^3\,s^{-1}}]. \tag{2.5}$$

In this form, $S(T, T_{\mathrm{d}})$ and $\eta(T_{\mathrm{d}})$ are both $\sim$1 and it is therefore assumed that every H atom that hits a grain sticks and reacts to form H_2. The UCL_PDR code was modified to accommodate these changes.

The benchmark models assume steady-state chemistry, primarily because most of the participating codes cannot treat the chemistry time-dependently, but also to avoid the added level of complexity that time-dependence might introduce. In the case of the UCL_PDR code, which is time-dependent, a model duration of 10^8 yr was adopted to ensure that the chemistry reached steady-state. Early tests using the UCL_PDR code with a model duration of 10^6 yr produced results that differed significantly from those of the other codes, since the chemistry does not reach steady-state on this time-scale.

Benchmark physical properties

To avoid the possibility of confusion when comparing model results, an effort was made to specify as many of the benchmark model parameters as possible, thus sacrificing some of the more advanced features of the codes in favour of less ambiguity. In addition to the physical parameters listed for

each benchmark model in Table 2.5, a cosmic-ray ionization rate of $\zeta = 5 \times 10^{-17}$ s^{-1} and a turbulent velocity of $v_{\rm turb} = 1$ km s^{-1} are assumed in all the benchmark models. The unattenuated photodissociation rates of H_2 and CO in a unit Draine field in open space (i.e. exposed to radiation over the full 4π steradians) are $R^0_{\rm H_2,diss} = 5.18 \times 10^{-11}$ s^{-1} and $R^0_{\rm CO,diss} = 2 \times 10^{-10}$ s^{-1}, respectively. For the case of $\chi = 10$ Draine, the H_2 photodissociation rate at the semi-infinite cloud surface is then $R_{\rm H_2,diss}(0) = 2.59 \times 10^{-10}$ s^{-1} (accounting for exposure to the radiation over 2π, rather than 4π, steradians). In codes capable of doing so, the H_2 photodissociation rate is instead calculated explicitly by summing over oscillator strengths, etc. Since the UCL_PDR code does not include such a treatment, the single value for the photodissociation rate $R_{\rm H_2,diss}$ is used.

The visual extinction perpendicular to the surface of the cloud (i.e., A_V, not $A_{V,\rm eff}$) is determined by

$$A_V = 6.289 \times 10^{-22} N_{\rm H}, \tag{2.6}$$

where $N_{\rm H}$ is the total column density of hydrogen nuclei from the surface to the current depth. For codes that do not explicitly treat the wavelength-dependence of the FUV attenuation, as is the case for the UCL_PDR code, the attenuation of the FUV radiation field is assumed to be

$$\chi(A_V) = \chi(0) \exp\left(-k_{\rm UV} A_V\right), \tag{2.7}$$

with $k_{\rm UV} = 3.02$ for all benchmark models. These relations replace the more flexible treatments used in the original UCL_PDR code that determined the attenuation based on the chosen grain absorption and scattering properties (see Section 1.3).

Benchmark heating and cooling

The collisional excitation rates and Einstein coefficients for the C II, C I and O I fine structure lines have been updated to use recent data from the Meudon group (Le Bourlot et al. 1993a). The collision partners for these three coolants are now H, H^+, H_2 (ortho and para), He and e^-. These new data were adopted by all groups for the purposes of benchmarking.

The choice of heating mechanisms is not specified in the benchmark models, with the exception of photoelectric heating, which is treated using the expression derived by Bakes & Tielens (1994). The other heating mechanisms included are therefore those typically implemented in the UCL_PDR code (see Section 2.1.6. The calculation of the dust temperature is also unspecified in the benchmark models, and is achieved in the UCL_PDR code using the expression derived by Hollenbach et al. (1991).

Table 2.7: Summary of the main parameters used in the benchmark models. Elemental abundances are quoted with respect to the total number of hydrogen nuclei.

Parameter		Value
Elemental helium abundance	$X(\mathrm{He})$	0.1
Elemental carbon abundance	$X(\mathrm{C})$	1×10^{-4}
Elemental oxygen abundance	$X(\mathrm{O})$	3×10^{-4}
Cosmic-ray ionization rate	ζ	$5 \times 10^{-17}\ \mathrm{s}^{-1}$
Turbulent velocity	v_{turb}	$1\ \mathrm{km\,s}^{-1}$
Visual extinction law	A_V	$6.289 \times 10^{-22} N_{\mathrm{H}}$
FUV dust attenuation	τ_{UV}	$3.02\, A_V$
H_2 formation rate on grains	R_{f}	$3 \times 10^{-18} \sqrt{T}\ \mathrm{cm}^3\,\mathrm{s}^{-1}$
H_2 photodissociation rate	$R^0_{\mathrm{H_2,diss}}$	$5.18 \times 10^{-11}\ \mathrm{s}^{-1}$
Number density of H nuclei	n	$10^3, 10^{5.5}\ \mathrm{cm}^{-3}$
Incident FUV intensity	χ	$10, 10^5$ Draine

Bug fixes to the UCL_PDR **code**

Heating due to collisional de-excitation of vibrationally excited H_2 is taken from Hollenbach & McKee (1979), with the expression for n_{cr} now corrected in the UCL_PDR code (the temperature-dependence was incorrectly taken to be $T^{1/2}$ previously, whereas it should be $T^{-1/2}$). An error in the dust temperature calculation has also been fixed (the value of ν_0, the frequency at which the dust absorption Q_{abs} reaches the large-particle limit, was quoted incorrectly) and the formulation of Hollenbach et al. (1991) is now correctly implemented.

This concludes the description of the benchmark model specifications, including the additions made during and after the workshop in Leiden. A summary of the most important benchmark model parameters is given in Table 2.7

2.2.4 Benchmark results

The prime purpose of this benchmarking effort was to arrive at a simplified set of benchmark PDR models for which each participating code could produce comparable results. It was also the intention to gain an understanding of the consequences of variations in the choice of treatment for certain key processes. The 8 benchmark models test the agreement of the codes over a fairly wide

range of parameter space. The main outcomes of the benchmarking effort are described in this section. The terms pre- and post-benchmark are used to signify the initial and final results of the benchmarking process, respectively. The pre-benchmark model results represent the first attempt by each group to adapt their code to the initial benchmark model specifications, prior to the Leiden workshop; the post-benchmark model results represent the final outcome of the benchmarking effort, following the resolution of problems in the codes and refinement of the benchmark model descriptions. All data and plots for the pre- and post-benchmark results are available from the PDR benchmarking website (`http://www.ph1.uni-koeln.de/pdr-comparison`).

Fixed temperature models: F1–F4

The assumption of a fixed gas temperature of 50 K in benchmark models F1 to F4 means that any differences in the number densities predicted by the codes can be traced to differences in the photoreaction rates, non-standard chemistry or numerical errors. The STERNBERG code departs slightly from the standard chemical network by including reactions involving vibrationally excited molecular hydrogen H_2^* and neglecting some of the more minor H_2 destruction routes. The MEUDON, CLOUDY, LEIDEN and STERNBERG codes treat the excitation and photodissociation of molecular hydrogen explicitly, calculating the local rovibrational level populations and determining the photodissociation rate by summing over all absorption lines. The CLOUDY code initially used the chemical network of Tielens & Hollenbach (1985a) and the radiative recombination rates of Abel et al. (2005) to produce the pre-benchmark results, but made the transition to the specified benchmark set of reactions and rates to produce the post-benchmark results. The CLOUDY pre-benchmark results displayed significant differences from those of the other codes, demonstrating the impact that changing the recombination rates can have on the chemistry, the number density of carbon being particularly affected. After changing to the benchmark model specifications, the CLOUDY post-benchmark results agree well with those of the other codes.

The H/H_2 transition layer is one of the most important characteristics of PDRs, governing the chemistry and physical properties within the structure. Figures 2.2 and 2.3 show the post-benchmark number densities of atomic and molecular hydrogen as a function of $A_{V,\mathrm{eff}}$ for the fixed temperature benchmark models F1 and F4, respectively. The vertical lines on each figure mark the minimum and maximum transition depths for the pre-benchmark (dashed lines) and post-benchmark (solid lines) results. For model F1, the range of predicted transition depths decreased from $\Delta A_{V,\mathrm{eff}} \approx 0.2$ mag in the pre-benchmark results to $\Delta A_{V,\mathrm{eff}} \approx 0.06$ mag in the post-benchmark results, over a factor of 3 reduction in the spread. For model F4, the range of predicted transition depths decreased from

$\Delta A_{V,\mathrm{eff}} \approx 5$ mag to $\Delta A_{V,\mathrm{eff}} \approx 0.4$ mag, representing almost an order of magnitude reduction in the scatter. This small spread of values demonstrates that the codes generally now agree on the location of the H/H_2 transition ($A_{V,\mathrm{eff}} \sim 0.1$ and 1 mag for models F1 and F4, respectively). This result is a significant achievement in the development of a consensus model. The majority of the codes also produce H and H_2 number densities in close agreement at the surface and inner regions ($A_{V,\mathrm{eff}} \sim 10$ mag) of the cloud, and that follow the same general trend at intermediate depths. It is encouraging to see that the UCL_PDR code gives results that fall in the centre of the spread of values. However, the MEUDON code produces a significantly lower H_2 number density at the cloud surface in the high density, high FUV radiation intensity model (F4; see Figure 2.3). This is due to the inclusion of backscattering of FUV photons and the explicit calculation of the H_2 photodissociation rate in the MEUDON code. The backscattered photons increase the local mean FUV intensity near the cloud surface, leading to a higher H_2 photodissociation rate and consequently a lower H_2 number density. This effect accounts for approximately 10% of the difference. The photodissociation rate is calculated by determining the local rovibrational level populations and summing over all absorption lines. This treatment is also included in the STERNBERG code, however, the different collisional and radiative data used by each code result in two key differences,

1. The MEUDON code predicts a higher population of excited states than the STERNBERG code.
2. Dissociation from excited rotational levels increases rapidly with J in the MEUDON data.

These differences lead to dissociation probabilities a factor of 2–3 higher in the MEUDON code and are the primary cause of the lower H_2 number density near the surface. Due to the structure of the MEUDON code, these features could not be disabled. The difference between the H_2 photodissociation rates calculated by the STERNBERG and MEUDON codes illustrates the important influence that the choice of rate data can have on results. The variation in calculated photorates is discussed in more detail later on.

The atomic hydrogen number density deep inside the cloud ($A_{V,\mathrm{eff}} \sim 10$ mag) shows some degree of variation from code to code. This scatter is present in all 4 fixed temperature models (see Figures 2.2 and 2.3). Most noticeable is the lower H number density produced by the STERNBERG code. In this code, the H_2 chemistry is restricted, including only grain surface formation, photodissociation and destruction by cosmic-rays; other destruction routes for H_2 are neglected. The other codes incorporate the additional reactions

$$\mathrm{H_2 + H_2^+ \rightarrow H_3^+ + H} \qquad k = 2.08 \times 10^{-9}\ \mathrm{cm^3\,s^{-1}}$$

$$\mathrm{H_2 + CH_2^+ \rightarrow CH_3^+ + H} \qquad k = 1.60 \times 10^{-9}\ \mathrm{cm^3\,s^{-1}}$$

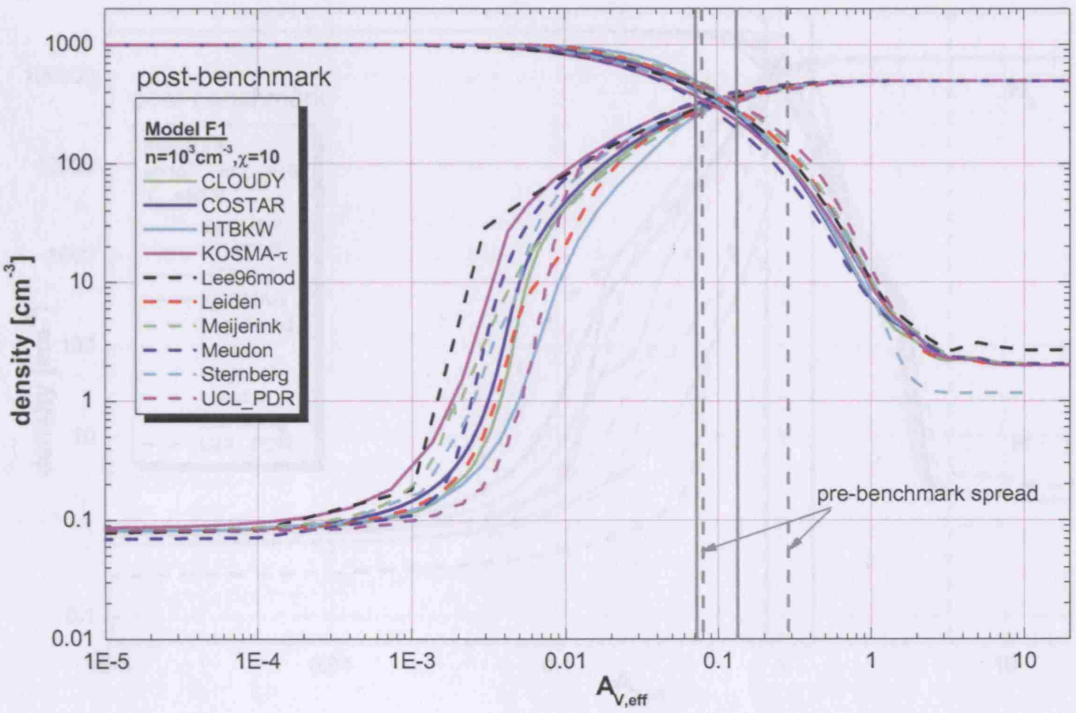

Figure 2.2: Benchmark model F1 ($n = 10^3$ cm^{-3}, $\chi = 10$ Draine, $T = 50$ K): Number densities (in cm^{-3}) of H and H_2 as a function of effective visual extinction ($A_{V,\mathrm{eff}}$) into the PDR for the participating codes. The dashed and solid vertical lines define the range of depths at which the H/H_2 transition occurs in the pre- and post-benchmark results, respectively. *Source: PDR comparison website.*

that contribute to the total H number density at high $A_{V,\mathrm{eff}}$. The omission of these reactions produces the lower H density in the STERNBERG results, demonstrating the sensitivity of the chemistry to changes in the reaction network. The reduced H_2 chemistry of the STERNBERG code also means that it fails to reproduce the slight kink in the H density profile at $A_{V,\mathrm{eff}} \approx 2$–3 mag in model F4 (Figure 2.3).

Another important feature of PDR chemistry is the appearance of the C^+/C/CO transition layer, marking the decline in carbon photoionization and CO photodissociation. and the gradual shift to dark cloud chemistry at greater depths. Figures 2.4 and 2.5 show the number densities of C^+, C and CO as a function of $A_{V,\mathrm{eff}}$ from the post-benchmark results for models F1 and F4, respectively. The vertical lines on each figure indicate the range of depths at which the maximum density is reached in the case of C and CO, and indicate the range of depths at which the number density has dropped by an order of magnitude in the case of C^+. Dashed vertical lines denote

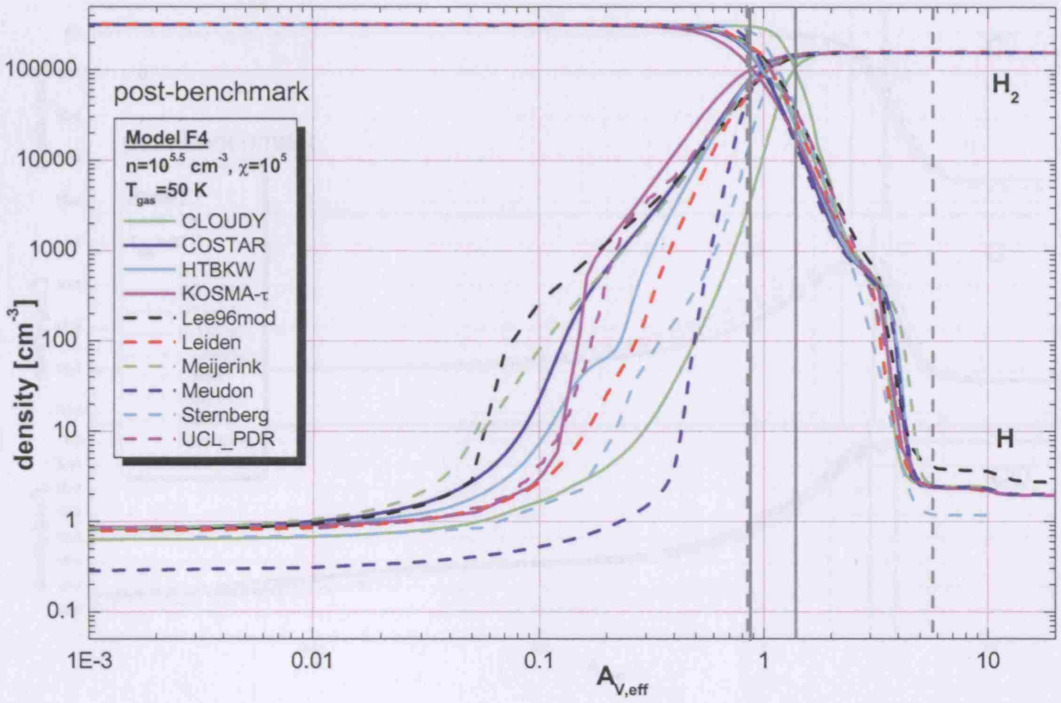

Figure 2.3: Benchmark model F4 ($n = 10^{5.5}$ cm^{-3}, $\chi = 10^5$ Draine, $T = 50$ K): Number densities (in cm^{-3}) of H and H_2 as a function of $A_{V,\mathrm{eff}}$ for the participating codes. *Source: PDR comparison website.*

the spread in the pre-benchmark values; solid vertical lines represent the reduced spread in the post-benchmark values. The scatter in the results for model F1 improves from $\Delta A_{V,\mathrm{eff}} \approx 2$–4 mag pre-benchmark to $\Delta A_{V,\mathrm{eff}} \approx 1$ mag post-benchmark and the scatter in model F4 results drops from $\Delta A_{V,\mathrm{eff}} \approx 3$–5 mag to $\Delta A_{V,\mathrm{eff}} \approx 1$ mag. The importance of the benchmarking workshop is again highlighted by these improvements.

There is now good general agreement between the codes for the densities of all three species in the post-benchmark results. However, the UCL_PDR and LEIDEN codes predict a slightly different behaviour for the C and C^+ number densities than is produced by the other codes. For these two codes, the number density of C is seen to peak marginally nearer the cloud surface, with a corresponding drop in C^+ density at that depth (see Figure 2.4). In addition, the UCL_PDR code predicts a peak C number density roughly 50% higher than that of the other codes. The shift in the C density peak is less apparent in the UCL_PDR results for model F4. A comparison with the photoionization rate of C calculated by each code (see the top right panel of Figure 2.6) shows that

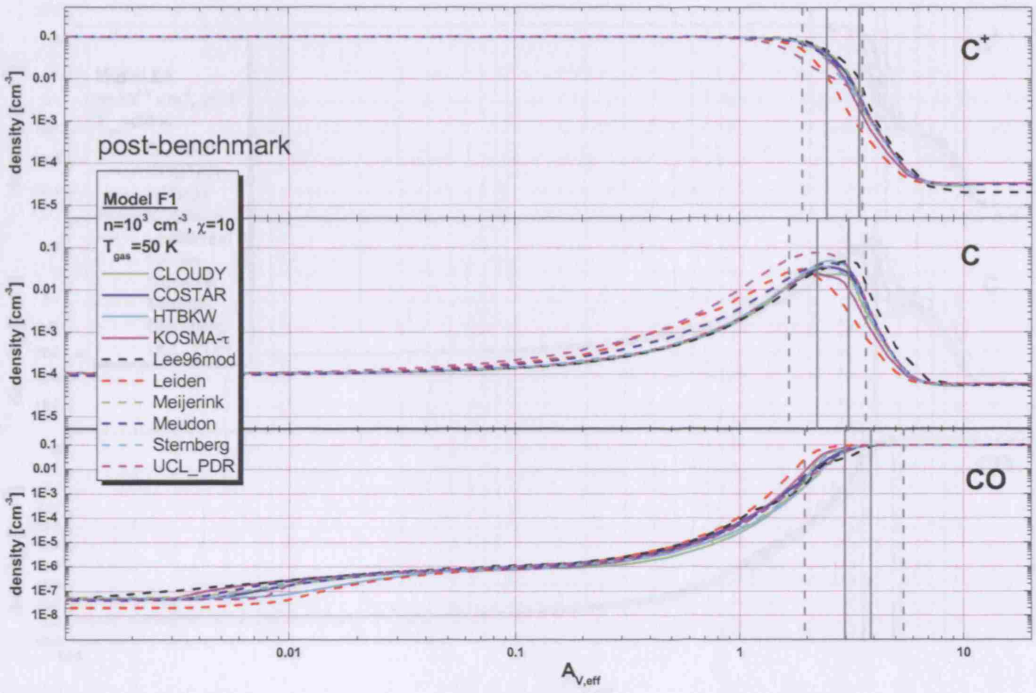

Figure 2.4: Benchmark model F1 ($n = 10^3$ cm^{-3}, $\chi = 10$ Draine, $T = 50$ K): Number densities (in cm^{-3}) of C^+, C and CO as a function of $A_{V,\mathrm{eff}}$, calculated by the participating codes. Vertical lines define the range of depths at which the the maximum number density is reached (in the case of C and CO) or at which the number density drops by a factor of 10 (in the case of C^+). Dashed vertical lines indicate the pre-benchmark range, solid vertical lines indicate the post-benchmark range. *Source: PDR comparison website.*

this behaviour is due to the increased shielding of the photoionization rate in these two codes. These differences are therefore attributable to the individual choice of shielding function in the codes. The increase in peak C number density produced by the UCL_PDR code may also be partly explained by the time-dependent treatment of the chemistry in this code. Initial pre-benchmark tests using a model duration of only 1 Myr were found to produce significantly higher C number densities than the steady-state codes. The slightly higher C density in the post-benchmark results may indicate that the chemistry has not quite reached equilibrium by 10^8 yr. The LEE96MOD results for model F4 show a small offset for the C^+ and C number densities at $A_{V,\mathrm{eff}} > 6$ mag. The dark cloud (i.e., $A_{V,\mathrm{eff}} \sim 10$ mag) number densities of C^+, C and CO agree very well, except for a somewhat lower C^+ density in the LEE96MOD results.

Figure 2.6 presents the post-benchmark rates for the photodissociation of H_2 (left-hand panels)

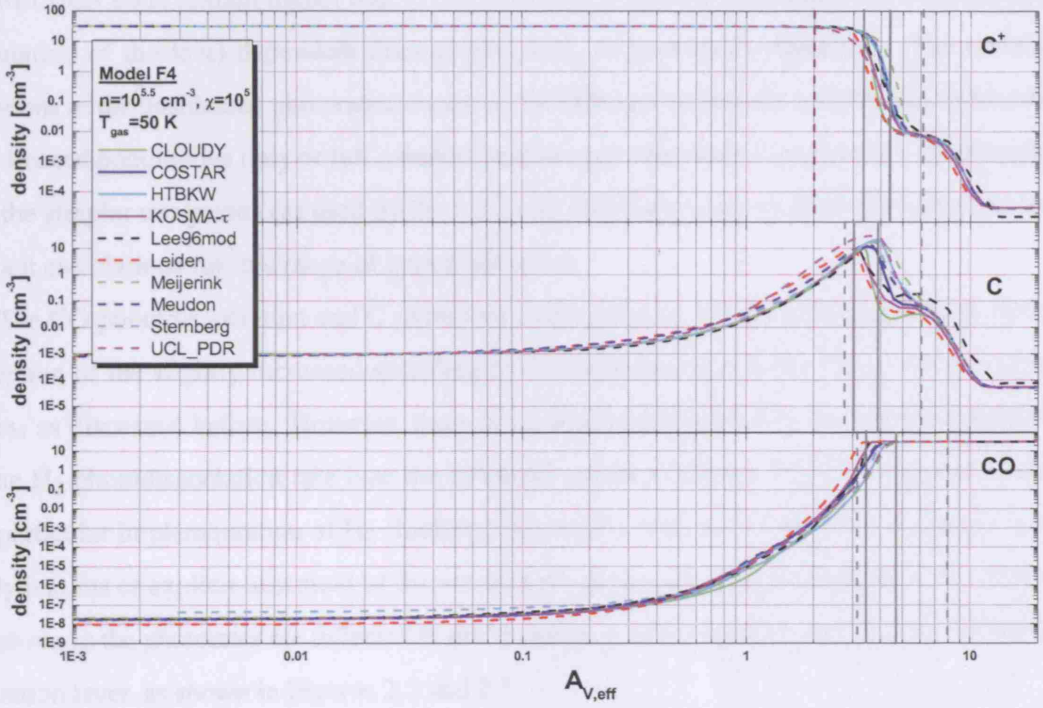

Figure 2.5: Benchmark model F4 ($n = 10^{5.5}$ cm^{-3}, $\chi = 10^5$ Draine, $T = 50$ K): Number densities (in cm^{-3}) of C^+, C and CO as a function of $A_{V,\mathrm{eff}}$, calculated by the participating codes. Vertical lines define the range of depths at which the the maximum number density is reached (in the case of C and CO) or at which the number density drops by a factor of 10 (in the case of C^+). Dashed vertical lines indicate the pre-benchmark range, solid vertical lines indicate the post-benchmark range. *Source: PDR comparison website.*

and CO (centre panels) and for the photoionization of C (right-hand panels), computed for models F1 (top) and F4 (bottom). In the pre-benchmark results (not shown), several codes, including the UCL_PDR code, calculated unshielded photorates at the surface of the cloud that were up to a factor of 2 higher than expected. This was largely due to the incorrect treatment of geometrical effects, specifically, failure to account for exposure to the incident radiation field over 2π steradians, rather than the full 4π steradians appropriate for open space. This was the case for the C photoionization rate in the UCL_PDR code. After correcting the error, the rate at the surface is now in agreement with the rest of the codes. The pre-benchmark rates of the KOSMA-τ code were slightly shifted toward lower A_V because of incorrect scaling between A_V and $A_{V,\mathrm{eff}}$ and an incorrect calculation of the angle-averaged photorates (the code assumes spherical geometry and isotropic FUV illumination). The post-benchmark results (Figure 2.6) show that most of these deviations have been corrected

and that the rates are generally in good agreement. The unshielded H_2 photodissociation rates of the MEUDON code remain higher due to the inclusion of photon backscattering and the explicit calculation of the level-dependent dissociation rates, as previously discussed. The remaining variations in the unshielded photorates are due to the different treatments used by the codes (single rate, limited populations only or full solution) and the fact that these variations are small suggests that the simpler treatments (as used by the UCL_PDR code) are a reasonable approximation to the explicit calculations for this range of parameter space.

The CO photodissociation and C photoionization rates are in very good agreement, with the exception of the slightly increased shielding of C photoionization in the UCL_PDR and LEIDEN codes, as discussed before. However, there is a considerable spread in the shielding behaviour of the H_2 photodissociation rate (see the left-hand panels of Figure 2.6). This spread is due to the particular implementation of H_2 shielding adopted by each code (tabulated shielding factors, analytical fits or explicit treatment of the wavelength-dependent radiative transfer). The resulting variations in the photorates are reflected in the H and H_2 number densities and location of the H/H_2 transition layer, as shown in Figures 2.2 and 2.3.

The pre- and post-benchmark results for models F1–F4 demonstrate the success of the benchmarking effort in improving the agreement between the PDR codes, whilst highlighting the difficulties faced in reaching a consensus model. The pre-benchmark results displayed a significant degree of variation from code to code, much of which was corrected during the benchmarking process. However, we did not achieve identical results with the individual codes, despite the severe restrictions imposed by the benchmark models, and the many remaining uncertainties raise the need for a further in-depth study.

Variable temperature models: V1–V4

The introduction of the thermal balance calculation to determine gas temperature profiles in benchmark models V1 to V4 adds many new sources of uncertainty and the potential for disagreement between codes is therefore significantly larger. The process requires the computation of heating and cooling rates whose implementation are not specified by the benchmark models and which are coupled to the chemistry through the gas temperature. The scatter in model results from different codes is therefore expected to be large. In this section, the analysis of the benchmarking results will focus on the temperature profiles, heating and cooling processes and emission strengths, with less emphasis on the number densities and photorates, since these have already been discussed in detail. In addition, problems with numerical noise and code failures in the two high density models,

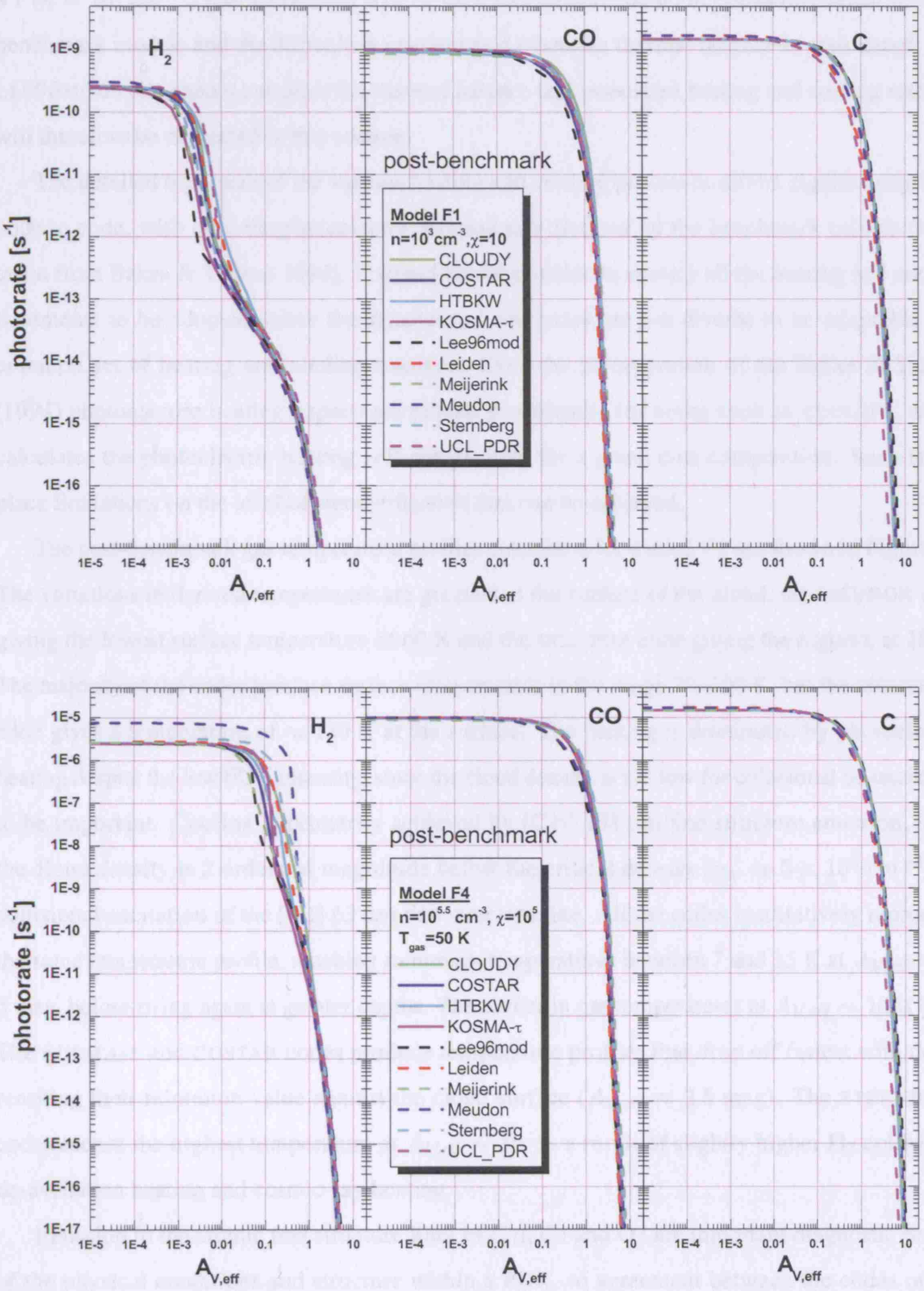

Figure 2.6: Benchmark models F1 ($n = 10^3$ cm^{-3}, $\chi = 10$ Draine, $T = 50$ K) & F4 ($n = 10^{5.5}$ cm^{-3}, $\chi = 10^5$ Draine, $T = 50$ K): Rates (in s^{-1}) of H_2 photodissociation (left-hand panels), CO photodissociation (centre panels) and C photoionization (right-hand panels) as a function of $A_{V,\mathrm{eff}}$ for the participating codes. *Source: PDR comparison website.*

V3 and V4 ($n = 10^{5.5}$ cm^{-3}) mean that their results are difficult to interpret. The results for model V1 ($n = 10^3$ cm^{-3}, $\chi = 10$ Draine) will be used to illustrate the main points of interest in these benchmark models and the difficulties encountered when the thermal balance is considered. The LEE96MOD code cannot calculate the thermal balance and associated heating and cooling rates, so will therefore be neglected in this section.

The detailed treatment of the various heating and cooling processes differs significantly from code to code, with only the photoelectric heating rate dictated by the benchmark models (to be taken from Bakes & Tielens 1994). It would not be possible to specify all the heating and cooling treatments to be adopted, since the structure of the codes are too diverse to be adaptable to a common set of heating and cooling routines. Even the incorporation of the Bakes & Tielens (1994) photoelectric heating expression proved problematic for codes such as CLOUDY, which calculates the photoelectric heating self-consistently for a given dust composition. Such issues place limitations on the level of standardization that can be achieved.

The post-benchmark gas temperature profiles calculated for model V1 are shown in Figure 2.7. The variations in derived temperature are greatest at the surface of the cloud, the MEUDON code giving the lowest surface temperature of 60 K and the UCL_PDR code giving the highest, at 180 K. The majority of the codes produce surface temperatures in the range 70–100 K, but the MEIJERINK code gives a temperature of $\approx$ 130 K at the surface. The heating is dominated by photoelectric heating despite the low FUV intensity, since the cloud density is too low for collisional de-excitation to be important. Cooling is primarily achieved by [C II] 158 μm fine structure emission, since the cloud density is 2 orders of magnitude below the critical density ($n_{\rm cr} \approx 5 \times 10^5$ cm^{-3}) for collisional excitation of the [O I] 63 μm fine structure line. All the codes qualitatively reproduce the same temperature profile, reaching minimum temperatures between 7 and 15 K at $A_{V,\rm eff} \approx 2$–5 mag, before rising again at greater depths. The scatter in gas temperatures at $A_{V,\rm eff} \sim 10$ is 20 K. The KOSMA-τ and COSTAR codes produce temperature profiles that drop off fastest with depth, reaching their minimum value nearest the cloud surface ($A_{V,\rm eff} \approx 2.5$ mag). The STERNBERG code reaches the highest temperature at $A_{V,\rm eff} \sim 10$, as a result of slightly higher H_2 collisional de-excitation heating and cosmic-ray heating.

Emission in the atomic fine structure lines of C II, C I and O I are important diagnostic probes of the physical conditions and structure within a PDR, so agreement between the codes on the emissivities and surface brightnesses of these lines is an important goal of the benchmarking. The emissivities of the atomic fine structure lines and the photoelectric heating rates for benchmark model V1 are shown in Figures 2.8 and 2.9. There are large scatters in the emissivities and PE

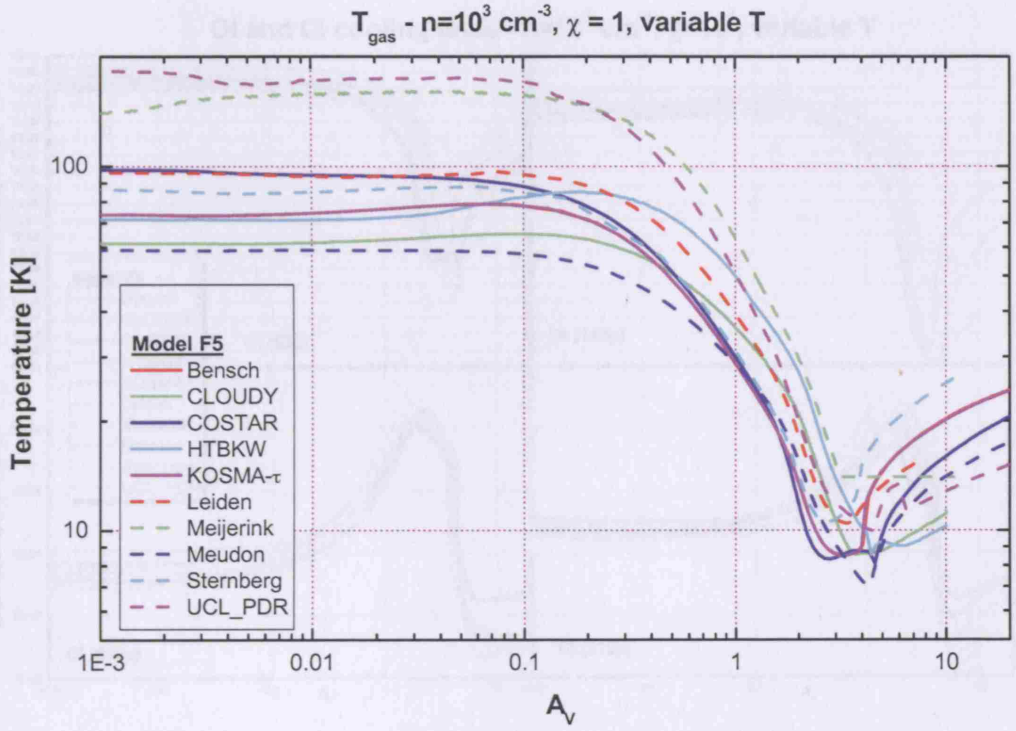

Figure 2.7: Benchmark model V1 ($n = 10^3$ cm^{-3}, $\chi = 10$ Draine): Gas temperature (in K) as a function of $A_{V,\mathrm{eff}}$ for the participating codes (post-benchmark results). *Source: PDR comparison website.*

heating rates for each code.The same collisional and radiative rates for the atomic fine structure lines (Le Bourlot et al. 1993a) are adopted by each code as part of the benchmark model, as is the expression for photoelectric heating (Bakes & Tielens 1994), therefore the difference in emissivities and photoelectric heating rate (assuming no numerical errors) are due to the gas temperature and the calculation of level populations and radiative transfer in each code. Given the fairly large scatter, it is hard to draw many useful comparisons from the emissivities, although the codes do reproduce the same overall behaviour. Figure 2.10 plots the surface brightnesses produced by each code for the main atomic fine structure lines in benchmark model V1. For spherical PDR codes, the surface brightness averaged over the projected area of the cloud is shown. The scatter is fairly small for the [C II] and [C I] lines (typically a factor of 3 to 5 variation), however the [O I] lines display a significant amount of variation between the codes, with over an order of magnitude difference in the predicted brightnesses of the UCL_PDR and CLOUDY codes.

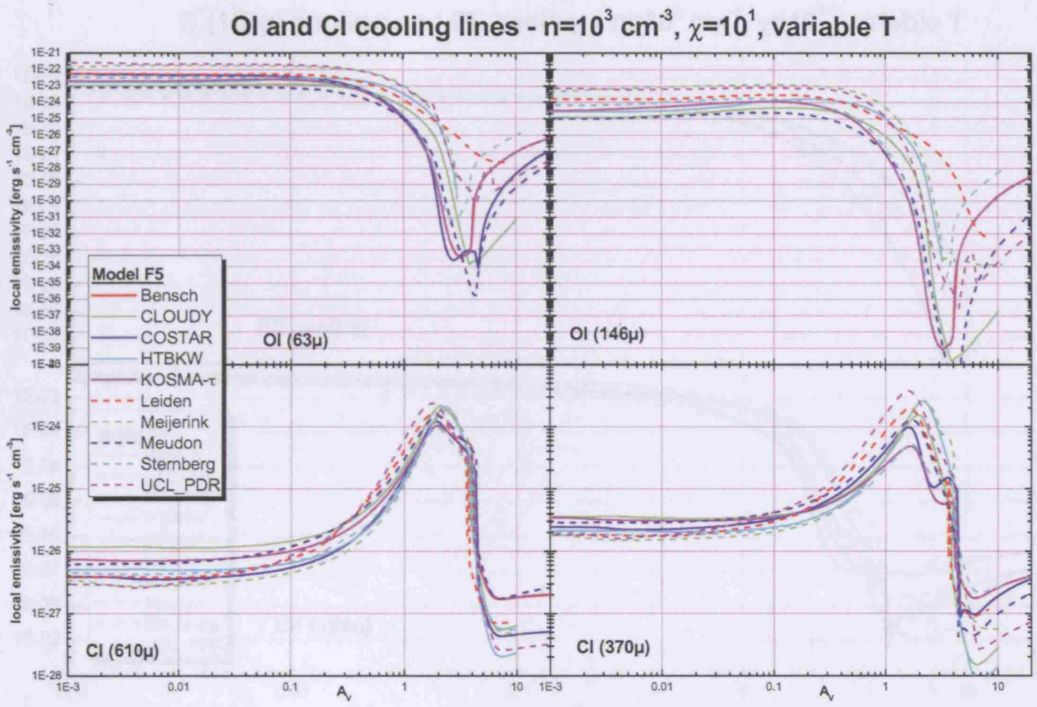

Figure 2.8: Benchmark model V1 ($n = 10^3$ cm^{-3}, $\chi = 10$ Draine): Local emissivities (in erg s^{-1} cm^{-3}) of the [O I] 63 μm (top-left), [O I] 146 μm (top-right), [C I] 610 μm (bottom-left) and [C I] 370 μm (bottom-right) fine structure lines as a function of $A_{V,\mathrm{eff}}$ for the participating codes (post-benchmark results). *Source: PDR comparison website.*

2.2.5 Discussion and conclusions

PDR models have now been available for almost 30 years and are established as routine tools for the interpretation of observational data. Despite their widespread use, developers of such codes have been aware of the uncertainties inherent within them and of the existence of disagreements between codes. This PDR benchmarking effort represents an initial attempt to address some of these uncertainties and to evaluate the impact of differing treatments on the agreement of the codes. The primary aim of the workshop was to understand the mutual differences in the model results and to gain a better understanding of the key processes involved. The intention was to ultimately arrive at a simplified model description that could be adopted by the various PDR codes, such that each code would produce the same results. The results produced by the codes during the course of the benchmarking show that a consensus model can potentially be reached if severe simplifying assumptions are made. However, these treatments prescribed by the model mean that the results are

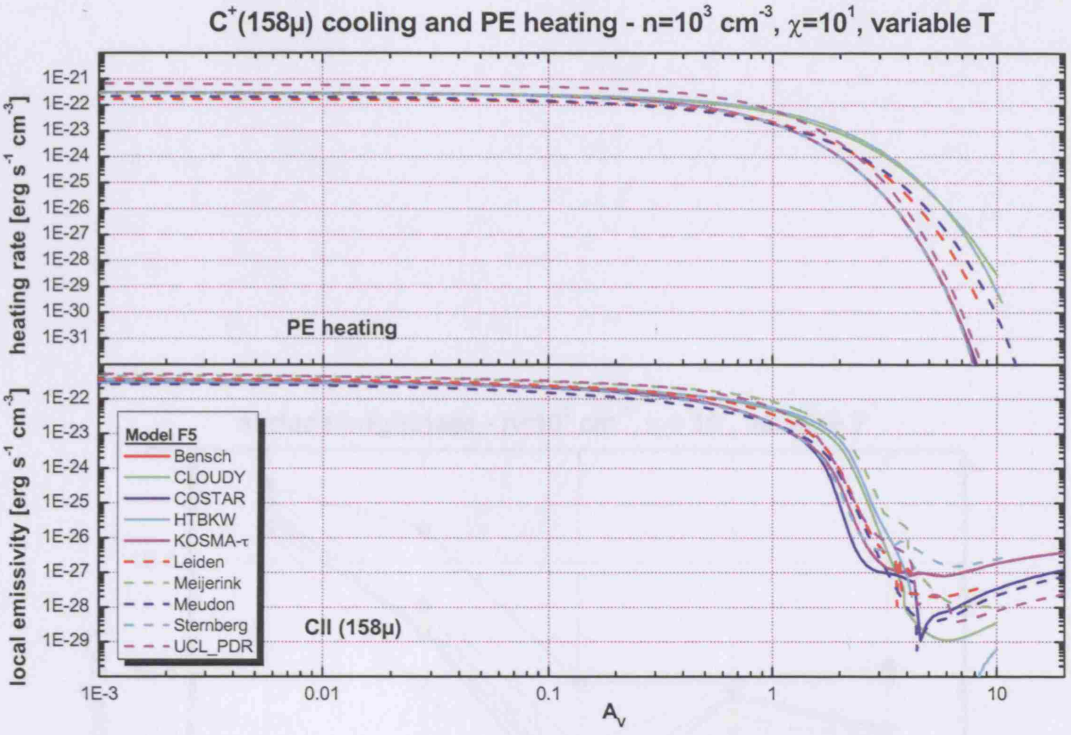

Figure 2.9: Benchmark model V1 ($n = 10^3$ cm^{-3}, $\chi = 10$ Draine): Photoelectric heating rate (in erg s^{-1} cm^{-3}) (top) and local emissivity (in erg s^{-1} cm^{-3}) of the [C II] 158 μm fine structure line (bottom), as a function of $A_{V,\mathrm{eff}}$ for the participating codes (post-benchmark results). *Source: PDR comparison website.*

likely to be less realistic. This process has also served to highlight various bugs in the codes that would otherwise have gone unnoticed.

If the condition of constant temperature is relaxed in the models, the complexity of the models grows significantly and it becomes much harder to disentangle the causes of disagreement between codes. Future study should focus on the thermal balance problem, clearly evident from the significant scatter in some of the results, and to understanding the importance of the various heating and cooling treatments on the model agreement.

Based on the results of the benchmarking effort, the reliability of the UCL_PDR code has been confirmed, and theoretical studies making use of it can be expected to produce sound results. The work that appears in subsequent chapters has been conducted with the benchmarked version of the code, with the exception of Chapter 6, which describes work that was ongoing at the time of the benchmarking and so did not benefit from the fully benchmarked model.

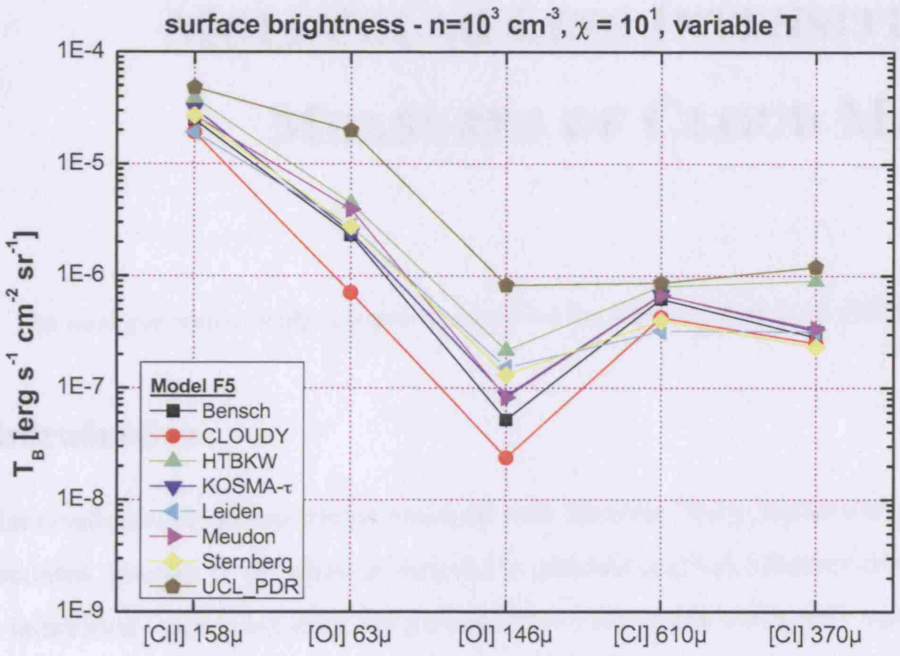

Figure 2.10: Benchmark model V1 ($n = 10^3$ cm^{-3}, $\chi = 10$ Draine): Surface brightnesses of the atomic fine structure lines (in erg s^{-1} cm^{-2} sr^{-1}) for the participating codes (post-benchmark results). *Source: PDR comparison website.*

CHAPTER 3

MOLECULAR LINE INTENSITIES AS MEASURES OF CLOUD MASSES

The work presented in this chapter is based on the paper by Bell et al. (2006a).

3.1 Introduction

Molecular clouds are the cradles within which all stars are born. They contain a significant, and often dominant, fraction of the gaseous material in galaxies and can influence the outcome of galactic interactions, providing effective cooling due to the highly dissipative nature of dense molecular gas. A reliable estimate of the molecular gas content in galaxies therefore plays a crucial role in determining their dynamical and star-forming properties. Accurate measurements of the molecular mass in galactic discs are required to derive the star formation efficiencies that are critical to models of galaxy evolution. Such measurements also play a vital role in understanding the properties of the interstellar medium in extragalactic environments. Furthermore, mapping the distribution of molecular gas in nearby galaxies allows their ongoing star formation activity, morphology and kinematic structure to be inferred.

Molecular hydrogen is the dominant molecular species in the Universe and governs the dynamical and chemical evolution of interstellar clouds. However, it lacks a permanent dipole moment and can only change ro-vibrational state through weak quadrupolar transitions with high excitation temperatures (above 500 K) that are subthermally populated and so difficult to detect in the cold bulk of the ISM. Furthermore, the pure rotational transitions of H_2 lie at mid-infrared wavelengths that are largely inaccessible from the ground, due to telluric absorption and strong background emission.

Alternative means of deriving the mass of molecular clouds have therefore been developed over the years. Many of these techniques make use of a tracer species (a molecule or dust) that is easier to detect and infer the molecular hydrogen content by some proportionality relation.

One of the most commonly used tracers of molecular gas is carbon monoxide (CO). After H_2, it is the most abundant molecule by several orders of magnitude and has been observed in all regions where molecular gas is thought to reside. Unlike molecular hydrogen, however, CO readily emits under the conditions typically found in molecular clouds. A weak dipole moment ($\mu = 0.11$ Debye) means that its rotational levels are easily excited by collisions with H_2 molecules, becoming thermalized at the densities and low temperatures appropriate for molecular clouds (the $J = 1 \rightarrow 0$ transition, for example, has a critical density of $\approx$300 cm^{-3} and an excitation temperature of 5.52 K). The lower rotational lines of CO have the added benefit of being easily observed at radio and submillimetre wavelengths with ground-based facilities. Together, these properties suggest CO emission to be an excellent tracer of molecular hydrogen.

The column density of molecular hydrogen along a line of sight is often related to the velocity-integrated intensity of the ^{12}CO($J = 1 \rightarrow 0$) rotational transition line using the CO-to-H_2 conversion factor:

$$X_{\rm CO} = \frac{N(\rm H_2)}{\int T_{\rm A}({\rm CO})\,{\rm d}v} \qquad [{\rm cm^{-2}\,(K\,km\,s^{-1})^{-1}}], \tag{3.1}$$

where $N(H_2)$ is the column density of H_2 and T_A(CO) is the antenna temperature of the CO(1–0) line. This has now become the standard method for inferring molecular gas content (see, e.g., reviews by Maloney 1990; Young & Scoville 1991; Combes 2000). The molecular mass within a cloud is then given by:

$$M = 1.6\,L_{\rm CO}\left(\frac{X_{\rm CO}}{10^{20}}\right) \qquad [M_\odot], \tag{3.2}$$

in which L_{CO} is the CO(1–0) luminosity of the cloud (K km s^{-1} pc^2). The total mass can be estimated by assuming all hydrogen is in H_2 and including a factor of 1.36 to account for the contribution from helium and heavy elements.

Observational estimates of X_{CO} can be derived for regions of the Milky Way and nearby galaxies where alternative methods for determining molecular cloud masses are available. Values of X_{CO} were first inferred using extinction measurements obtained from star counts to derive $N(H_2)$, assuming a constant gas-to-dust relationship, and comparing with observed CO luminosities (e.g. Dickman 1978; Frerking et al. 1982). Similarly, far-infrared emission can be used to estimate the cold dust mass and hence, through some assumed gas-to-dust mass ratio, the gas mass, and

comparison with CO luminosity can again yield values of $X_{\rm CO}$ (e.g. Guélin et al. 1995; Boselli et al. 2002a). Scoville et al. (1987) and Solomon et al. (1987) derived values of $X_{\rm CO}$ for a large sample of resolved giant molecular clouds with assigned kinematic distances by calculating their virial masses from CO linewidths. The same approach has more recently been applied to clouds within nearby galaxies (e.g. Rosolowsky et al. 2003; Rosolowsky & Blitz 2005). It should be noted that the values derived using this method are based on the assumption that the clouds are virialized. Maps of the diffuse γ-ray emission produced by interactions between cosmic-rays and hydrogen nuclei have been compared to H I and CO survey data for the Galactic plane to calculate the contribution of H_2 nuclei to the γ-ray emission and so calculate $X_{\rm CO}$ values along many lines of sight (Blitz et al. 1985; Bhat et al. 1986; Richardson & Wolfendale 1988; Bloemen 1989; Strong & Mattox 1996). The remarkable outcome of these studies is that the value of $X_{\rm CO}$ seems to be roughly constant for the Galactic molecular clouds that have been observed, and a canonical value is often adopted: $X_{\rm CO} \approx 2 \times 10^{20}$ cm^{-2} (K km s^{-1})$^{-1}$ (Strong & Mattox 1996; Dame et al. 2001). There have been several attempts to explain this apparent invariance, citing ensembles of virialized clouds (Dickman et al. 1986; Solomon et al. 1987) and clumpiness of the interstellar medium on scales of $A_V < 2$ mag (Taylor et al. 1993).

Despite the widespread use of this canonical value, there is strong evidence to suggest that $X_{\rm CO}$ can vary significantly under conditions differing from those in the Solar neighbourhood. Even within the Milky Way, observationally determined values for the X factor are found to vary with Galactocentric radius (Digel et al. 1990; Sodroski et al. 1995; Dahmen et al. 1998) and, further afield, estimates for $X_{\rm CO}$ in the Small and Large Magellanic Clouds are over an order of magnitude higher than the canonical value (Cohen et al. 1988; Rubio et al. 1993; Israel 1997). Conversion factors up to an order of magnitude lower than the canonical value have also been determined for a number of galactic nuclei (Smith et al. 1991; Israel & Baas 2001; Israel et al. 2006). Theoretical studies of the variation of the CO-to-H_2 ratio have also suggested that $X_{\rm CO}$ can be up to an order of magnitude higher or lower than the canonical value under certain conditions (e.g. Sakamoto 1996, 1999). Taylor et al. (1993) used a photon-dominated region (PDR) chemical model to perform *ab initio* calculations of $X_{\rm CO}$ and showed its variation for small changes in typical cloud parameters. Work along similar lines has also been conducted by Le Bourlot et al. (1993b), Wolfire et al. (1993) and Kaufman et al. (1999). These previous studies provide the foundation and motivation for this current work.

The bulk of CO emission occurs in the outer regions of molecular clouds ($A_V < 10$ mag), where the interstellar radiation field falls on the cloud surface. PDR models are therefore ideally

suited to the theoretical study of the $X_{\rm CO}$ factor, since they self-consistently compute the chemistry and thermal balance, and thus the column density of H_2 and emission strength of CO, within these regions. In this chapter we examine the influence of physical and chemical conditions on $X_{\rm CO}$ and attempt to explain its dependence on important physical parameters, such as the density, age, and metallicity of the cloud. In Section 3.2 we describe the models used to calculate and independently verify theoretical estimates of the CO-to-H_2 ratio for given physical conditions. Section 3.3 reviews the benchmarking results for important combinations of parameters when using the two PDR models and evaluates the reliability of subsequent, more extensive calculations. The effect of varying physical parameters is then discussed in depth in Section 3.4, before we summarize our conclusions in Section 3.5.

3.2 PDR models

3.2.1 The UCL_PDR code

We use the UCL_PDR time-dependent PDR code to compute the chemistry, thermal balance and CO(1–0) emission strength within the outer region ($A_V < 10$ mag) of a molecular cloud in order to derive theoretical values of the CO-to-H_2 ratio, $X_{\rm CO}$, for given physical parameters. The version of the code used for these calculations is described in Chapter 2. For the majority of the models considered here, steady-state conditions are determined by assuming a cloud age of 1 Gyr, however, the time-dependent evolution of the chemistry and emission are considered in a subset of models, in which the gas is initially taken to be in atomic form with all carbon singly ionized. The free parameters and their standard values adopted for the models are listed in Table 3.1.

The integrated intensity of the CO(1–0) line, calculated along the line of sight through the cloud, is given by:

$$I = \frac{1}{2\pi} \int \Lambda(z)\, {\rm d}z \qquad [{\rm erg\,s^{-1}\,cm^{-2}\,sr^{-1}}], \tag{3.3}$$

where $\Lambda(z)$ is the CO(1–0) line emissivity at depth z into the cloud (erg s^{-1} cm^{-3}) and the factor of $1/2\pi$ accounts for the fact that photons only emerge from the outer edge of the cloud, rather than over the full 4π steradians. The theoretical velocity-integrated antenna temperature is then

$$\int T_{\rm A}\, {\rm d}v = \frac{c^3}{2k\nu^3} I \qquad [{\rm K\,km\,s^{-1}}], \tag{3.4}$$

with ν being the transition frequency of the CO(1–0) line. The value of $X_{\rm CO}$ is therefore calculated at each depth point into the PDR using equation (3.1).

Table 3.1: Standard parameter values adopted for each cloud model.

Parameter		Standard Value
Number density of hydrogen nuclei	n	10^3 cm^{-3}
Incident FUV radiation field	χ	1 Draine
Cosmic-ray ionization rate	ζ	1.3×10^{-17} s^{-1}
Metallicity (relative to Solar)	Z	$Z_\odot$
Turbulent velocity	$v_{\rm turb}$	1 km s^{-1}
Age of the cloud	t	1 Gyr

3.2.2 The Meudon code

The Meudon PDR code self-consistently computes the steady-state chemical and thermal structure of the cloud, in addition to the emission strengths of the relevant cooling lines. The present benchmark calculations have been performed using an older version of the code (Abgrall et al. 1992; Le Bourlot et al. 1993a; Flower et al. 1994), in which self-shielding of H_2 and CO are computed using the approximation of Federman et al. (1979) and do not include the overlap between H_2 and CO predissociating lines. This has been demonstrated to be a reasonable approximation by Lee et al. (1996).

3.3 Benchmarking the X factor models

In order to assess the reliability of the model predictions in this work, the $X_{\rm CO}$ factor data produced by the UCL_PDR code have been benchmarked against the model results of the Meudon PDR code to check that the same trends are found in both. The Meudon code treats the microphysical processes within the cloud in more detail than the UCL_PDR code, but is more computationally intensive and less suited to examining large regions of parameter space. Therefore, to test the agreement between the two codes, we have selected six key models (listed in Table 3.2) that are representative of the parameter space being examined.

The same species set and reaction network have been used in both codes as part of the benchmarking process. The grain properties, extinction law and metallicity-dependence are also common to both codes, so that the results can be directly compared. Since the Meudon code computes steady-state chemistry, a cloud age of 1 Gyr has been used in the UCL_PDR code to approach chemical equilibrium.

Table 3.2: Benchmark model parameters. When not specified, the standard parameter values listed in Table 3.1 were used.

Model	Parameter
A	Standard Values
B	$n = 500\,\mathrm{cm}^{-3}$
C	$\chi = 10^3$ Draine
D	$\zeta = 1.3 \times 10^{-14}\,\mathrm{s}^{-1}$
E	$Z = 10^{-2}\,Z_\odot$
F	$v_{\mathrm{turb}} = 3\,\mathrm{km\,s}^{-1}$

Figure 3.1 shows the results of the benchmarking tests. The characteristic depth profile of the X_{CO} factor, seen in all these results, is discussed in Section 3.4. It must be stressed that exact agreement between the two codes is not expected, since their treatment of the physical processes is very different in some cases. Overall, agreement is good between the two codes, with X_{CO} profile minima generally differing by less than a factor of 2 across the visual extinction range considered here (see Table 3.3). The test models probe the influence of each parameter considered in this paper and both codes predict the same trend for the X_{CO} factor variation in each case. However, the Meudon code produces X_{CO} factor depth profiles with minima that are consistently lower and deeper into the cloud than those calculated by the UCL_PDR code. This can be attributed to the different treatments of the self-shielding used by the two codes in the attenuation of the CO photodissociation and C I photoionization rates. The Meudon code also considers the increased photodissociation rate of H_2 molecules in rovibrationally excited states, an effect neglected in the UCL_PDR code. The differences caused by the individual self-shielding treatments and the additional photodissociation of excited H_2 included in the Meudon code are most apparent in benchmark model C ($\chi = 10^3$ Draine; middle-left panel in Figure 3.1) where the FUV radiation is strong and the gas temperatures are high. These differences should be preserved, since they reflect the choice of treatment for this physical process and give an indication of the uncertainty inherent in calculations of theoretical X_{CO} factors. We regard the agreement between the codes as satisfactory and the exploration of parameter space reported below is made using the UCL_PDR code.

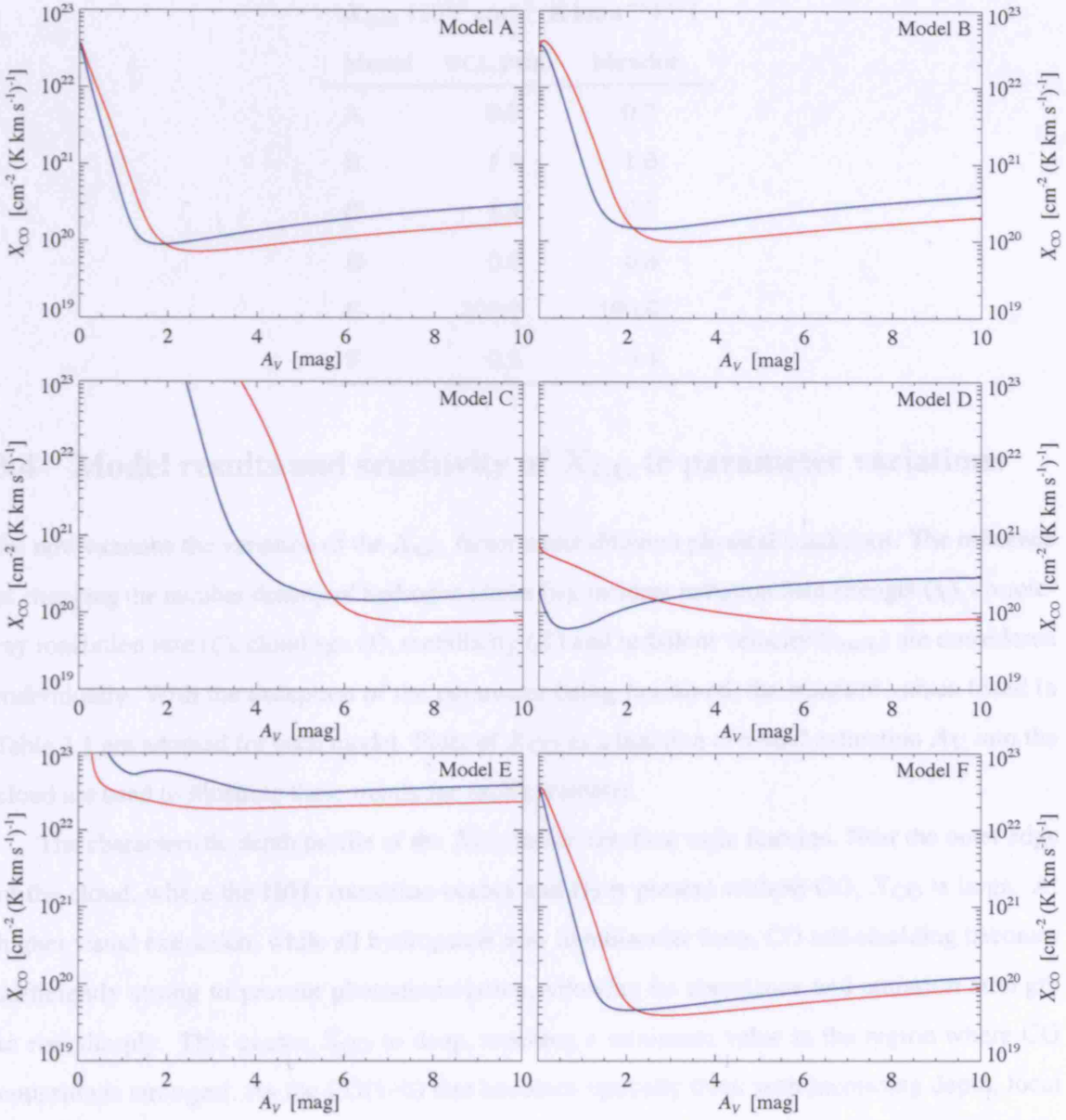

Figure 3.1: Benchmark model comparisons. $X_{\rm CO}$ as a function of visual extinction A_V, as calculated by the UCL_PDR (blue line) and Meudon (red line) codes, is plotted for models A (standard parameters), B ($n = 500$ cm^{-3}), C ($\chi = 10^3$ Draine), D ($\zeta = 1.3 \times 10^{-14}$ s^{-1}), E ($Z = 10^{-2}\,Z_\odot$) and F ($v_{\rm turb} = 3$ km s^{-1}), respectively.

Table 3.3: Minimum X_{CO} values obtained for the six benchmark models, as calculated by the UCL_PDR and Meudon codes.

X_{min} [10^{20} cm^{-2} (K km s^{-1})$^{-1}$]		
Model	UCL_PDR	Meudon
A	0.9	0.7
B	1.5	1.0
C	1.4	0.7
D	0.6	0.8
E	300.0	190.0
F	0.5	0.4

3.4 Model results and sensitivity of X_{CO} to parameter variations

We now examine the variation of the X_{CO} factor under different physical conditions. The influence of changing the number density of hydrogen nuclei (n), incident radiation field strength (χ), cosmic-ray ionization rate (ζ), cloud age (t), metallicity (Z) and turbulent velocity (v_{turb}) are considered individually. With the exception of the parameter being examined, the standard values listed in Table 3.1 are adopted for each model. Plots of X_{CO} as a function of visual extinction A_V into the cloud are used to illustrate these trends for each parameter.

The characteristic depth profile of the X_{CO} factor has three main features. Near the outer edge of the cloud, where the H/H_2 transition occurs and H_2 is present without CO, X_{CO} is large. At higher visual extinction, while all hydrogen is now in molecular form, CO self-shielding becomes sufficiently strong to prevent photodissociation, allowing its abundance and emission strength to rise sharply. This causes X_{CO} to drop, reaching a minimum value in the region where CO emission is strongest. As the CO(1–0) line becomes optically thick with increasing depth, local emission gradually declines and X_{CO} begins to rise slowly again. The minimum of the depth profile therefore represents the value of X_{CO} that would be observed for that particular environment, since it corresponds to the peak emission of the CO line (see Figure 3.2), with little contribution from deeper within the cloud. In what follows, the X_{CO} factor adopted for a particular model is taken as the value at the minimum in the X_{CO}–A_V plot. Under most conditions, X_{CO} profile minima tend to occur in the region $A_V < 2$ mag where freeze-out of atoms and molecules should not take place, therefore our decision to exclude it from the chemistry seems reasonable.

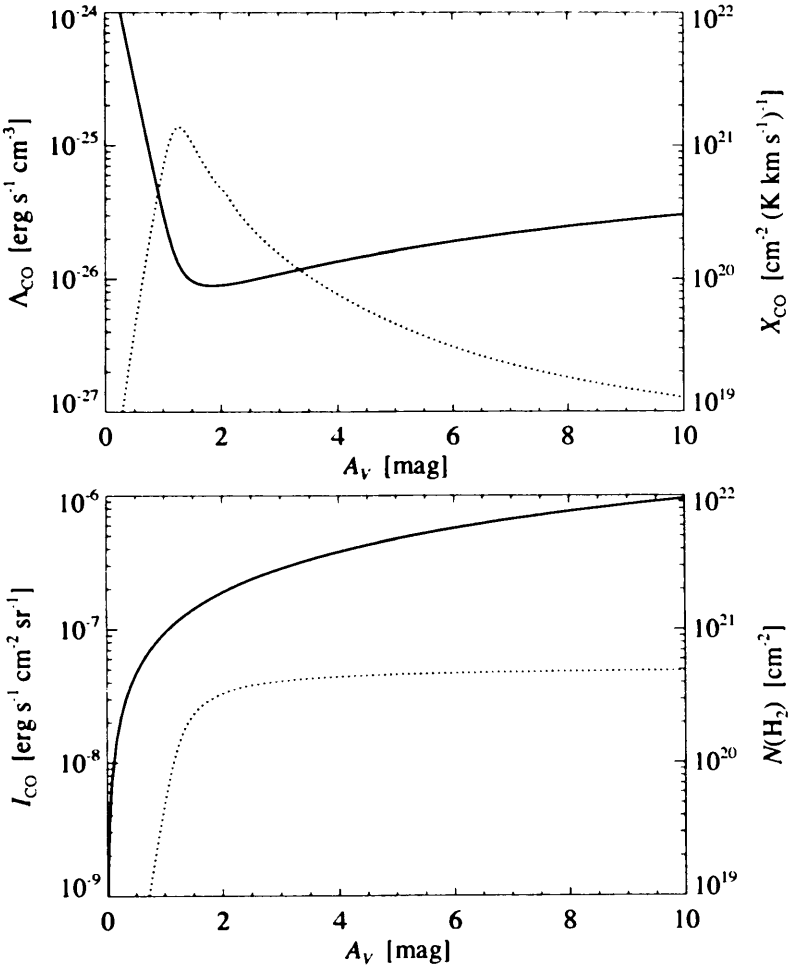

Figure 3.2: *Top*: X_{CO} profile calculated for the standard parameter values listed in Table 3.1. CO(1–0) emissivity (Λ_{CO}; dotted line) and X_{CO} (solid line) as a function of A_V into the cloud. *Bottom*: CO(1–0) integrated intensity (I_{CO}; dotted line) and H_2 column density (solid line) as a function of A_V into the cloud.

The lower panel of Figure 3.2 demonstrates that once the CO line has become optically thick, its integrated intensity reaches a constant value and is no longer sensitive to the monotonically increasing H_2 column density deeper into the cloud. Therefore, in the case of a slab of uniform density, the X_{CO} factor only provides a lower limit for $N(H_2)$. However, in reality, there is good evidence that at least some interstellar clouds are clumpy (Peng et al. 1998; Morata et al. 2005). In this case, the CO emission arises from an ensemble of clumps, each effectively optically thin. The total H_2 column density is then recovered using the X_{CO} factor method if clouds are clumpy on scales of $A_V \sim 1$ mag, as has been suggested (e.g. Taylor et al. 1993; Wolfire et al. 1993).

For our choice of standard physical parameters adopted in Figure 3.2, the derived value of X_{CO} would be about 1, rather than the canonical value of 2 for the Milky Way, in units of 10^{20} cm^{-2} (K km s^{-1})$^{-1}$. We note, however, that we could obtain $X_{CO} = 2$ with a variety of plausible parameter combinations, e.g., by setting the cloud number density to 400 cm^{-3}, or the cloud age to $\sim$1 Myr, or the turbulent velocity to 0.3 km s^{-1}. This degeneracy in reproducing the observed value shows that X_{CO} cannot be used to infer the physical conditions and, conversely, that using the canonical value in any situation without further consideration can be dangerous.

3.4.1 Gas density

Diffuse clouds containing reasonable quantities of molecular gas have hydrogen nuclei number densities $n \lesssim 100$ cm^{-3}, whilst giant molecular clouds have densities ranging from an average value of ~ 200 cm^{-3} up to 10^6 cm^{-3} in their cores (see, e.g., Scoville et al. 1987; Güsten 1989; Dyson & Williams 1997, and references therein). Therefore, we consider the sensitivity of X_{CO} to variations in density within the range $10^2 \leq n \leq 10^6$ cm^{-3}. For the purposes of comparison, we have adopted the simplifying assumption of constant density across the PDR in these models. The variation of X_{CO} with visual extinction for densities from 10^2 to 10^4 cm^{-3} is shown in Figure 3.3.

As the density increases from the lowest values considered, the minimum value of X_{CO} drops and the profile minimum gets sharper and shifts to lower A_V. The shielding of CO from photodissociation increases with gas density and allows its abundance to reach saturation nearer the surface of the cloud, resulting in stronger emission and therefore reducing the value of X_{CO}, which is inversely proportional to CO emission strength. At higher densities, the CO(1–0) line rapidly becomes optically thick with increasing depth, causing emission to occur within a thin region of the cloud (see Figure 3.4) and narrowing the minimum of the X_{CO} versus A_V profile. At densities above 10^4 cm^{-3} (not shown) the sharpening and deepening of the X_{CO} profile minimum becomes more exaggerated.

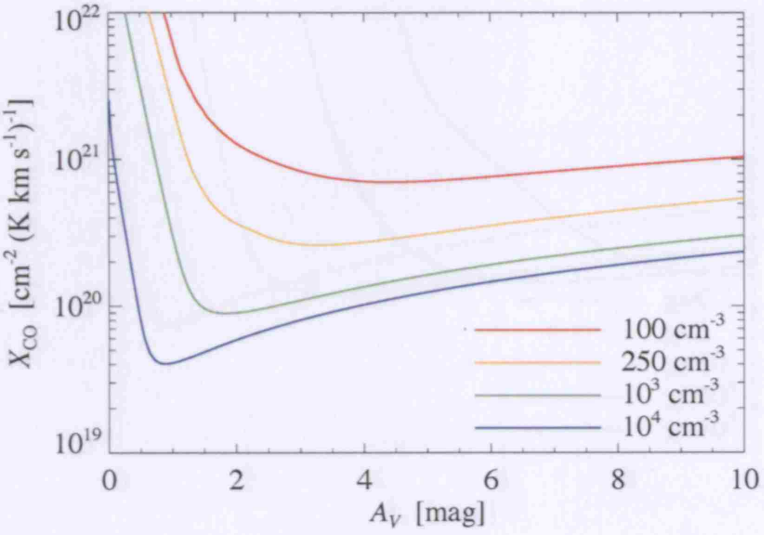

Figure 3.3: $X_{\rm CO}$ versus A_V profiles for varying number density of hydrogen nuclei within the cloud (n cm^{-3}).

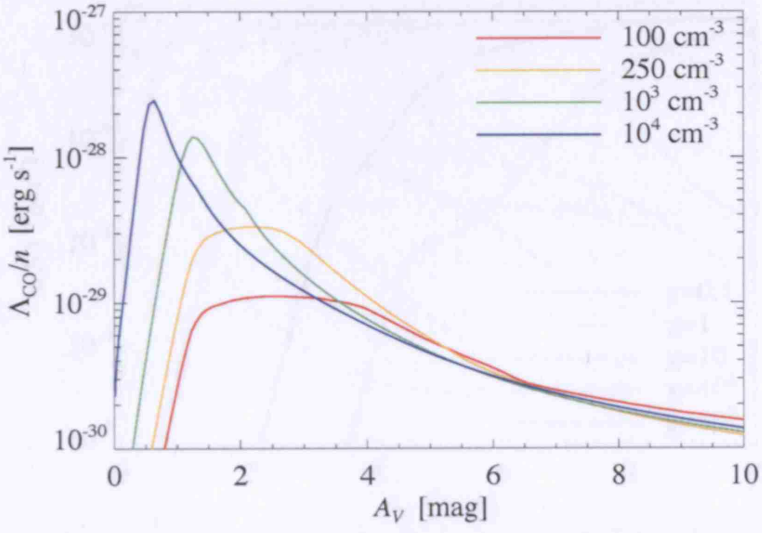

Figure 3.4: CO(1–0) emissivity divided by number density ($\Lambda_{\rm CO}/n$) as a function of visual extinction A_V for varying number density (n cm^{-3}).

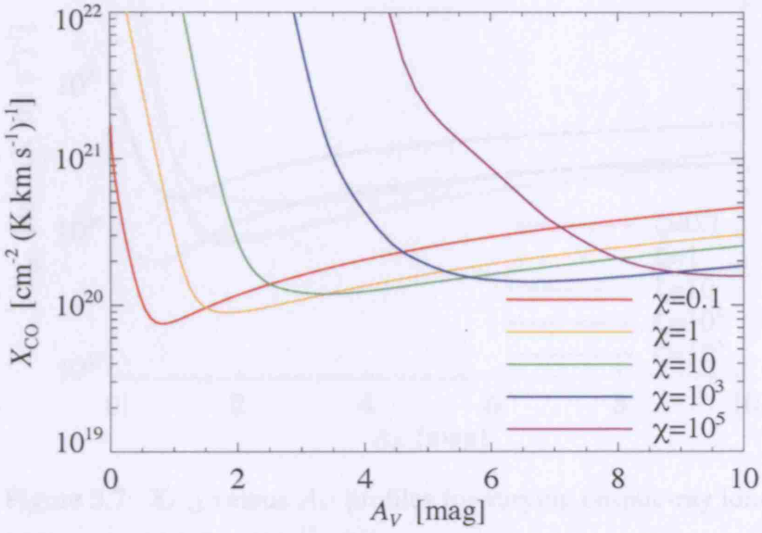

Figure 3.5: X_{CO} versus A_V profiles for varying incident FUV radiation field strength (χ Draine).

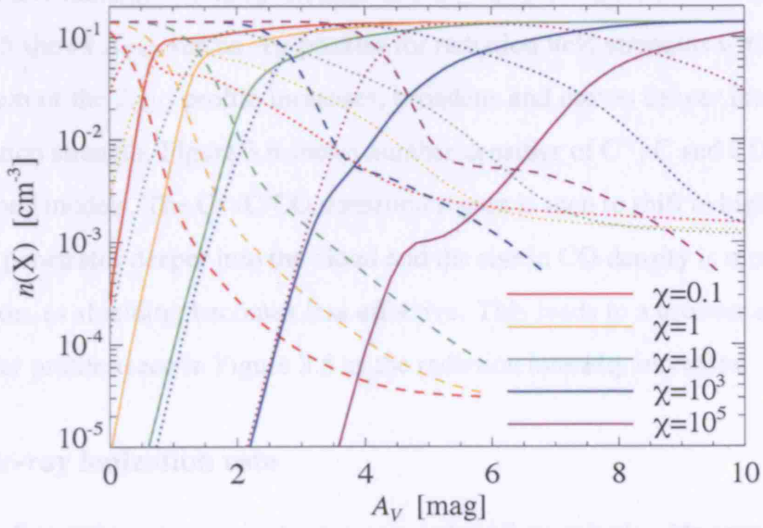

Figure 3.6: Number densities of C^+(dashed line), C (dotted line) and CO (solid line) as a function of A_V for varying incident FUV radiation field strength (χ Draine).

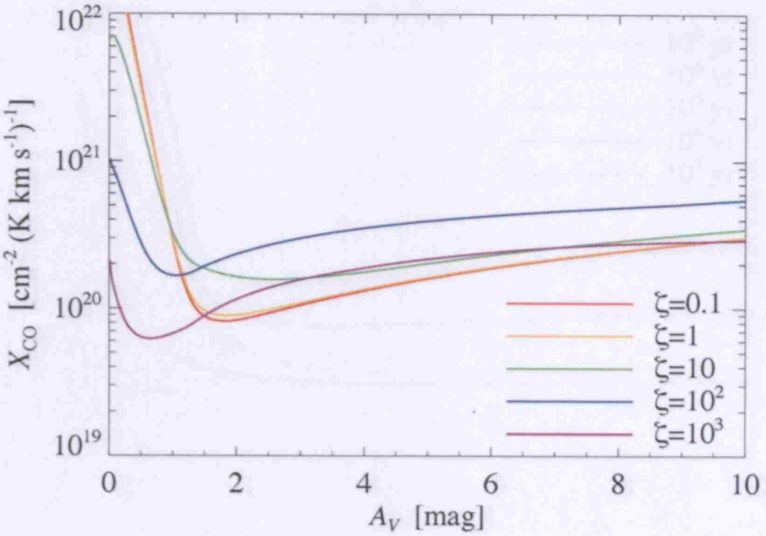

Figure 3.7: X_{CO} versus A_V profiles for varying cosmic-ray ionization rate (ζ 1.3×10^{-17} s^{-1}).

3.4.2 Radiation field strength

Radiation field strengths incident upon gas clouds can vary from a few times the standard interstellar Draine field up to $\chi \sim 10^7$ Draine in regions of intense star formation (see Hollenbach & Tielens 1999, and references therein). We adopt a range of $0.1 \leq \chi \leq 10^5$ Draine for consideration in this study. Figure 3.5 shows X_{CO} versus A_V profiles for radiation field strengths within that range.

The minimum of the X_{CO} profile increases, broadens and moves deeper into the cloud with increasing radiation strength. Figure 3.6 shows number densities of C^+, C and CO as a function of A_V for these cloud models. The C^+/C/CO transition region is seen to shift to higher values of A_V as the radiation penetrates deeper into the cloud and the rise in CO density is more gradual under stronger radiation, as shielding becomes less effective. This leads to a broader emission feature, causing the wider profiles seen in Figure 3.5 as the radiation intensity increases.

3.4.3 Cosmic-ray ionization rate

The cosmic-ray flux is known to vary by over an order of magnitude. Magnetic field lines can channel cosmic-rays away from dense molecular cores; alternatively, the flux of particles in starburst regions can be many times higher than the canonical rate (Schilke et al. 1993). We therefore consider a range of $0.1 \leq \zeta \leq 10^3$ times our adopted canonical rate of 1.3×10^{-17} s^{-1}.

Increasing the flux of ionizing particles through the cloud produces a complex behaviour in the X_{CO} versus A_V profiles (see Figure 3.7). As the ionization rate increases from the standard

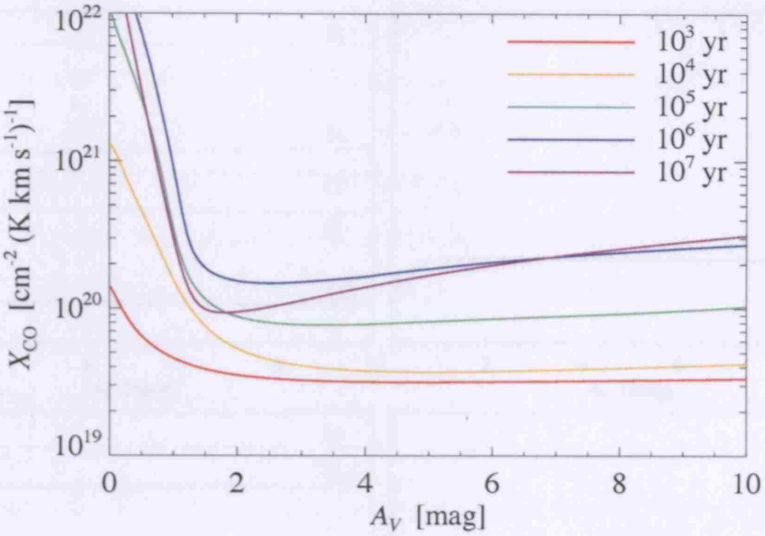

Figure 3.8: X_{CO} versus A_V profiles for varying cloud age (t yr).

value (see Table 3.1), CO is initially destroyed more effectively through reactions with He^+ and its abundance drops, causing an upward shift in the X_{CO} profile. This is the case for the $\zeta = 10$ and $\zeta = 10^2$ models. However, the corresponding increase in the cosmic-ray heating rate causes a rise in gas temperature, becoming the dominant heating mechanism at $A_V > 1$ mag for $\zeta = 10^2$ and at all depths for $\zeta = 10^3$. This promotes CO formation and emission, and counters, in part, the increased destruction rate. A hump emerges in the CO density and emission profiles (not shown) across the region $0 < A_V < 1.5$ mag for ionization rates above 10^2, produced by the strong cosmic-ray heating and effective [O I] cooling that peaks at $A_V \sim 1.5$ mag. This results in X_{CO} profile minima that are lower than in the standard model and nearer the cloud surface. Thus, a slight rise in ionization rate shifts the X_{CO} profile minimum upwards, whilst a further increase in ionization rate leads to the X_{CO} minimum dropping and moving towards the cloud surface. In models with ζ below the standard value (not shown), there is no appreciable change in the X_{CO} profile shape.

3.4.4 Time-dependence

The evolution of a cloud consisting initially of atomic species produces profiles that change from low, very broad minima to the usual, sharper minimum as the chemistry approaches equilibrium (see Figure 3.8). The formation of molecular hydrogen represents the significant time-scale in the chemical evolution, since the formation of CO proceeds fairly rapidly once H_2 is dominant. At early

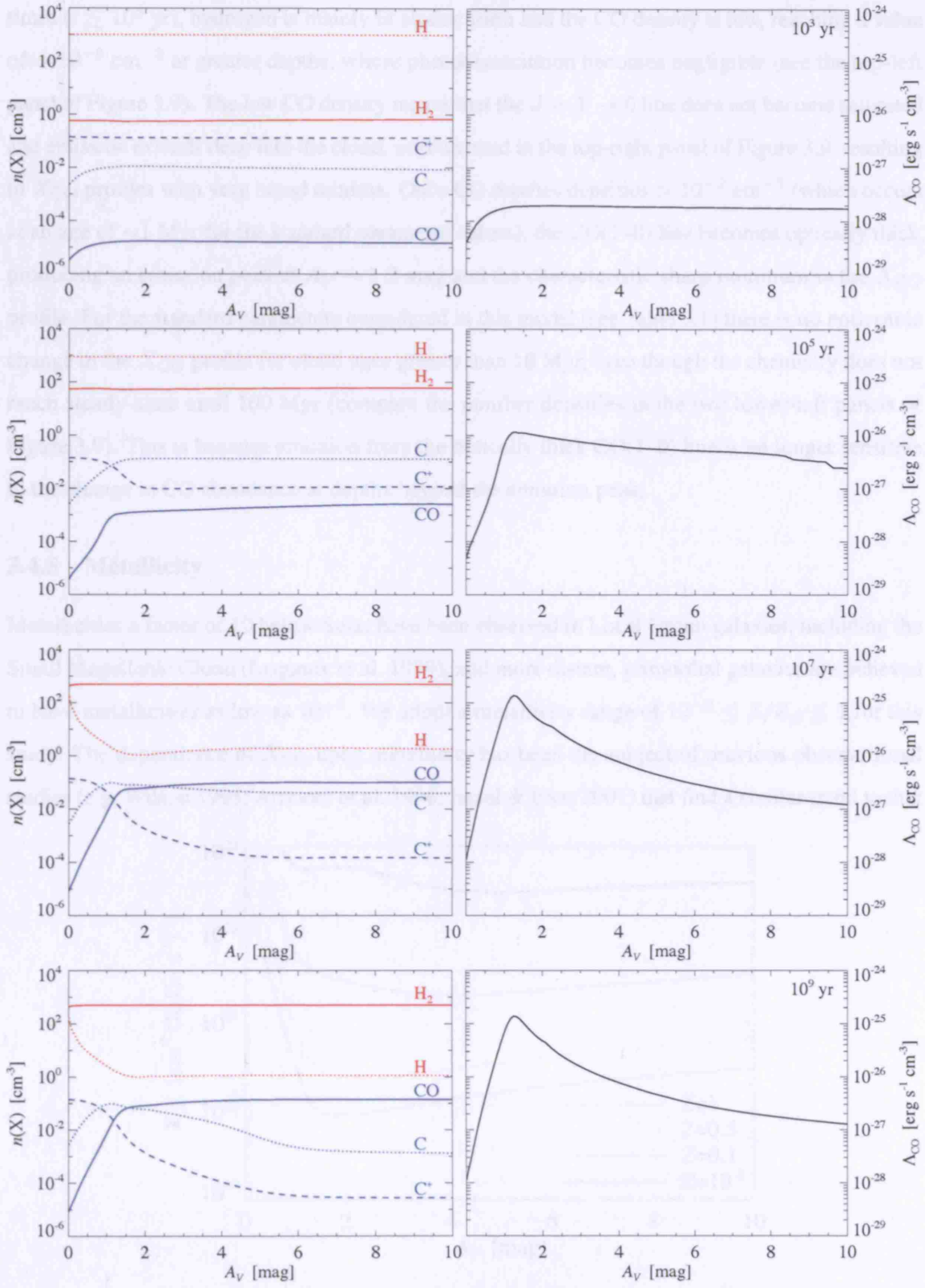

Figure 3.9: *Left*: Number densities of H (red dotted line), H_2 (red solid line), C^+ (blue dashed line), C (blue dotted line) and CO (blue solid line) as a function of A_V for cloud ages of 10^3, 10^5, 10^7 and 10^9 yr (from top to bottom). *Right*: CO(1–0) emissivity as a function of A_V for cloud ages of 10^3, 10^5, 10^7 and 10^9 yr (from top to bottom).

times ($t \lesssim 10^3$ yr), hydrogen is mainly in atomic form and the CO density is low, reaching a value of $\sim 10^{-5}$ cm^{-3} at greater depths, where photodissociation becomes negligible (see the top-left panel of Figure 3.9). The low CO density means that the $J = 1 \rightarrow 0$ line does not become saturated and emission extends deep into the cloud, as illustrated in the top-right panel of Figure 3.9, resulting in $X_{\rm CO}$ profiles with very broad minima. Once CO reaches densities $> 10^{-2}$ cm^{-3} (which occurs at an age of $\sim$1 Myr for the standard parameter values), the CO(1–0) line becomes optically thick, producing an emission peak at $A_V \sim 1.2$ mag and the characteristic sharp minimum in the $X_{\rm CO}$ profile. For the standard parameters considered in this model (see Table 3.1) there is no noticeable change in the $X_{\rm CO}$ profile for cloud ages greater than 10 Myr, even though the chemistry does not reach steady-state until 100 Myr (compare the number densities in the two lower-left panels of Figure 3.9). This is because emission from the optically thick CO(1–0) line is no longer sensitive to the change in CO abundance at depths beyond the emission peak.

3.4.5 Metallicity

Metallicities a factor of 10 below Solar have been observed in Local Group galaxies, including the Small Magellanic Cloud (Lequeux et al. 1979), and more distant, primordial galaxies are believed to have metallicities as low as 10^{-2}. We adopt a metallicity range of $10^{-2} \leq Z/Z_\odot \leq 1$ for this study. The dependence of $X_{\rm CO}$ upon metallicity has been the subject of previous observational studies (e.g. Wilson 1995; Arimoto et al. 1996; Israel & Baas 2001) that find a similar trend to that

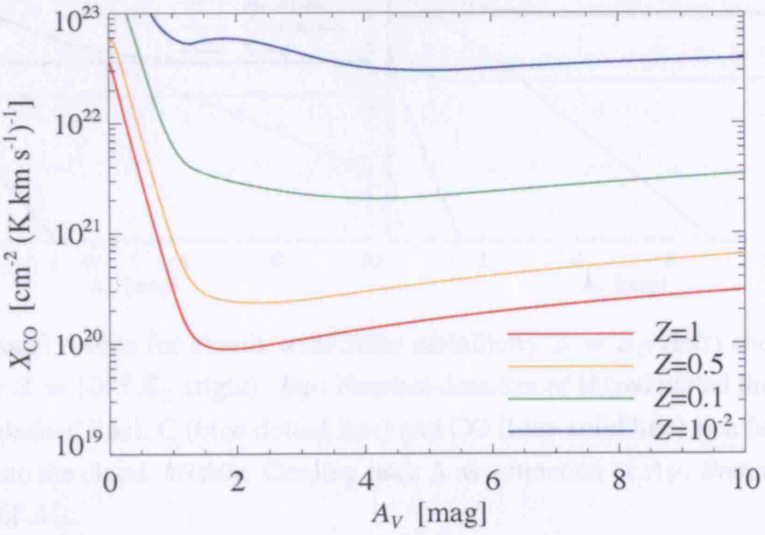

Figure 3.10: $X_{\rm CO}$ versus A_V profiles for varying metallicity ($Z/Z_\odot$).

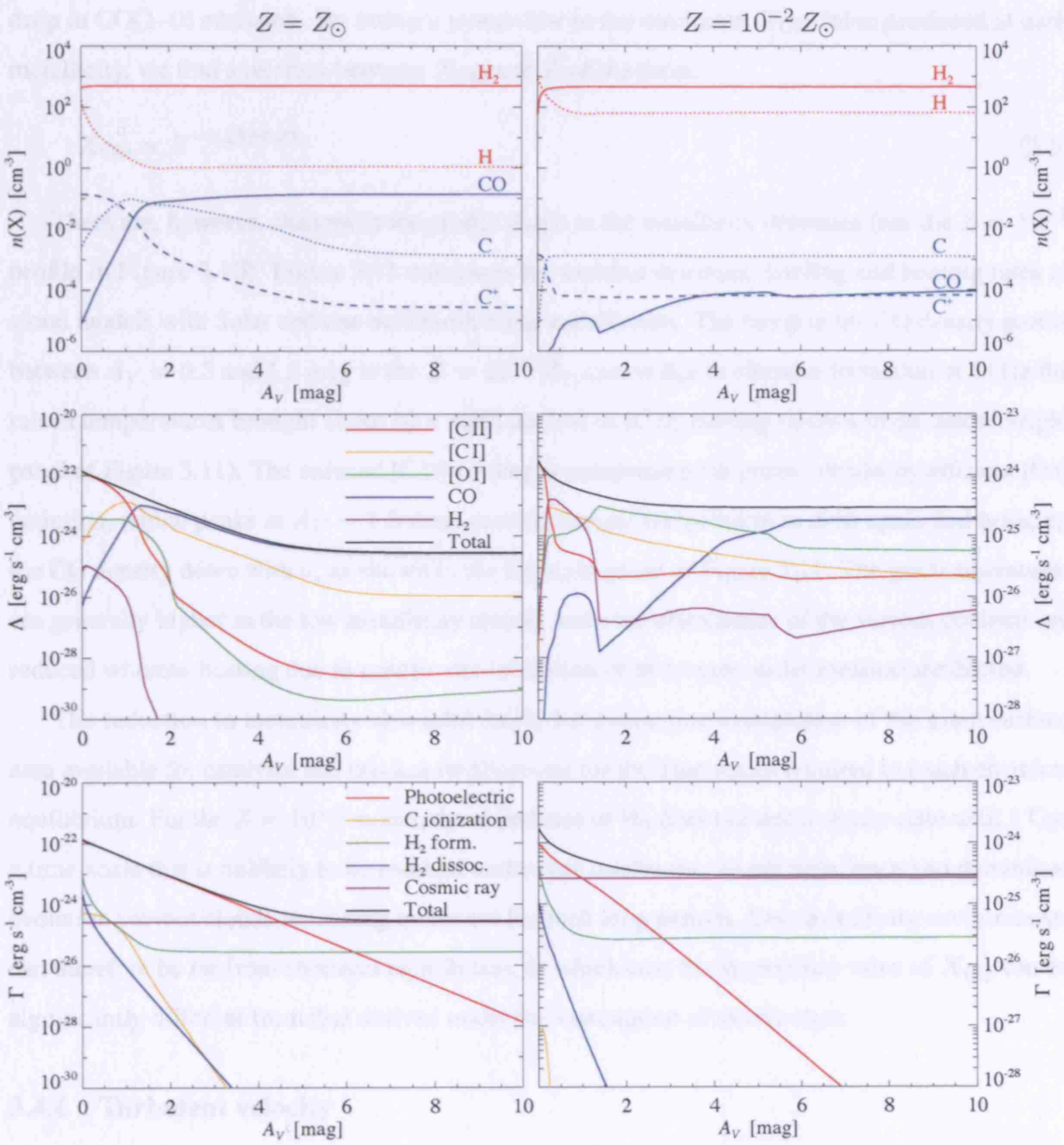

Figure 3.11: Model results for clouds with Solar metallicity $Z = Z_\odot$ (left) and one hundredth Solar metallicity $Z = 10^{-2}\,Z_\odot$ (right). *Top*: Number densities of H (red dotted line), H_2 (red solid line), C^+ (blue dashed line), C (blue dotted line) and CO (blue solid line) as a function of visual extinction A_V into the cloud. *Middle*: Cooling rates Λ as a function of A_V. *Bottom*: Heating rates Γ as a function of A_V.

shown in Figure 3.10, namely, that the value of $X_{\rm CO}$ is generally increased when metallicity is less than Solar. This is due to the reduced abundance of CO that can form, resulting in a matching drop in CO(1–0) emission. By fitting a power-law to the minimum $X_{\rm CO}$ value produced at each metallicity, we find a relation between $X_{\rm CO}$ and Z of the form:

$$X_{\rm CO} \propto Z^{-1.22\pm0.03} \tag{3.5}$$

There are, however, changes in the profile shape as the metallicity decreases (see the $Z = 10^{-2}$ profile in Figure 3.10). Figure 3.11 compares the number densities, cooling and heating rates in cloud models with Solar and one hundredth Solar metallicities. The bump in the CO density profile between $A_V = 0.5$ and 1.5 mag in the $Z = 10^{-2}\,Z_\odot$ case is due to effective formation of CO at the raised temperatures brought about by a rapid decline in [C II] cooling (shown in the middle-right panel of Figure 3.11). The reduced [C II] cooling is compensated at greater depths by efficient [O I] emission, which peaks at $A_V \sim 1.5$ mag, causing the gas temperature to drop again and bringing the CO density down with it, as shown in the top-right panel of Figure 3.11. The gas temperatures are generally higher in the low metallicity clouds, since the abundances of the various coolants are reduced whereas heating due to cosmic-ray ionization of hydrogen nuclei remains unaffected.

The reduction in metallicity also inhibits H_2 formation due to depletion of the grain surface area available for catalysis and this has implications for the time-scales required to reach chemical equilibrium. For the $Z = 10^{-2}$ model, the abundance of H_2 does not reach steady-state until 1 Gyr, a time-scale that is unlikely to be reached under real conditions, where turbulence and dynamical evolution prevent clouds remaining quiescent for such long periods. Low metallicity environments can therefore be far from chemical equilibrium, in which case the appropriate value of $X_{\rm CO}$ can be significantly different from that derived under the assumption of steady-state.

3.4.6 Turbulent velocity

The degree of turbulence within a cloud can be parametrized by its contribution to the observed random velocities. Turbulent velocities can be close to zero in quiescent clouds and 5 km s^{-1} or more in particularly active regions (e.g. Williams et al. 1995; Brunt & Heyer 2002). We consider a turbulent velocity range $0.5 \leq v_{\rm turb} \leq 3$ km s^{-1} in this work.

An increase in the turbulent velocity of the cloud serves to decrease the value of $X_{\rm CO}$ at each depth point whilst retaining the characteristic profile shape (see Figure 3.12). The stronger turbulent broadening of emission lines leads to lower opacities, causing a rise in CO emission (as seen in Figure 3.13) and a corresponding drop in the value of $X_{\rm CO}$.

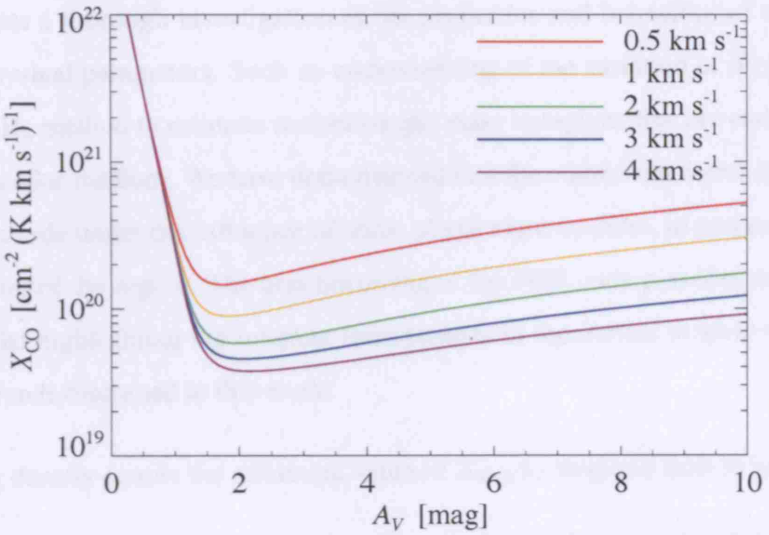

Figure 3.12: $X_{\rm CO}$ versus A_V profiles for varying turbulent velocity within the cloud ($v_{\rm turb}$ km s^{-1}).

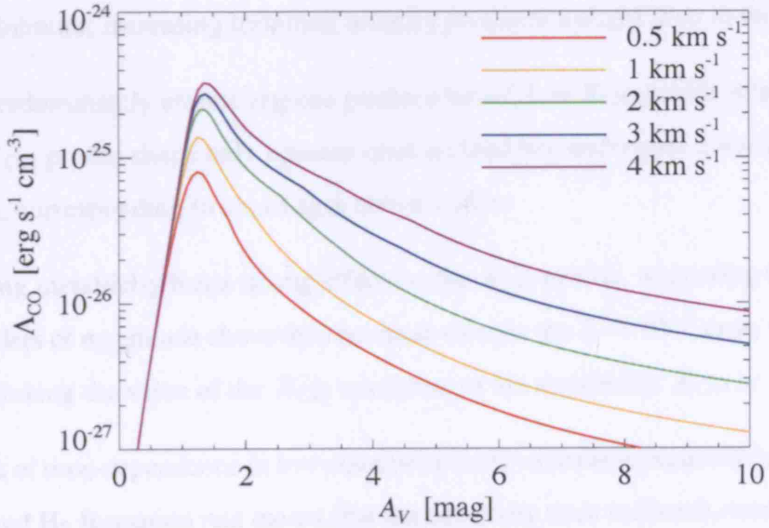

Figure 3.13: CO(1–0) emissivity as a function of A_V for varying turbulent velocity within the cloud ($v_{\rm turb}$ km s^{-1}).

3.5 Conclusions

This work presents a thorough investigation of the properties and behaviour of the $X_{\rm CO}$ factor under varying physical parameters. Such an understanding of the variation in $X_{\rm CO}$ is vital when using the CO-to-H_2 method to estimate molecular gas mass in regions that are markedly different to the local interstellar medium. We have demonstrated that the conversion factor can vary by over an order of magnitude under the influence of some physical parameters, in particular the density, age and metallicity of the region. The benchmarking of the PDR code provides support for these predictions, whilst highlighting the inherent uncertainties in theoretical models of this kind. To summarize the trends discussed in this work:

1. Increasing density causes the minimum value of $X_{\rm CO}$ to drop and shift to lower A_V.

2. Stronger radiation fields slightly raise the $X_{\rm CO}$ profile minimum and push it deeper into the cloud.

3. A slight increase in the cosmic-ray ionization rate will raise the $X_{\rm CO}$ minimum, but ionization rates over 100 times the standard value result in the minimum dropping and appearing nearer to the cloud surface.

4. Turbulent velocity variation does not significantly alter the shape or position of the $X_{\rm CO}$ profile minimum; increasing turbulent velocity produces a slight drop in the $X_{\rm CO}$ value.

5. Young, predominantly atomic regions produce broad, low $X_{\rm CO}$ profile minima; the characteristic $X_{\rm CO}$ profile shape only appears once a cloud has undergone considerable chemical evolution, corresponding to cloud ages above 1 Myr.

6. Decreasing metallicity has a strong effect on the $X_{\rm CO}$ profile, increasing the minimum by over 2 orders of magnitude above the canonical value in the $Z = 10^{-2}$ case, with a power-law relation linking the value of the $X_{\rm CO}$ minimum to the metallicity, $X_{\rm CO} \propto Z^{-1.22\pm0.03}$.

7. The issue of time-dependence in low metallicity environments is particularly important, since the reduced H_2 formation rate means that the chemistry does not reach steady-state for cloud ages below 100 Myr.

Conditions that produce extended CO emission deep into the cloud (such as low density, strong radiation fields or low metallicity) serve to broaden the $X_{\rm CO}$ profile minimum, and the CO emission reliably traces the H_2 column density to higher A_V in such cases. Since interstellar clouds are

likely to be clumpy on scales significantly less than the 10 mag of extinction considered in these models, the CO emission in each clump is likely to be optically thin for most of the parameters considered here. Conditions producing extended emission allow for the presence of larger clump sizes before the reliability of the X_{CO} factor as a tracer of total H_2 column density breaks down.

In the next chapter, we continue this project by deriving a set of X_{CO} values that are appropriate for specific galaxy types, comparing them to observational studies of the X_{CO} factor in those regions. This allows the accuracy of theoretical models of X_{CO} to be evaluated. We will present a table of conversion factors that may be used by observers to obtain more reliable estimates for molecular gas masses, along with limitations for their use.

CHAPTER 4

CONVERSION FACTORS FOR SPECIFIC GALAXY TYPES

4.1 Introduction

We have seen in the last chapter that there is considerable potential for variation in the CO-to-H_2 conversion factor X_{CO}. As discussed, observational studies of external galaxies have inferred values of X_{CO} using a variety of techniques, including virial mass estimates when individual clouds can be resolved (Brouillet et al. 1998), dust continuum observations coupled with some assumptions regarding the gas-to-dust mass ratio (Boselli et al. 2002b) and the use of neutral carbon emission as a tracer when its abundance can be determined (Israel et al. 2006). Such studies confirm the variable nature of X_{CO}, which is seen to differ from galaxy to galaxy. The ability to resolve molecular emission from individual clouds within nearby galaxies through interferometric techniques has created new opportunities for studying the interstellar medium in different environments (e.g. Sakamoto et al. 1999; Helfer et al. 2003); however, many properties still depend critically on the masses derived for these clouds. The CO-to-H_2 conversion factor therefore has an increasingly important role to play in advancing our understanding of the properties of interstellar gas in external galaxies.

In this chapter, we derive values of X_{CO} that are appropriate for the interstellar medium within specific galaxy types. We select a sample of nearby galaxies that are representative of the various commonly observed morphological types and determine the physical properties that best describe the neutral interstellar gas within them by fitting observed line intensity ratios for a range of FIR and submm diagnostic lines. The best fit model for each galaxy is then used to calculate values of X_{CO}

Table 4.1: Properties of the four galaxies adopted for this study.

Galaxy	Morphology[a]	R.A.(2000) (hh mm ss)	Dec.(2000) (° ′ ″)	V_{LSR} (km s^{-1})	Distance (Mpc)	Angular Scale (pc/arcsec)
M 51	SA(s)bc pec	13 29 52.7	+47 11 42.0	464	9.7[b]	46.5
NGC 6946	SAB(rs)cd	20 34 51.2	+60 09 17.5	55	5.5[c]	26.7
M 82	I0; Sbrst	09 55 52.3	+69 40 45.9	175	3.2[d]	15.5
SMC N27	dSB(s)m pec	00 48 21.1	−73 05 29.0	115	63 kpc[e]	0.3

References: [a] de Vaucouleurs et al. (1991); [b] Sandage & Tammann (1975); [c] Tully (1988); [d] Dumke et al. (2001); [e] Rubio et al. (1993).

for various transitions of CO that are appropriate for that galaxy. These values may then be used in future observational studies to obtain more reliable mass estimates. In Section 4.2 we discuss the sample of galaxies we have selected to study and introduce them individually. Section 4.3 describes our fitting procedure to determine appropriate physical parameters for the ISM in each of our sample galaxies. We present the best fit model for each galaxy in Section 4.3.2 and discuss the derived physical parameters and the quality of the fits. In Section 4.4 we use these models to derive suitable CO-to-H_2 conversion factors for each galaxy type considered and we summarize our conclusions in Section 4.5.

4.2 The galaxy sample

To produce CO-to-H_2 conversion factors that are applicable to as wide a variety of galaxies as possible, we select four nearby examples that are considered to be prototypical of the main galaxy types, possessing interstellar clouds that span a range of physical conditions and so are likely to require conversion factors that are somewhat different to the canonical value for the Milky Way, $X_{CO} = 2 \times 10^{20}$ cm^{-2} (K km s^{-1})$^{-1}$ (Strong & Mattox 1996; Dame et al. 2001). The examples we consider are the interacting, grand-design spiral galaxy M 51, the late-type spiral galaxy NGC 6946, which has a nuclear starburst, the irregular starburst galaxy M 82 and nebula N27 within the Small Magellanic Cloud, a dwarf irregular galaxy. Table 4.1 lists the properties of our chosen galaxies; their morphologies (from the RC3 catalogue of de Vaucouleurs et al. 1991), the coordinates of their central positions (J2000 epoch), their radial velocities relative to the local standard of rest (LSR), estimated distances (in Mpc) and the corresponding angular scale at that distance (in pc/arcsec).

We restrict our study to the central positions of these galaxies (with the exception of the Small

Figure 4.1: Colour composite ($B, V, I + H\alpha$) mosaic image of M 51 and its companion NGC 5195 (top-right), obtained with the Advanced Camera for Surveys (ACS) onboard the *Hubble Space Telescope* (*HST*). *Credit: NASA, ESA, Steven Beckwith (STScI) and The Hubble Heritage Team (STScI/AURA).*

Magellanic Cloud, see below). This is partly due to the limited amount of relevant observational data in the required transitions. Most studies of the neutral ISM within external galaxies focus on single-beam observations or mapping of the brightest regions, typically their centres, which are known to exhibit strong molecular concentrations. These studies are further restricted due to the large telescope beam sizes involved (typically >10 arcsec, although interferometric mapping can reach angular resolutions of ∼1 arcsec); these beams can encompass whole ensembles of clouds that exhibit a range of properties. Determination of the physical conditions within these regions is then necessarily limited to deriving average properties for an ensemble of clouds. In this section, the four galaxies in our sample are introduced and observational studies of the interstellar gas within them are summarized.

M 51. The grand-design spiral of M 51 (NGC 5194) appears nearly face-on ($i \sim 20°$) at a distance of 9.7 Mpc (see Table 4.1), and is seen to be interacting with its smaller companion, NGC 5195, which lies 4.5 arcmin to the north (see Figure 4.1). It has a metallicity slightly above Solar, determined near its centre to be $12 + \log(\mathrm{O/H}) = 9.28 \pm 0.11$ (Zaritsky et al. 1994). M 51 has been classed a Seyfert 2 galaxy by Ho et al. (1997), with a central AGN surrounded by a ∼100 pc disc of warm and dense gas (Matsushita et al. 1998). This galaxy has been studied

Figure 4.2: Colour composite image of NGC 6946, showing the central bar and open spiral structure of this low-inclination starburst galaxy. *Credit: Fred Calvert, Adam Block, NOAO/AURA/NSF.*

extensively and a large amount of observational data are available, including an extended map of [C II] 158 μm emission, taken with the *Kuiper Airborne Observatory* (Nikola et al. 2001) and additional observations of FIR fine-structure lines toward the galaxy centre (Negishi et al. 2001) using the Long Wavelength Spectrometer (LWS) onboard the *Infrared Space Observatory* (*ISO*). Ground-based single-dish studies mapping the low-lying transitions of ^{12}CO and ^{13}CO show the CO to be tightly confined to the spiral arms (e.g. García-Burillo et al. 1993; Nakai et al. 1994). Maps of higher CO transitions, $J = 3 \rightarrow 2$ and $4 \rightarrow 3$, have been obtained with the Heinrich Hertz Telescope (HHT) by Nieten et al. (1999) and Dumke et al. (2001), showing warm molecular gas to be present out to a galactocentric radius of 5 kpc or more within these arms. Recently, the [C I] 609 μm fine structure line has also been observed towards the galaxy centre and several positions along the spiral arms (Gerin & Phillips 2000; Israel & Baas 2002; Kramer et al. 2005), which show that the neutral carbon emission is also extended. Aperture synthesis maps were obtained by Sakamoto et al. (1999) and Regan et al. (2001) at resolutions of 4–6 arcsec in the CO(1–0) line and, more recently, Matsushita et al. (2004) have mapped the inner region in CO(3–2).

NGC 6946. This nearby low-inclination ($i \sim 30°$) galaxy, classified as a spiral with a weak bar (SAB) in the RC3 catalogue (de Vaucouleurs et al. 1991), is at a distance of 5.5 Mpc (see Table 4.1) and has an abundance gradient $d\log(\mathrm{O/H})/dR = -0.089 \pm 0.003$ dex kpc^{-1} (Belley & Roy

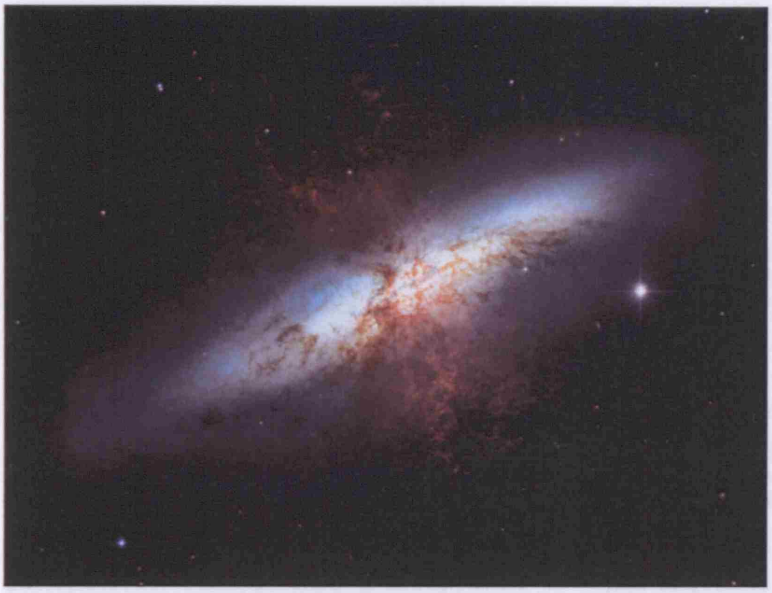

Figure 4.3: Colour composite ($B, V, I + H\alpha$) mosaic image of M 82, obtained with the *HST* ACS. *Credit: NASA, ESA and The Hubble Heritage Team (STScI/AURA).*

1992), similar to that of the Milky Way, and a metallicity of $12 + \log(\mathrm{O/H}) = 9.13 \pm 0.15$ near its centre (Zaritsky et al. 1994). It has a nuclear starburst (see, e.g., Engelbracht et al. 1996) and a small inner bar, seen clearly in recent interferometric maps of CO(1–0) and CO(2–1) (Schinnerer et al. 2006), that is driving an inflow of molecular gas into the central region of intense star formation. The galaxy shows a pronounced open spiral pattern (see Figure 4.2), the north-eastern arm being the brightest at all wavelengths, indicating a site of vigorous ongoing star formation. One of the first galaxies to be mapped in CO emission (Morris & Lo 1978), NGC 6946 has been relatively well studied in the lower CO transitions, both towards its central region (e.g. Weliachew et al. 1988) and towards its spiral arms (Casoli et al. 1990). More recently, maps of the central region have been made in the $J = 2 \rightarrow 1$, $3 \rightarrow 2$ and $4 \rightarrow 3$ transitions of CO and in the [C I] 609 μm line (Mauersberger et al. 1999; Israel & Baas 2001). All these observations show that the gas is predominantly molecular within 5 kpc of the centre and that CO emission is rather extended over the galaxy, but is most concentrated in the central region.

M 82. The irregular starburst galaxy M 82 (NGC 3034) is perhaps the most studied of all nearby galaxies due to its spectacular display of active star formation, which dominates its evolution and is thought to have been triggered about 100 Myr ago by tidal interaction with its companion galaxy M81. Originating in the nucleus, the starburst activity within M 82 is currently seen to be

Figure 4.4: Colour composite image of the Small Magellanic Cloud. *Credit & Copyright: Josch Hambsch, Robert Gendler.*

propagating into the molecular rings, disrupting the surrounding ISM and causing the insterstellar clouds to fragment (see Figure 4.3). The gravitational interaction is also likely to have produced the stellar bar seen in the central ∼400 pc (Telesco et al. 1991). As a result of its vigorous star formation, M 82 is also one of the most luminous nearby galaxies in the infrared, with $L_{\rm IR} \sim 4 \times 10^{10}\ L_{\odot}$. The galaxy has been the subject of many observational studies, including extensive mapping in both low and high (up to $J = 7 \rightarrow 6$) transitions of CO (e.g. Sutton et al. 1983; White et al. 1994; Mao et al. 2000; Seaquist et al. 2006), comprehensive FIR spectroscopy (Colbert et al. 1999) and mapping in a variety of molecular species, including HCO^+ and HCN (Seaquist & Frayer 2000), SiO (García-Burillo et al. 2001) and CO^+ (Fuente et al. 2006). These observations demonstrate the presence of PDR chemistry over large regions of the galaxy centre and strong, extended CO emission arising from a warm and diffuse ISM.

Nebula N27 in the SMC. At just under 63 kpc away, the Small Magellanic Cloud (SMC; NGC 292) is one of the nearest examples of a dwarf irregular galaxy, and presents an excellent opportunity to study the properties of interstellar gas under conditions very different to those in the Milky Way. Its metal content is known to be particularly low, with an oxygen abundance of $12 + \log [{\rm O/H}] = 7.96 \pm 0.11$ (Vermeij & van der Hulst 2002) implying a metallicity of about

one tenth Solar, and it possesses a gas-rich interstellar medium that is subjected to strong FUV fluxes due to the presence of a large population of young massive stars (Westerlund 1990, see Figure 4.4). As part of a three-galaxy system that includes the Large Magellanic Cloud (LMC) and the Milky Way Galaxy, the SMC has experienced a disruptive history; an encounter with the LMC some 200 Myr ago is likely to be responsible for the current burst of star-forming activity (Gardiner & Noguchi 1996). Such rapid star formation in a low metallicity environment is also thought to be representative of the conditions within primordial galaxies. In the absence of an obvious central feature, we have chosen to adopt the well-studied region surrounding the N27 nebula as our example of the typical environment within the SMC. The N27 nebula is a bright and relatively compact H II region located in the south-western bar of the SMC and is associated with the IRAS point source LIRS 49 (Schwering & Israel 1989). It has been mapped in the $J = 1 \rightarrow 0$ and $J = 2 \rightarrow 1$ lines of CO by Rubio et al. (1993) and observed in the $J = 3 \rightarrow 2$ CO line and transitions of CS, HCO^+ and HCN by Heikkilä et al. (1999). More recently, the [C I] 609 μm line has been detected in this region for the first time (Bolatto et al. 2000) and the FIR fine structure lines have been observed using the *ISO* LWS.

4.3 Determining appropriate physical parameters for the sample of galaxies

The atomic fine structure and CO rotational emission lines serve as excellent diagnostics of the physical conditions within PDRs, since they are the dominant cooling lines within the warm gas at the surfaces of molecular clouds. Their range of critical densities $n_{\rm cr}$ and energy level spacings $\Delta E/k$ mean that, when used in combination, the intensities of these lines can be used to constrain the density, incident FUV flux and surface temperature of the gas (see, e.g., Kaufman et al. 1999). The use of key emission line ratios to constrain the physical parameters within PDRs was discussed in Section 1.6 so will not be repeated here.

In order to derive appropriate physical parameters for the galaxies in our sample, we compare emission line intensity ratios predicted by PDR models to those detected in each of the four example galaxies. The best fitting models are determined by performing a χ^2 goodness of fit analysis of the predicted and observed line ratios for a grid of PDR models covering a large region of parameter space. Section 4.3.1 describes the grid of models used for comparison with the galaxies in our sample, the calculation of appropriate line ratios from the observed line intensities and the calculation of χ^2 values, from which the best fit models are determined. The observational

data obtained from the literature and the resulting line ratios adopted for each galaxy are discussed and the corresponding best fit models are presented in Section 4.3.2. These models are then used in Section 4.4 to derive suitable CO-to-H_2 conversion factors X_{CO} for each galaxy type considered.

4.3.1 Best fit PDR models using χ^2 analysis

The short computation times required by the UCL_PDR code make it ideally suited to the calculation of large grids of models covering substantial regions of parameter space. The models predict the integrated intensities of the fine structure and CO rotational lines emitted by a PDR with the adopted physical parameters. Each model produces line intensities as a function of total cloud depth (at visual extinctions of $0 < A_V < 10$ mag) for cloud ages of 10^4, 10^5, 10^6, 10^7 and 10^8 yr. The standard version of the UCL_PDR code was used to calculate the grid of models to which the χ^2 analysis is then applied. The code is described in detail in Chapter 2. As in previous work (see Chapter 3), the gas is initially assumed to be fully atomic in the models, with all carbon in C^+, and the evolving chemistry and thermal balance are then computed for subsequent time-steps. The PDR is treated as a one-dimensional semi-infinite slab of uniform density. We adopt the standard chemical network used in the UCL_PDR code, neglecting freeze-out of atoms and molecules onto grains. The metallicity-dependence of the gas-phase elemental abundances, dust and PAH number densities, photoelectric heating rate and H_2 formation rate on grains are as before (see Section 2.1.8). Table 4.2 lists the range of parameter values covered by the grid of models, including those parameters that are not varied. Homogeneous clouds with hydrogen nuclei number densities of $10^2 \leq n \leq 10^5$ cm^{-3}, subject to incident FUV fluxes of $10 \leq G_0 \leq 10^5$ times the standard Habing (1968) ISRF have been computed at metallicities $Z/Z_\odot$ of 1, 0.5 and 0.1. A turbulent velocity of $v_{turb} = 1.5$ km s^{-1} is adopted in all the models, typical of individual Galactic molecular clouds (e.g. Hollenbach & Tielens 1999). We do not consider the variation of this parameter in our attempts to fit the observed emission from each galaxy, since the line ratios are believed to be fairly insensitive to small changes in the turbulent velocity (Wolfire et al. 1989). Furthermore, few estimates exist for the degree of turbulent motion within molecular clouds of other galaxies, since observations of extragalactic emission lines do not generally resolve the velocities of individual clouds.

Comparing PDR model predictions to extragalactic observations is never straightforward. Individual molecular clouds are rarely resolved in single-dish observations, particularly so in the case of FIR fine structure lines, which have typically been observed with the *ISO* LWS with a beam size of ~70–80 arcsec. Several phases of the ISM are therefore contained within a single

Table 4.2: The region of parameter space covered by the grid of PDR models.

Parameter	Range of values
Cloud density (cm^{-3})	$10^2 \leq n \leq 10^5$
Incident FUV flux (Habing)	$10 \leq G_0 \leq 10^5$
Metallicity	$0.1 \leq Z/Z_\odot \leq 1$
Age of the cloud (yr)	$10^4 \leq t \leq 10^8$
Cloud size (mag)	$0 \leq A_V \leq 10$
C.R. ionization rate (s^{-1})	$\zeta = 5 \times 10^{-17}$
Turbulent velocity ($km\,s^{-1}$)	$v_{turb} = 1.5$

beam and the line intensity ratios will represent the combined emission from these phases. The physical properties derived from comparison with PDR models are then the *average* properties for the molecular clouds within the region, although they may be biased towards those of the brighter components. By using line ratios, rather than fitting the line intensities directly, the beam area filling factors of the two emission lines are cancelled out, assuming that they come from the same clouds.

In our fitting of the observed fine structure and CO rotational lines, we will consider the following line intensity ratios:

1. [O I] 63 μm/[C II]$_{PDR}$
2. [O I] 145 μm/[O I] 63 μm
3. [C II]$_{PDR}$/[C I] 609 μm
4. [C II]$_{PDR}$/CO(3–2)
5. [C I] 609 μm/CO(3–2)
6. CO(3–2)/CO(1–0)

when the necessary line intensities are available in the literature.

In order to derive meaningful ratios, the various line intensities must share a common spatial resolution. Given that the lines are observed with different beam sizes, it is necessary to convolve the integrated intensities to the spatial resolution appropriate to the largest beam size, typically that

of the *ISO* LWS, which has an average half-power beam width (HPBW) of ~75 arcsec. When observational data at the necessary resolution are not available in the literature, we perform the convolution using the scaling factor:

$$\Phi = \sqrt{\frac{\theta_{\mathrm{b},i}^2 + \theta_{\mathrm{s},x}^2}{\theta_{\mathrm{b},f}^2 + \theta_{\mathrm{s},x}^2}} \times \sqrt{\frac{\theta_{\mathrm{b},i}^2 + \theta_{\mathrm{s},y}^2}{\theta_{\mathrm{b},f}^2 + \theta_{\mathrm{s},y}^2}}, \tag{4.1}$$

where $\theta_{\mathrm{b},i}$ and $\theta_{\mathrm{b},f}$ are the initial (observed) and final beam sizes (HPBW in arcsec), and $\theta_{\mathrm{s},x}$ and $\theta_{\mathrm{s},y}$ are the source sizes along the major and minor axes (FWHM in arcsec). Of course, if the source is circular then these two axes will have the same dimensions. The observed intensity is then multiplied by this factor to obtain the intensity at the desired resolution.

Since [C II] 158 μm emission arises from both ionized and neutral gas, the fraction originating from the ionized medium must be subtracted before a comparison with PDR models can be made. We have chosen to estimate the fraction of [C II] emission from the ionized medium using the observed [N II] 122 μm fine structure line, in the manner of Malhotra et al. (2001) and Contursi et al. (2002). The [N II] emission occurs exclusively in the ionized gas, so by assuming a constant ratio between the [C II] and [N II] line intensities in the diffuse ionized medium (DIM), taken to be the dominant ionized component, the contribution of ionized gas to [C II] emission can be estimated. The [C II]/[N II] ratio derived by these authors is 4.3, based upon observations of ionized gas in the Milky Way and using Solar abundances for carbon and nitrogen. In reality, this ratio is likely to vary from region to region and the metallicities of the galaxies studied here are known to differ. However, the abundance ratio has been shown to be independent of metallicity in both normal and irregular galaxies (Garnett et al. 1999) and in view of the lack of more reliable estimates of the ionized gas contribution, the use of this ratio is justified. The intensity of [C II] emission originating from PDRs is then

$$I_{[\mathrm{C\,II}]_{\mathrm{PDR}}} = I_{[\mathrm{C\,II}]} - 4.3 \times I_{[\mathrm{N\,II}]} \qquad [\mathrm{erg\,s^{-1}\,cm^{-2}\,sr^{-1}}], \tag{4.2}$$

where $I_{[\mathrm{C\,II}]}$ and $I_{[\mathrm{N\,II}]}$ are the observed intensities of the [C II] 158 μm and [N II] 122 μm lines.

Finally, the [C I] and CO intensities are usually measured as velocity-integrated antenna temperatures (in $\mathrm{K\,km\,s^{-1}}$). These values must therefore be converted to integrated intensities ($\mathrm{erg\,s^{-1}\,cm^{-2}\,sr^{-1}}$) before they can be compared to the FIR fine structure lines and model predictions. This is achieved using the relation:

$$I = \frac{2k\nu^3}{c^3} \int T_{\mathrm{A}}\, \mathrm{d}v \qquad [\mathrm{erg\,s^{-1}\,cm^{-2}\,sr^{-1}}], \tag{4.3}$$

where ν is the transition frequency (in Hz) and $\int T_{\mathrm{A}}\, \mathrm{d}v$ is the antenna temperature integrated over velocity (in $\mathrm{K\,km\,s^{-1}}$).

Table 4.3: Line ratios derived for each galaxy in the sample.

Source	$\frac{[\mathrm{O\,I}]\,63}{[\mathrm{C\,II}]_{\mathrm{PDR}}}$	$\frac{[\mathrm{O\,I}]\,145}{[\mathrm{O\,I}]\,63}$	$\frac{[\mathrm{C\,II}]_{\mathrm{PDR}}}{[\mathrm{C\,I}]\,609}$	$\frac{[\mathrm{C\,II}]_{\mathrm{PDR}}}{\mathrm{CO}(3-2)}$	$\frac{[\mathrm{C\,I}]\,609}{\mathrm{CO}(3-2)}$	$\frac{\mathrm{CO}(3-2)}{\mathrm{CO}(1-0)}$
M 51	0.730	n/a	39.41	43.91	1.114	14.74
NGC 6946	0.935	0.058	112.2	58.19	0.519	14.11
M 82	1.329	0.092	128.2	605.6	4.726	16.11
SMC N27	0.873	0.026	219.7	512.3†	2.331†	8.694†

† CO(3–2) data were not available at the location of the N27 nebula so these line ratios were instead calculated using the CO(2–1) integrated intensity derived from the observational data of Rubio et al. (1993).

Once the relevant line intensity ratios have been determined for a particular galaxy, we calculate the reduced χ^2 goodness of fit for each model in the grid as

$$\chi^2 = \frac{1}{(N_{\mathrm{obs}} - N_{\mathrm{par}})} \sum_i \left(\frac{R_i^{\mathrm{obs}} - R_i^{\mathrm{mod}}}{\sigma_i} \right)^2 , \tag{4.4}$$

where N_{obs} is the number of *independent* line ratios compared to observations, N_{par} is the number of free parameters in the models and, for each line ratio i considered, R_i^{obs} is the observed value, R_i^{mod} is the model value and σ_i is the estimated error on the observed value. We take the typical observational error to be ~20% of the line intensity, including calibration uncertainties, leading to a combined error of 30% on the line ratios. Note that three of the line ratios are linked and so not independent, $[\mathrm{C\,II}]_{\mathrm{PDR}}/[\mathrm{C\,I}]$ 609 μm, [C I] 609 μm/CO(3–2) and $[\mathrm{C\,II}]_{\mathrm{PDR}}$/CO(3–2), thus reducing the number of independent line ratios N_{obs} by one.

The best fit model for the physical conditions in each galaxy is therefore the model with the minimum reduced χ^2 value. In the next section we list the calculated line ratios for each galaxy in our sample and present contour maps of reduced χ^2 across the grid of models for each galaxy. The physical parameters derived from the best fit models are discussed for each of the galaxies in our sample.

4.3.2 Adopted line ratios and best fit model parameters

The line intensities used to derive the relevant line ratios are taken from the literature, applying the convolution formula in equation (4.1) when necessary in order to obtain a set of integrated intensities at a common resolution for each source. All the FIR data included have been acquired using the *ISO* LWS, with a typical HPBW of 70–80 arcsec (Lloyd 2003), corresponding to spatial

scales of ~1–3.5 kpc at the distances of these nearby galaxies. All other observations at higher spatial resolution have therefore been convolved to a beam size of 75 arcsec ($\Omega_b = 1.1 \times 10^{-7}$ sr).

Table 4.3 lists the adopted line intensity ratios for each galaxy, derived from data in the literature, to which the predicted line ratios from each model are compared. The majority of the FIR fine structure line intensities are taken from Negishi et al. (2001), who present *ISO* LWS observations for a large sample of galaxies. The line fluxes listed in table 2 of their paper have been converted to intensities using the extended source correction factors of Lloyd (2003) and an effective aperture of $\Omega_b = 1.1 \times 10^{-7}$ sr. For M 51, the CO(1–0), CO(3–2) and [C I] 609 μm integrated intensities listed in table 4 of Kramer et al. (2005) have been adopted, since these values are already at an appropriate angular resolution of 80 arcsec, derived by smoothing available map data. The CO and [C I] data for NGC 6946 are taken from Israel & Baas (2001) and Israel & Baas (2002), and have been convolved to the required resolution using an assumed source size of 26″ × 23″ (Nieten et al. 1999). The adopted line intensities for M 82 were drawn from observational data presented by Colbert et al. (1999), Mao et al. (2000) and Israel & Baas (2002) for the FIR, CO and [C I] transitions, respectively. Bolatto et al. (2000) have used line intensities observed in nebula N27 of the Small Magellanic Cloud to estimate the physical conditions within the region by comparison with the PDR models of Kaufman et al. (1999). The *ISO* LWS data presented in their paper are used here, adjusted to our adopted beam size of 75 arcsec, along with their observed value for the [C I] integrated intensity in the region. The CO(1–0) map of Rubio et al. (1993) covers a smaller area within N27, but is thought to encompass most of the CO emission (Bolatto et al. 2000) and is therefore adopted here. Unfortunately, no CO(3–2) data are currently available in the literature for this source. Rubio et al. (1993) have mapped the CO(2–1) line in the region and we therefore use these data to calculate the ratios $[C\,II]_{PDR}$/CO(2–1), [C I] 609 μm/CO(2–1) and CO(2–1)/CO(1–0) in place of the equivalent CO(3–2) line ratios. The CO and [C I] data were convolved to the appropriate angular resolution assuming a source size of 110″ × 110″, determined from the maps of Rubio et al. (1993). The [N II] 122 μm data used to estimate the contribution of the ionized medium to the [C II] 158 μm emission are taken from Kramer et al. (2005), Negishi et al. (2001) and Colbert et al. (1999) for the relevant regions in M 51, NGC 6946 and M 82, respectively. No [N II] data is available in the literature for the region of interest within the SMC.

Figures 4.5–4.8 show contours of reduced χ^2, calculated for each grid model across the adopted range of densities and FUV fluxes, for each galaxy in our sample. Models with Solar metallicity were used to fit the observed line ratios of M 51, NGC 6946 and M 82, which display similar metallicities. When determining the best fit models for the SMC region, the analysis was restricted

Table 4.4: Best fit physical parameters for each of the four galaxies, based on the model with the lowest χ^2 value.

Source	n (cm^{-3})	G_0 (Habing)	$Z/Z_\odot$	A_V (mag)	t (yr)	$\chi^2_{\rm min}$
M 51	7×10^3	20	1	9.5	10^7	1.7
NGC 6946	1×10^4	20	1	8.6	10^7	7.4
M 82	1×10^3	500	1	5.3	10^8	2.9
SMC N27	1×10^3	100	0.1	2.8	10^5	4.9

to only those models with $Z/Z_\odot = 0.1$, appropriate for this low metallicity environment. The physical parameters of the best fit models for each galaxy are listed in Table 4.4.

M 51. For the central region of M 51, in which our adopted beam size encompasses an area approximately 3.5 kpc across, we find that the observed line intensity ratios are best fit by average conditions characterised by reasonably dense ($n = 7 \times 10^3$ cm^{-3}) gas immersed in a ambient FUV field ($G_0 = 20$ Habing). These values agree remarkably well with those determined by Kramer et al. (2005), who perform a similar χ^2 fit to the observed line ratios using the PDR models presented by Kaufman et al. (1999). They find that local densities of $n \sim 10^4$ cm^{-3} and FUV fluxes of $G_0 \sim 20$ Habing best fit the observations, both at the central position and within the spiral arms of the galaxy. This level of agreement is encouraging, suggesting that the method is reliable and that our models are consistent with those of others. However, our approach has the additional benefit of determining the average cloud size and estimated degree of chemical evolution within the region, since the models produce line intensities that are both depth- and time-dependent. We find that the line ratios are best fit by cloud models with visual extinctions of $A_V \sim 10$ mag and ages of $\sim$10 Myr (when evolving from initially atomic gas). Such conditions are expected in dense regions where many clouds along the line of sight give rise to optically thick emission (with the possible exception of the [C I] and [C II] lines) and the gas is maintained in molecular form. The fact that Kramer et al. (2005) find similar conditions in the spiral arms of M 51 suggest that our models might be equally applicable to these regions. We find a minimum reduced χ^2 of 1.7 for the best fit model, a factor of 2 better than the fit achieved by Kramer et al. (2005). We therefore regard this model as representative of the conditions within interstellar molecular gas in normal spiral galaxies.

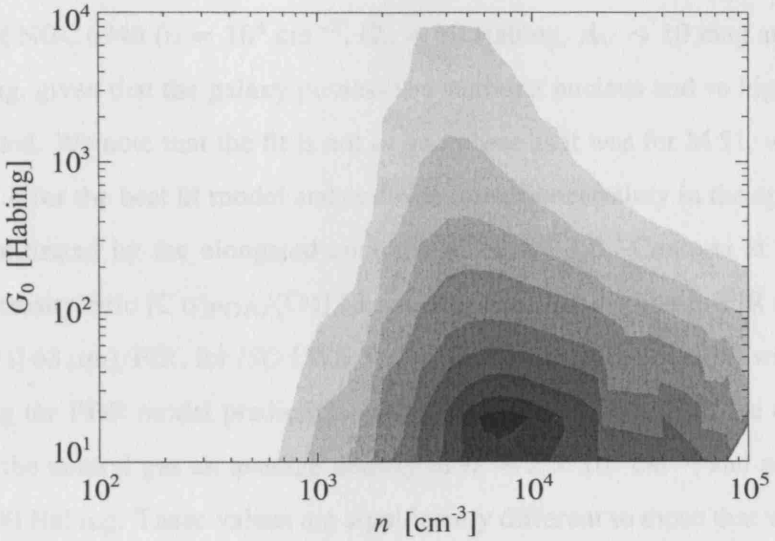

Figure 4.5: Centre of M 51. Contours of the reduced χ^2 fit to the data are shown across the range of parameter space covered by the grid of models in the n–G_0 plane. Contour levels are 1 (black), 2, 3, 5, 10, 20, 50, 100, 200, and 500 (white).

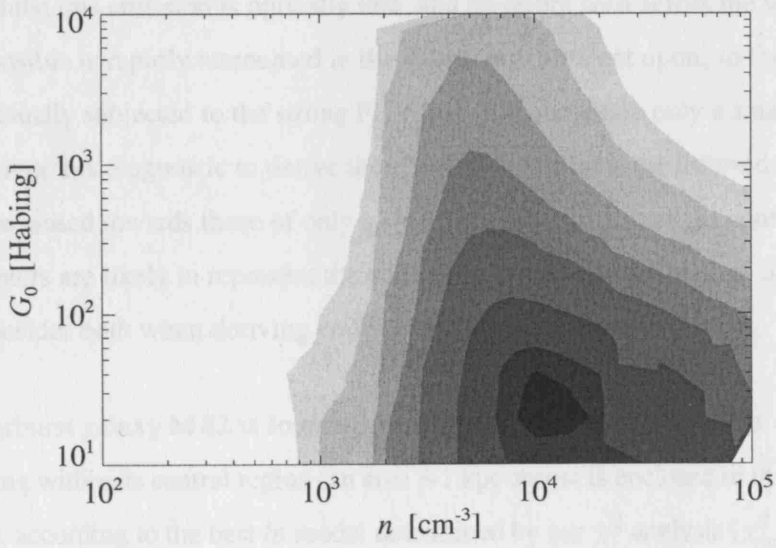

Figure 4.6: Centre of NGC 6946. Contours of the reduced χ^2 fit to the data are shown across the range of parameter space covered by the grid of models in the n–G_0 plane. Contour levels are 7 (black), 8, 10, 20, 50, 100, 200, 500, and 1000 (white).

NGC 6946. Similar physical parameters are found to best fit the line ratios determined for the central region of NGC 6946 ($n = 10^4$ cm^{-3}, $G_0 = 20$ Habing, $A_V \sim 10$ mag and $t \sim 10$ Myr). This is surprising, given that the galaxy possesses a starburst nucleus and so higher FUV fluxes would be expected. We note that the fit is not as good here as it was for M 51, with a minimum reduced χ^2 of 7.4 for the best fit model and some degree of uncertainty in the appropriate value of G_0, as demonstrated by the elongated contours in Figure 4.6. Contursi et al. (2002) have fitted the line intensity ratio [C II]$_{\rm PDR}$/[O I] 63 μm, together with the line-to-FIR continuum ratio, ([C II]$_{\rm PDR}$ + [O I] 63 μm)/FIR, for *ISO* LWS observations of various positions within NGC 6946, again employing the PDR model predictions of Kaufman et al. (1999). At the central position, they derive for the neutral gas an average density of $n \approx 2 \times 10^3$ cm^{-3} and an incident FUV flux of $G_0 \approx 900$ Habing. These values are significantly different to those that we have derived, predicting the gas to be lower in density by almost an order of magnitude and, more dramatically, the incident FUV radiation to be close to a factor of 50 higher. Such a large difference suggests that, by comparing different line ratios, we may be probing different gas components within the region.

The large beam size, corresponding to an area ~2 kpc across at the distance of NGC 6946, makes it likely that the emission arises from a mixture of active and less active regions. The FIR continuum traces the strength of the FUV flux, which is absorbed by the dust and re-emitted in the IR. However, whilst this emission is optically thin, and therefore seen across the whole region, the FUV flux responsible is rapidly attenuated in the clouds it is incident upon, so the surface area of the gas that is actually subjected to the strong FUV flux may constitute only a small fraction of the total area. By using this diagnostic to derive the physical conditions, the inferred cloud properties may therefore be biased towards those of only a small fraction of the total gas content. Both sets of physical parameters are likely to represent the conditions within certain regions of the galaxy, and we therefore consider both when deriving conversion factors in the next section.

M 82. The starburst galaxy M 82 is found to have average gas properties of $n = 10^3$ cm^{-3} and $G_0 = 500$ Habing within its central region (an area ~1 kpc across is enclosed in the 75 arcsec beam at this distance), according to the best fit model determined by our χ^2 analysis ($\chi^2_{\rm min} = 2.9$). These properties are consistent with those derived by Colbert et al. (1999), who find $n \approx 2000$ cm^{-3} and $G_0 \approx 600$ Habing using a combination of H II and PDR models to self-consistently fit the observed FIR ionic and atomic fine structure lines. We find that the observed line ratios are best fit by smaller clouds, with total visual extinctions of $A_V \approx 5$ mag. This is in agreement with the recent observational study of Fuente et al. (2005), who find that the observed abundance ratio

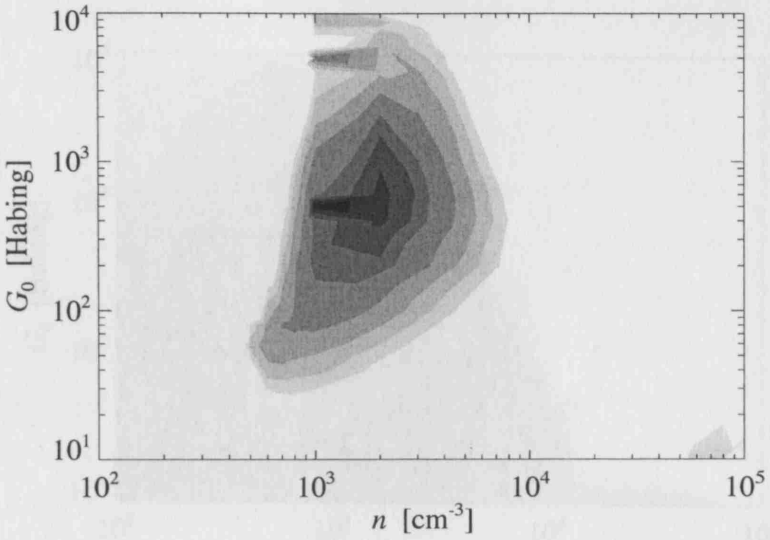

Figure 4.7: Centre of M 82. Contours of the reduced χ^2 fit to the data are shown across the range of parameter space covered by the grid of models in the n–G_0 plane. Contour levels are 2 (black), 4, 6, 10, 15, 20, 25, 30 and 35 (white).

[CN]/[HCN] $\gtrsim 5$, determined for the central 650 pc of M 82, requires cloud sizes of $A_V < 5$–6 mag. For comparison, we plot the [CN]/[HCN] abundance ratio produced by our best fit model as a function of visual extinction in Figure 4.9. From this plot, it can be seen that a cloud size of $A_V < 4$ mag is also required to maintain an abundance ratio > 5 in this model. Finally, Suchkov et al. (1993) proposed an increased cosmic-ray ionization rate of $\zeta = 4 \times 10^{-15}$ s^{-1} in the centre of M 82 to account for the observed physical conditions of the molecular gas. To see if a better fit to the observed line ratios might be obtained by using a higher cosmic-ray ionization rate, we computed additional models with the same density and incident FUV flux as the best fit model, but with cosmic-ray ionization rates of $\zeta = 5 \times 10^{-16}$ and 5×10^{-15} s^{-1} (i.e. 10 and 100 times the original rate). The resulting reduced χ^2 values for these models are 8.7 and 5.5 for the $\zeta = 5 \times 10^{-16}$ and 5×10^{-15} s^{-1} cases, respectively. Both are higher than the original best fit model value of $\chi^2_{\rm min} = 2.9$, although the model with a rate 100 times higher shows a better fit than the model with only a factor 10 increase in the cosmic-ray ionization rate. Since no improvement in the goodness of fit is obtained by using an higher value of ζ, we adopt the physical parameters of the original best fit model when determining appropriate conversion factors for starburst regions.

SMC. In the low metallicity environment of the Small Magellanic Cloud, the molecular gas is known to exhibit significantly different properties to those typically found in regions with

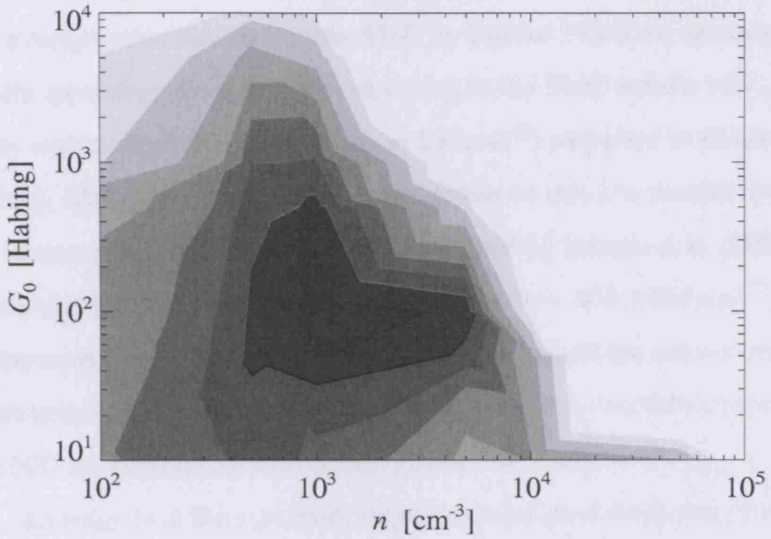

Figure 4.8: N27 region of the Small Magellanic Cloud. Contours of the reduced χ^2 fit to the data are shown across the range of parameter space covered by the grid of models in the n–G_0 plane. Contour levels are 4 (black), 6, 8, 10, 12, 15, 20, 25 and 30 (white).

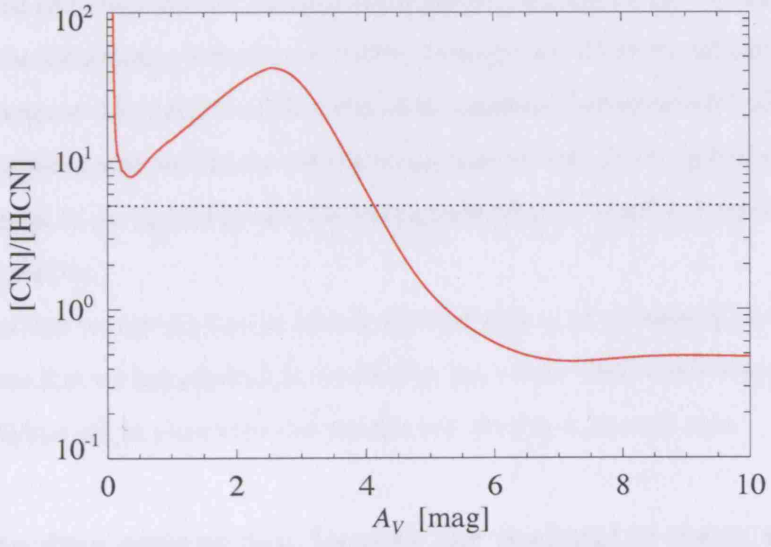

Figure 4.9: Centre of M 82. The abundance ratio of CN to HCN ([CN]/[HCN]; red line) as a function of visual extinction A_V for the best fit model ($n = 10^3$ cm^{-3}, $G_0 = 500$ Habing), compared to the ratio observed by Fuente et al. (2005, black dotted line).

metallicities closer to Solar. By restricting our parameter search to models with metallicity $Z/Z_{\odot} = 0.1$ (the average value derived for the SMC by Dufour 1984) we obtain a best fit model able to successfully reproduce the line ratios observed in the SMC nebula N27, predicting the presence of clouds with reasonably dense gas ($n = 10^3$ cm^{-3}) subjected to elevated FUV fluxes ($G_0 = 100$ Habing), likely due to the reduced extinction in this low metallicity environment. These results are in very good agreement with those obtained by Bolatto et al. (2000), determined using FIR fine structure line and continuum emission to be $n \sim 300$–1000 cm^{-3} and $G_0 \sim 30$–100 Habing. Furthermore, whilst previous models have had to impose the limit of low A_V observed in these clouds, this property is independently predicted as a result by our fitting procedure. The line ratios observed in N27 are slightly less well fit than those of M 51 and M 82 ($\chi^2_{\rm min} = 4.9$ for the best fit model of N27). An analysis of the agreement between model predictions and observations shows that the predicted [O I] 63 μm/[C II] ratio is the most discrepant of the six line ratios considered, being a factor of 2 lower than the observed value. We note that in our adopted line ratios for N27 we have not accounted for the ionized gas contribution to the [C II] 158 μm emission, since the required [N II] 122 μm data are unavailable in the literature. However, subtracting the ionized gas contribution would increase the observed value of the [O I] 63 μm/[C II] ratio, which would actually *reduce* the quality of the fit. Instead, a more favourable explanation for the disagreement between predicted and observed line ratios is the high O/C abundance ratio in the SMC, a factor 2.5 greater than the local value (Wilson et al. 2005). This was not taken into account in the models, but is likely to increase the strength of [O I] emission, producing a higher [O I] 63 μm/[C II] line ratio and bringing the model predictions into better agreement with the observations. We adopt the physical parameters of the best fit model for our consideration of suitable conversion factors for dwarf irregular galaxies.

In the next section we use the best fit models for each galaxy in our sample to derive CO-to-H_2 conversion factors that are appropriate for molecular gas within these environments and suggest transitions of CO that might yield the most reliable mass estimate in each case.

4.4 Appropriate conversion factors for molecular mass estimates in different galaxy types

Having determined the physical conditions that best represent the average properties of the neutral ISM within each galaxy type, we now derive CO-to-H_2 conversion factors appropriate for those conditions in the manner described in Sections 3.2 and 3.4. In addition to the standard value of

$X_{\rm CO}$, relevant to CO $J = 1 \rightarrow 0$ emission, we extend our study to consider conversion factors for higher rotational lines of CO that might serve as useful alternatives under certain conditions. The UCL_PDR code calculates the integrated intensities of all CO rotational lines up to $J = 11 \rightarrow 10$ and values of $X_{\rm CO}$ can therefore be derived for each transition using a more general version of equation (3.1),

$$X_{\rm CO}^{u \rightarrow l} = \frac{N({\rm H_2})}{\int T_{\rm A}({\rm CO}\ J = u \rightarrow l)\, {\rm d}v} \qquad [{\rm cm^{-2}\,(K\,km\,s^{-1})^{-1}}], \tag{4.5}$$

where $N({\rm H_2})$ is the column density of H_2, as before, and $T_{\rm A}({\rm CO}\ J = u \rightarrow l)$ is the antenna temperature of the CO $J = u \rightarrow l$ line. We will use the notation $X_{\rm CO}^{u \rightarrow l}$ to distinguish between the different CO-to-H_2 conversion factors throughout this section. Figures 4.10–4.14 show $X_{\rm CO}$ as a function of visual extinction A_V for various transitions of CO, from the best fit model for each galaxy in our sample. Recall that, for these $X_{\rm CO}$ profiles, the observationally-relevant conversion factor in each transition corresponds to the profile minimum, which represents the peak emission from the cloud (or ensemble of clouds; see Section 3.4). Table 4.5 lists the minimum values of $X_{\rm CO}$ [in units of 10^{20} ${\rm cm^{-2}\,(K\,km\,s^{-1})^{-1}}$] for each galaxy type in various transitions of CO (1–0, 2–1, 3–2, 4–3 and 6–5), together with the cloud depths at which they occur (in A_V). These are therefore the appropriate values of $X_{\rm CO}$ that should be used to derive molecular mass estimates in these regions. The results for each of the four galaxy types are discussed briefly below. For the remainder of this section, the units of the CO-to-H_2 conversion factor, ${\rm cm^{-2}\,(K\,km\,s^{-1})^{-1}}$, are omitted to save space.

We adopted the conditions within the central ~3 kpc of M 51 as characteristic of those within normal late-type spiral galaxies, both in their centres and in their spiral arms. Using the best fit model for these conditions, we find a value for the CO(1–0) conversion factor, $X_{\rm CO}^{1 \rightarrow 0} = 6 \times 10^{19}$. This value is over 3 times *lower* than the canonical CO-to-H_2 conversion factor derived for the Solar neighbourhood, $X_{\rm CO}^{1 \rightarrow 0} = 2 \times 10^{20}$ (Dame et al. 2001). Observational studies of the centres of nearby spiral galaxies have consistently inferred values of $X_{\rm CO}^{1 \rightarrow 0}$ that are lower than the canonical value (see, e.g., Maloney & Black 1988; Sorai et al. 2000; Israel & Baas 2003, and references therein), in agreement with our theoretical value. Furthermore, Israel et al. (2006) have recently determined the CO-to-H_2 conversion factor for the centre of M 51 to be $X_{\rm CO} = 5.0 \pm 2.5 \times 10^{19}$ from observations of neutral carbon emission within the region. This is very close to the value obtained from our best fit model and we feel that this independent observational verification shows our theoretical approach to be reliable. Looking to the higher transition lines of CO, the CO(2–1), CO(3–2) and CO(4–3) lines all give similar conversion factors (4×10^{19}, 5×10^{19} and

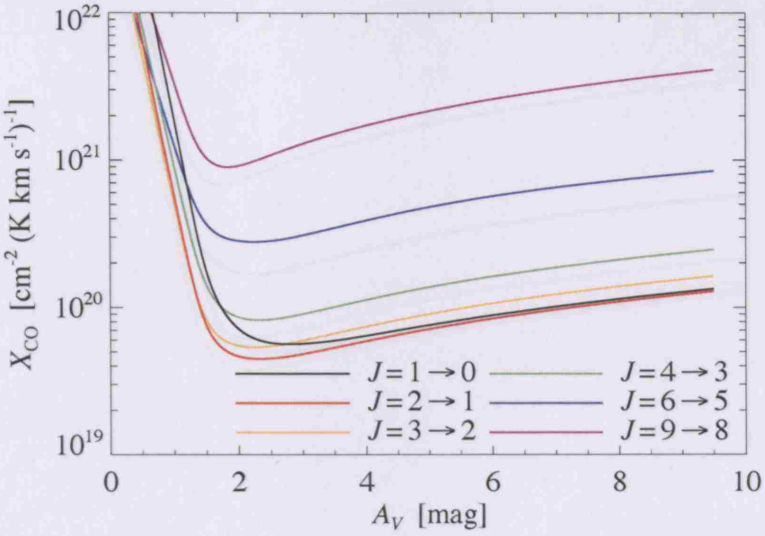

Figure 4.10: Normal spiral galaxies. X_{CO} versus A_V profiles for the best fit physical parameters for the centre of M 51. The values of X_{CO} shown are for emission from the various rotational transitions of CO.

8×10^{19}, respectively) and become optically thick ($\tau > 1$) beyond $A_V \approx 2$ mag. The CO(6–5) and CO(9–8) lines remain optically thin to greater cloud depths, but are fairly weak due to the low gas temperatures (∼140–20 K from the surface to the cloud interior). The lower transitions are therefore more likely to yield reliable molecular mass estimates, particularly when several lines intensities are used in combination.

Our best fit physical parameters for the centre of NGC 6946 are similar to those obtained for M 51, representative of more quiescent interstellar gas, although a slightly higher density is predicted (10^4 cm^{-3} instead of 7×10^3 cm^{-3}). As such, the derived CO-to-H_2 conversion factors are also similar, though they are typically 10–20% lower than those found for M 51 (see Figure 4.11 and Table 4.5). As discussed in the previous section, these conditions may be selectively sampling a particular component within the galaxy centre and may not be fully representative of typical nuclear starburst activity. We therefore also consider an alternative model for the starburst nucleus of NGC 6946, based on the parameters determined by Contursi et al. (2002), i.e. $n = 2 \times 10^3$ cm^{-3} and $G_0 = 10^3$ Habing. The resulting X_{CO} profiles for the various CO transitions are shown in Figure 4.12 and the appropriate conversion factors to be used with each transition to derive molecular masses are listed in Table 4.5. The increased FUV radiation striking the interstellar gas in the Contursi et al. (2002) model leads to enhanced photodissociation of CO, pushing the C^+/C/CO transition deeper into the cloud, where the lower gas temperatures (∼40 K) result in reduced

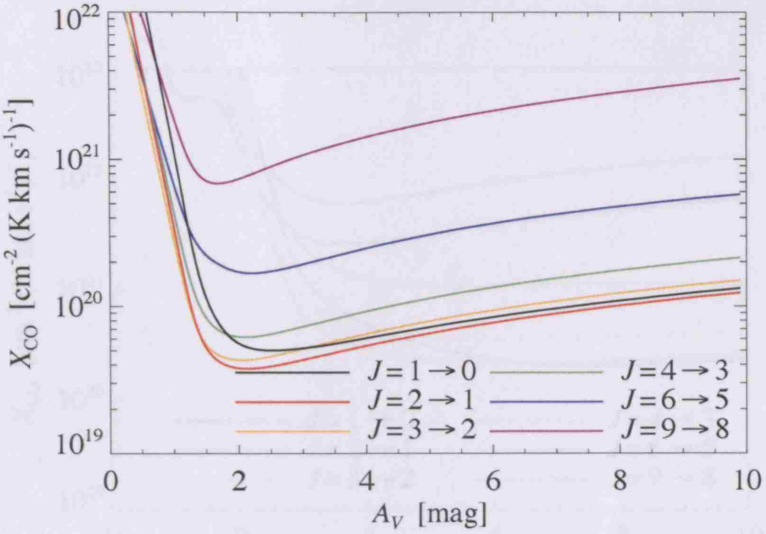

Figure 4.11: Weak starbust nuclei. X_{CO} versus A_V profiles for the best fit physical parameters for the centre of NGC 6946. Values of X_{CO} for the various rotational transitions of CO are shown.

emission strengths. The CO(1–0) conversion factor is $X_{CO}^{1\rightarrow0} = 2 \times 10^{20}$, the value obtained for local regions within the Milky Way. From examining Figure 4.12, it can be seen that the CO(4–3) line may prove to be the best tracer of total molecular mass in this environment, since the $X_{CO}^{4\rightarrow3}$ conversion factor remains fairly constant to high visual extinction. The appropriate value for the conversion factor in this case is $X_{CO}^{4\rightarrow3} = 9.5 \times 10^{20}$.

Smith et al. (1991) have derived the CO-to-H_2 conversion factor for the central regions of M 82 from observations of the dust continuum. They find a value of $\approx 1.2 \times 10^{20}$, which is in good agreement with the value obtained from our best fit model, $X_{CO}^{1\rightarrow0} = 1.5 \times 10^{20}$. The profile minimum occurs deep within the cloud at $A_V \approx 6$ mag, as in the previous case, due to the higher FUV flux (500 Habing). The conversion factors for rotational lines up to CO(4–3) all show fairly constant values for visual extinctions above $\sim$5 mag, suggesting that accurate molecular masses may be obtained for larger cloud sizes. However, the best fit model predicts cloud sizes of $A_V \lesssim 5$ mag, in accordance with observations, so the appropriate CO-to-H_2 conversion factors for clouds of low A_V are likely to vary quite significantly, shown by the sharp rise in X_{CO} towards the left hand side of Figure 4.13. The difficulties of using the CO-to-H_2 conversion factor in such translucent clouds has been discussed extensively (see, e.g., Magnani et al. 2003, and references therein).

The best fit model for the N27 nebula within the Small Magellanic Cloud can provide conversion factors suitable for low metallicity dwarf irregular galaxies. It predicts a CO(1–0) conversion factor

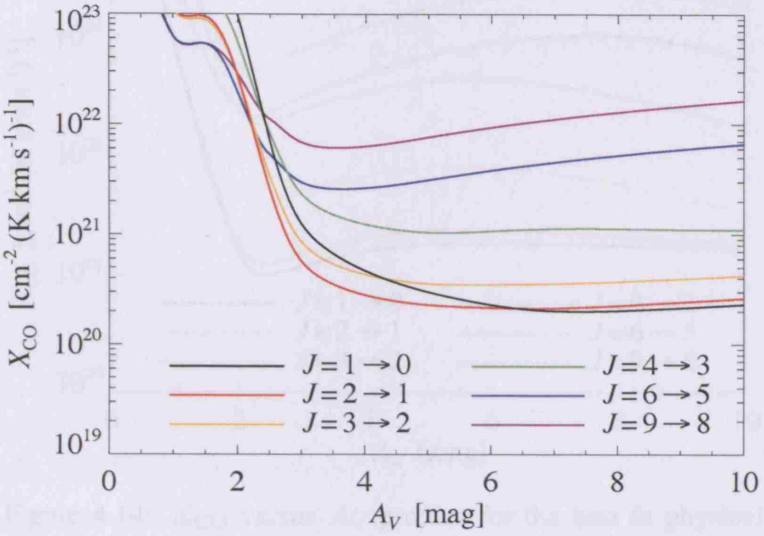

Figure 4.12: Starburst nuclei. X_{CO} versus A_V profiles for the physical parameters derived by Contursi et al. (2002) for the centre of NGC 6946. Values of X_{CO} for the various rotational transitions of CO are shown.

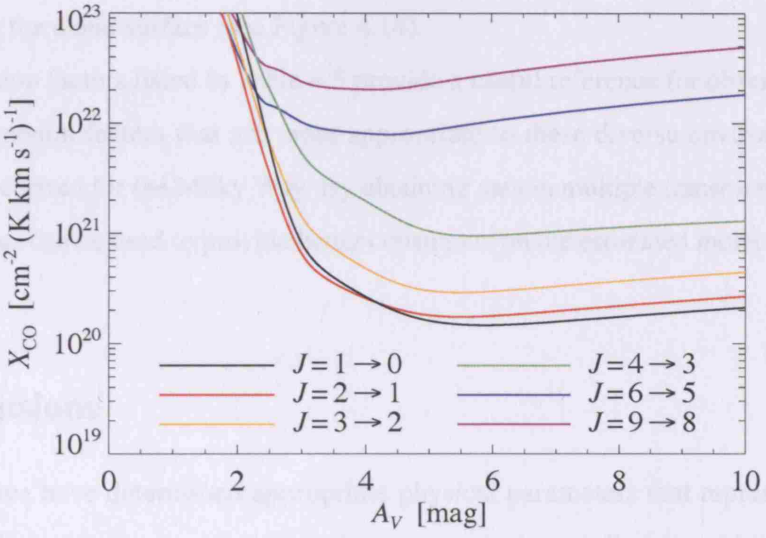

Figure 4.13: Irregular starburst galaxies. X_{CO} versus A_V profiles for the best fit physical parameters for the centre of M 82. Values of X_{CO} for the various rotational transitions of CO are shown.

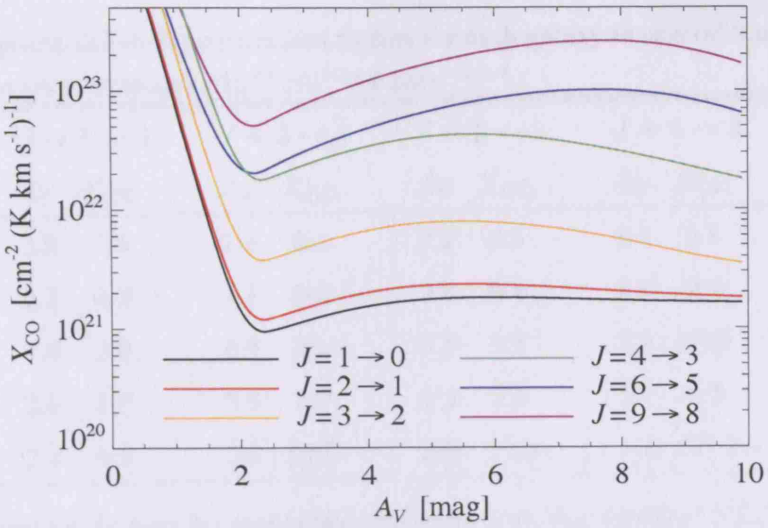

Figure 4.14: X_{CO} versus A_V profiles for the best fit physical parameters for the N27 region of the Small Magellanic Cloud. Values of X_{CO} for the various rotational transitions of CO are shown.

of $X_{CO}^{1\rightarrow0} = 9.5 \times 10^{20}$, approximately 5 times *greater* than the canonical value for the Milky Way. This is primarily due to the low metallicity ($Z = 0.1\ Z_{\odot}$), as discussed in Section 3.4.5. The low visual extinction in these clouds may mean that the appropriate value is higher still, since X_{CO} increases nearer the cloud surface (see Figure 4.14).

The conversion factors listed in Table 4.5 provide a useful reference for observers, presenting "standard" conversion factors that are more appropriate to these diverse environments than the canonical value derived for the Milky Way. By obtaining data in multiple transitions of CO, several conversion factors can be used to provide better constraints on the estimated molecular mass within a region.

4.5 Conclusions

In this chapter we have determined appropriate physical parameters that represent the average conditions within four key extragalactic environments; the interstellar gas within the spiral arms and nuclei of normal late-type spiral galaxies (modelled on the central region of M 51), the starburst nuclei of spiral galaxies and more extreme starburst environments (including the centre of the barred spiral galaxy NGC 6946 and the prototypical starburst galaxy M 82) and the low metallicities and high UV fields typical of dwarf irregular galaxies (in this case, modelled on region N27 of the

Table 4.5: Appropriate CO-to-H_2 conversion factors for each galaxy in several transitions of CO. Values of X_{CO} are given in units of 10^{20} cm^{-2} (K km s^{-1})$^{-1}$.

Galaxy	$J = 1 \rightarrow 0$		$J = 2 \rightarrow 1$		$J = 3 \rightarrow 2$		$J = 4 \rightarrow 3$		$J = 6 \rightarrow 5$	
	A_V	X_{CO}	A_V	X_{CO}	A_V	X_{CO}	A_V	X_{CO}	A_V	X_{CO}
M 51	2.8	0.6	2.3	0.4	2.2	0.5	2.3	0.8	2.2	2.8
NGC 6946*a*	2.5	0.5	2.1	0.4	2.0	0.4	2.1	0.6	2.2	1.7
NGC 6946*b*	7.4	2.0	6.7	2.1	5.5	3.5	5.2	10.4	3.6	25.9
M 82	5.8	1.5	5.5	1.7	5.5	2.9	5.7	9.5	4.4	79.4
SMC N27	2.4	9.5	2.3	12.0	9.9	35.2	2.3	179.3	2.2	203.9

Notes: [a] Determined for the best fit model obtained in this work (see Section 4.3.2). [b] Model values calculated for the physical parameters of Contursi et al. (2002).

Small Magellanic Cloud). Best fit models for these environments have been determined by fitting observed line intensity ratios in the selected regions for a range of FIR and submm diagnostic lines.

The resulting models have been used to derive appropriate CO-to-H_2 conversion factors that will allow reliable molecular mass estimates to be inferred from observations of CO rotational line intensities in a wide variety of extragalactic environments. These conversion factors are listed in Table 4.5. Conversion factors are presented for a range of CO transitions, enabling estimates of the molecular mass to be further constrained using several line intensities simultaneously. Furthermore, different rotational line intensities may probe specific components within the interstellar medium, i.e. dense and hot gas in the case of the high J transitions.

In future work, the range of physical parameters over which each specified conversion factor remains valid will be examined, providing limits on their applicability. The emission lines of other species might also prove to be better tracers of the molecular gas under certain conditions; this prospect will also be considered in a future study. It is hoped that, taken together, these conversion factors will provide a firm basis upon which increasingly reliable molecular mass estimates can be made.

CHAPTER 5

MOLECULAR DARK MATTER IN GALAXIES

The work presented in this chapter is based on the paper by Bell et al. (2006b).

5.1 Introduction

The mapping of external galaxies in the 21 cm H I (e.g. Noordermeer et al. 2005; Walter et al. 2005) and the 2.6 mm CO $J = 1 \rightarrow 0$ (e.g. Helfer et al. 2003; Lundgren et al. 2004) lines provides information about the distributions of atomic and molecular gas in those galaxies. Many studies of these distributions are undertaken in the context of star formation. For example, one commonly addressed question concerns whether a column density of gas in excess of a local critical value leads to star formation (Kennicutt 1989).

As we have seen in previous chapters, applying a standard CO-to-H_2 factor to CO(1–0) observations can lead to a significant underestimate of the mass in molecular gas within metal-poor regions, such as those found in dwarf galaxies. Furthermore, the use of CO emission alone to map the molecular gas distribution within these regions may be inappropriate and combined studies including the [C II] fine-structure line may provide a more reliable inventory of the molecular gas reservoir in dwarf irregular galaxies (Madden et al. 1997; Madden 2002). This is consistent with the known difficulty in detecting CO emission in some dwarf and compact galaxies, compared to large spiral galaxies (e.g. Israel 2005). The possibility that molecular gas may be present in large quantities but undetected in such regions has been postulated (see, e.g., Pfenniger et al. 1994; Combes 2000; Kalberla et al. 2000, and references therein). In this scenario, molecular gas is proposed to reside in dense clumps with extents of the order of 10 AU and masses very much smaller than a Solar mass each. Such clumps would have a covering factor (or beam filling factor)

that is much smaller than unity. Their existence might have a range of observational consequences. For instance, they may be responsible for "extreme scattering events", causing large variations in radio signals from more distant sources (Walker & Wardle 1998).

Of course, no survey will lead to the detection of all neutral atomic or molecular gas in a galaxy. Sensitivity limits mean that mapped distributions have boundaries, even though the real gas distributions may be more extended. In this chapter, we attempt to determine physical parameters characterizing the gas and environment that might result in significant quantities of molecular gas being hidden, with column densities comparable to those often found by surveys to be associated with star formation. Such gas could provide a reservoir for eventual star formation, which would in turn create conditions leading to the gas being more easily detected. In many cases, the observed regions will be sufficiently distant that individual clouds are not observed. Where previous studies of this kind have concentrated on small, dense clumps (e.g. Pfenniger et al. 1994; Lawrence 2001), we focus attention on lower density, larger objects, having a covering factor near unity. We have assumed, in effect, that all clouds have the same total column density and that, on average, any line of sight will pass through one cloud.

We therefore consider the possible existence of molecular clouds that contain a significant column density of H_2 whilst producing sufficiently little emission that they are undetectable or at least ignored by those conducting most surveys. We produce theoretical models of the chemistry and emission arising in molecular clouds and conduct a parameter space search for physical conditions that might give rise to undetectable quantities of molecular gas. In Section 5.2 we describe the modifications to the UCL_PDR code used to calculate the chemical and emission properties of model clouds and outline the range of parameter space examined. In Section 5.3 we review the sensitivity limits of current telescopes appropriate to the detection of emission (in the IR/submm/mm/radio) from molecular clouds and specify the constraints we impose for a cloud to be considered undetectable. The results of the parameter space search are presented in Section 5.4 and we summarize our findings in Section 5.5.

5.2 Cloud model

The UCL_PDR time-dependent PDR code is again employed to calculate the chemistry, thermal balance and emission strengths of fine structure and molecular lines within model clouds, for a given set of physical parameters. Constant thermal pressure is assumed, and the density is calculated self-consistently with the temperature at each depth- and time-step. The turbulent contribution to

Table 5.1: Elemental abundances used in the reduced chemical network (relative to hydrogen nuclei).

He	7.50×10^{-2}	C	1.42×10^{-4}
O	3.19×10^{-4}	Mg	5.12×10^{-6}

Table 5.2: Species included in the reduced chemical network.

H, H^+, H_2, H_2^+, H_3^+, He, He^+
C, C^+, CH, CH^+, CH_2, CH_2^+, CH_3,
CH_3^+, CH_4, CH_4^+, CH_5^+, CO, CO^+, HCO^+
O, O^+, OH, OH^+, H_2O, H_2O^+, H_3O^+, O_2, O_2^+
Mg, Mg^+, e^-

the pressure is neglected. Self-gravity may be important in real clouds, and lead to some density variation. However, magnetic forces may also be important and counteract the gravity to a large extent. Given the uncertainities in the real density distributions, we consider the assumption of isobaric clouds to be reasonable.

A reduced chemical network is adopted for this study, containing 32 species and over 300 reactions, including ion-molecule, photoionization and photodissociation reactions. Freeze-out of atoms and molecules onto grains is again neglected. The gas-phase elemental abundances adopted are listed in Table 5.1 and are assumed to scale linearly with metallicity Z. The species included in the network are listed in Table 5.2. All fractional abundances in this paper are quoted relative to the hydrogen nuclei number density n. The reaction rates are drawn from the larger set typically used in the UCL_PDR code, which is based on the UMIST99 database (Le Teuff et al. 2000), with some modifications introduced as part of the PDR benchmarking effort (Röllig et al. 2006a).

Variation in the metallicity ($Z/Z_\odot$) is taken into account as before, through the assumption that the dust and PAH number densities, their photoelectric heating rates, the formation rate of H_2 on grains and the elemental metal abundances all scale linearly with Z.

Model parameter space

Two sets of initial conditions are assumed for the chemical abundances in the models: purely atomic (all hydrogen in H^0 and all carbon in C^0), or purely molecular (all hydrogen in H_2 and all carbon in

CO). These represent the two extremes for the initial state of the cloud, forming either from tenuous material or from dense cores that have subsequently relaxed to a diffuse state, therefore bracketing the range of possible starting conditions. Clouds that are initially molecular are considered to have originated from much denser material. Consequently, the outer layers of atomic hydrogen around them are narrow and the UCL_PDR code computes the H/H_2 transition accurately as these objects evolve. The abundances, temperature and emission properties are calculated at each time-step for a total period of 1 Gyr in each cloud model. Models are calculated for the entire region of parameter space with both sets of initial abundances.

Some correlation between the radiation field and the cosmic-ray ionization rate would be expected for extragalactic observations where a beam samples the average interstellar UV field and cosmic-ray flux incident on a cloud, as the high-mass stars that emit the bulk of the far ultraviolet radiation also become supernovae that create remnants in which cosmic-rays are accelerated. Therefore, the cosmic-ray ionization rate per hydrogen molecule (ζ) is assumed to scale linearly with the incident radiation field strength (χ Draine) as:

$$\zeta = 1.3 \times 10^{-17} \chi \qquad [\mathrm{s}^{-1}]. \tag{5.1}$$

A large region of parameter space is considered, but is restricted to low radiation intensities ($< 10^{-3}$ Draine). A lower limit to the radiation field is given by the metagalactic radiation field, which has been considered extensively recently by Sternberg et al. (2002). The spectral shapes of the standard Draine (1978) and the metagalactic radiation fields differ, but a comparison at 1000 Å implies that the metagalactic field is the weaker by four orders of magnitude. Of course, that field varies from point to point depending on the distances to the nearest bright galaxies. We consider a range of four orders of magnitude in metallicity and gas pressure. Table 5.3 lists the individual parameter values considered. Since regions where the radiation background is low compared to the Solar neighbourhood are far from stars which provide energy to stir their environments, such regions are likely to be fairly quiescent. The level of turbulence in the clouds considered here is expected to be significantly lower than is typically found in standard nearby Galactic giant molecular clouds (Williams et al. 1995). We therefore include models with microturbulent velocities in the range 0.05–0.5 $\mathrm{km\,s^{-1}}$. The assumed value of this velocity is important for the heating and cooling of the clouds and for the opacity in emission lines. It therefore plays an important role in the considerations of detectability. An ensemble of clouds possessing a cloud-cloud velocity dispersion would produce emission lines that are broader than those from the individual clouds; Wolfire et al. (1993) included such a cloud-cloud velocity dispersion in their models. We have not, in part because

Table 5.3: The range of values covered in the parameter space.

Parameter	Values taken for each parameter	
t	$10^1, 10^2, \ldots, 10^8, 10^9$	yr
Z	$10^0, 10^{-1}, 10^{-2}, 10^{-3}$	$Z_\odot$
P/k	$10^1, 10^2, 10^3, 10^4$	$\mathrm{cm^{-3}\,K}$
χ	$10^{-3}, 10^{-4}, 10^{-5}$	Draine
v_{turb}	0.05, 0.1, 0.3, 0.5	$\mathrm{km\,s^{-1}}$

regions where few supernovae occur will have small cloud-cloud velocity dispersions, and also in part to restrict the range of parameter space to a manageable level. The neglect of a cloud-cloud velocity dispersion leads to a more restricted region of parameter space corresponding to molecular dark matter that is difficult to detect.

In total, we have constructed 384 time-dependent cloud models to cover the specified parameter space. The next section contains the criteria used to determine what part of parameter space is associated with molecular dark matter.

5.3 Emission constraints

The distributions of neutral atomic and molecular clouds are studied predominantly with H I 21 cm, [O I], [C I] and [C II] fine structure and CO rotational lines, as well as dust continuum radiation. 21 cm surveys can lead to the six sigma detection of neutral atomic hydrogen column densities of 1.6×10^{18} $\mathrm{cm^{-2}}$ for a velocity dispersion of 10 $\mathrm{km\,s^{-1}}$ and a comparable velocity resolution (e.g. Giovanelli et al. 2005). However, published column density distributions of H I in other galaxies usually do not go to such low column densities. For instance, Walter et al. (2005) take a column density of 10^{20} $\mathrm{cm^{-2}}$ for the lowest contour in figures, and the lowest column density shown in figures by Noordermeer et al. (2005) is roughly 10^{19} $\mathrm{cm^{-2}}$. We shall use 10^{19} $\mathrm{cm^{-2}}$ as the minimum column density of neutral hydrogen to be considered of observational significance. Though we have cited observations that were sensitive to H I column densities roughly as low as 10^{19} $\mathrm{cm^{-2}}$, we realize that this is a rather small value. We have chosen to define such a low limiting value for the H I column density because the small velocity dispersions that we have assumed would make H I more readily detectable.

Ground-based observations of the lower CO rotational emission lines have a typical RMS noise

limit of $\sim$1 mK; we therefore adopt a minimum level for the detectable integrated line intensity of 0.01 K km s^{-1} (assuming a velocity resolution of 10 km s^{-1}), suitable for deep searches (e.g. Wilson & Combes 1998; Smoker et al. 2000). The noise limits on [C I] 610 μm ground-based observations are higher, but for convenience we also impose a constraint of 0.01 K km s^{-1} for the minimum detectable integrated line intensity.

The [O I] and [C II] fine structure lines are only observable from space or the upper atmosphere. Taking typical RMS noise limits for spectra obtained with the Long Wavelength Spectrometer (LWS) on the *Infrared Space Observatory* (*ISO*), a minimum integrated flux of $\sim 10^{-17}$ W m^{-2} is reasonable (assuming a resolution of 0.29 μm for the [O I] 63 μm line and 0.6 μm for the [C II] 158 μm line). This corresponds to a surface brightness $I \sim 10^{-7}$ erg s^{-1} cm^{-2} sr^{-1} (assuming $\Omega_b \sim 10^{-7}$ sr for the LWS; Lloyd 2003). We adopt this as the detection limit for the two dominant fine structure lines.

Since the dust in these clouds is cold (typically <5 K) and depleted at the lower metallicities, its emission will be faint and therefore unlikely to be detected above the background level.

To summarize, the limits for non-detection that we impose on the cloud models are: $N_{\rm H\,I} < 10^{19}$ cm^{-2}, $W_{\rm CO} < 0.01$ K km s^{-1} in all rotational lines, $W < 0.01$ K km s^{-1} for the [C I] 610 μm line, $I < 10^{-7}$ erg s^{-1} cm^{-2} sr^{-1} for the [O I] 63 μm and [C II] 158 μm lines. Any cloud model with emission below all these limits simultaneously is considered to be effectively undetectable with current technology. We now describe the results of the parameter space search, presenting models that meet these criteria.

5.4 Model results

The column density through the cloud is restricted in each model such that the total emission in each line is below the corresponding limit given above. For each set of physical parameters, the resulting cloud model therefore represents the maximum amount of molecular gas that can be hidden under those conditions. We then select cloud models that contain significant quantities of H_2, specifically $N_{H_2} \geq 10^{21}$ cm^{-2}, at some point during their 1 Gyr evolution. Such a column density is of the same order of magnitude as the hydrogen nuclei column densities associated with parts of large spiral galaxies in which stars form (e.g. Noordermeer et al. 2005). This subset of models defines the region of parameter space where significant amounts of molecular gas can reside without being detected in emission. Tables 5.4–5.7 list the subset of cloud models with initially molecular gas that meet the criteria for non-detectable emission whilst containing a significant amount of H_2.

Table 5.8 lists the subset of initially atomic cloud models that meet the same conditions. The tables also show the period of time for which this is the case in each model, starting at $t_{\rm min}$ and ending at $t_{\rm max}$, as well as the time, $t_{\rm high}$, at which the peak value of $N_{\rm H_2}$ is reached. In total, 111 of the 384 model clouds obtain H_2 column densities $\geq 10^{21}$ cm^{-2} for some period of their evolution. The trends describing the change in total H_2 column density with parameter variation are discussed in the next two sections.

5.4.1 Initially molecular clouds

For models for which the gas is initially molecular, the peak H_2 column density ($>10^{24}$ cm^{-2}) occurs in the cloud with the lowest turbulent velocity, subject to the lowest incident radiation field strength, with low metallicity and with the highest pressure (0.05 km s^{-1}, 10^{-5} Draine, 10^{-2} $Z_{\odot}$, 10^4 cm^{-3} K; see Table 5.4 and Figure 5.1). For the lowest radiation field strength, in the models with low turbulent velocities (0.05 or 0.1 km s^{-1}), the H_2 column density increases as the pressure rises and it is the intermediate metallicities (10^{-1}–10^{-2} $Z_{\odot}$) that produce the highest column densities of dark material. For models for which the radiation field does not have its lowest value, the H_2 column density increases as the pressure and metallicity drop (see Figure 5.1).

At the lowest metallicity considered (10^{-3} $Z_{\odot}$), the H_2 column density is $\geq 10^{21}$ cm^{-2} for almost all combinations of turbulent velocity, radiation field strength and pressure (see the bottom right panel of Figure 5.2 for the $v_{\rm turb} = 0.05$ km s^{-1} case). The only exceptions are the three cloud models with the lowest incident radiation and highest pressure at turbulent velocities of 0.3 and 0.5 km s^{-1} (see Tables 5.6 and 5.7). Overall, increasing turbulent velocity within the cloud serves to reduce the H_2 column density that can be hidden, although some of the low pressure models show a slight increase in $N_{\rm H_2}$ at higher turbulent velocities.

The period of time for which $N_{\rm H_2} \geq 10^{21}$ cm^{-2} in each model (i.e. from $t_{\rm min}$ to $t_{\rm max}$) is governed by the restrictions placed on the CO and H I emission. For cloud models with $t_{\rm min} > 0$, the 2.6 mm CO(1–0) line emission is initially above the limit given in Section 5.3 and therefore considered detectable, but falls below the limit once $t_{\rm min}$ is reached. In models with $t_{\rm max} < 1$ Gyr, the maximum time considered in the calculations, the 21 cm H I emission rises above its detection limit at late times, reducing the period for which the cloud remains undetectable. This is generally the case for models with higher radiation field strengths.

An analysis of the thermal balance in the models shows that the dominant cooling processes are emission in the lower rotational transitions of CO and the fine structure lines of neutral carbon, with some contribution from collisions with the cooler dust grains in the high pressure models. The

Table 5.4: Molecular models with $v_{\rm turb} = 0.05$ km s^{-1} that satisfy the criteria of undetectable emission and $N_{\rm H_2} \geq 10^{21}$ cm^{-2}. $N_{\rm H_2}$ is the peak H_2 column density, reached at time $t_{\rm high}$. The period of time for which $N_{\rm H_2} \geq 10^{21}$ cm^{-2} in each model is defined by $t_{\rm min}$ and $t_{\rm max}$.

Z ($Z_\odot$)	χ (Draine)	P/k (cm^{-3} K)	$N_{\rm H_2}$ (cm^{-2})	$t_{\rm high}$ (yr)	$t_{\rm min}$ (yr)	$t_{\rm max}$ (yr)
10^{0}	10^{-5}	10^{3}	2.9×10^{22}	7×10^{6}	0×10^{0}	1×10^{9}
10^{0}	10^{-5}	10^{4}	2.9×10^{22}	3×10^{7}	0×10^{0}	1×10^{9}
10^{-1}	10^{-3}	10^{1}	2.4×10^{21}	1×10^{7}	6×10^{6}	1×10^{7}
10^{-1}	10^{-4}	10^{1}	2.3×10^{21}	6×10^{8}	8×10^{7}	8×10^{8}
10^{-1}	10^{-5}	10^{1}	6.0×10^{21}	3×10^{7}	0×10^{0}	1×10^{9}
10^{-1}	10^{-5}	10^{2}	6.3×10^{21}	4×10^{3}	0×10^{0}	1×10^{9}
10^{-1}	10^{-5}	10^{3}	1.2×10^{22}	1×10^{6}	0×10^{0}	1×10^{9}
10^{-1}	10^{-5}	10^{4}	2.8×10^{23}	4×10^{7}	0×10^{0}	1×10^{9}
10^{-2}	10^{-3}	10^{1}	5.3×10^{21}	9×10^{6}	3×10^{6}	1×10^{7}
10^{-2}	10^{-3}	10^{2}	4.7×10^{21}	8×10^{6}	4×10^{6}	1×10^{7}
10^{-2}	10^{-3}	10^{3}	1.6×10^{21}	5×10^{7}	2×10^{7}	1×10^{8}
10^{-2}	10^{-4}	10^{1}	5.5×10^{21}	9×10^{7}	0×10^{0}	1×10^{8}
10^{-2}	10^{-4}	10^{2}	2.8×10^{21}	5×10^{8}	0×10^{0}	1×10^{9}
10^{-2}	10^{-4}	10^{3}	1.1×10^{21}	1×10^{9}	0×10^{0}	1×10^{9}
10^{-2}	10^{-5}	10^{1}	2.6×10^{22}	0×10^{0}	0×10^{0}	1×10^{9}
10^{-2}	10^{-5}	10^{2}	2.4×10^{22}	3×10^{5}	0×10^{0}	1×10^{9}
10^{-2}	10^{-5}	10^{3}	2.8×10^{22}	0×10^{0}	0×10^{0}	1×10^{9}
10^{-2}	10^{-5}	10^{4}	1.2×10^{24}	0×10^{0}	0×10^{0}	1×10^{9}
10^{-3}	10^{-3}	10^{1}	1.2×10^{22}	9×10^{6}	2×10^{5}	1×10^{7}
10^{-3}	10^{-3}	10^{2}	9.1×10^{21}	1×10^{7}	2×10^{6}	1×10^{7}
10^{-3}	10^{-3}	10^{3}	7.9×10^{21}	9×10^{6}	3×10^{6}	1×10^{7}
10^{-3}	10^{-3}	10^{4}	3.5×10^{21}	2×10^{7}	3×10^{6}	7×10^{7}
10^{-3}	10^{-4}	10^{1}	1.0×10^{22}	8×10^{7}	0×10^{0}	1×10^{8}
10^{-3}	10^{-4}	10^{2}	1.0×10^{22}	9×10^{7}	0×10^{0}	1×10^{8}
10^{-3}	10^{-4}	10^{3}	9.1×10^{21}	2×10^{8}	0×10^{0}	9×10^{8}
10^{-3}	10^{-4}	10^{4}	3.3×10^{21}	1×10^{9}	0×10^{0}	1×10^{9}
10^{-3}	10^{-5}	10^{1}	2.1×10^{22}	9×10^{8}	0×10^{0}	1×10^{9}
10^{-3}	10^{-5}	10^{2}	2.0×10^{22}	9×10^{4}	0×10^{0}	1×10^{9}
10^{-3}	10^{-5}	10^{3}	2.0×10^{22}	2×10^{4}	0×10^{0}	1×10^{9}
10^{-3}	10^{-5}	10^{4}	3.2×10^{22}	2×10^{5}	0×10^{0}	1×10^{9}

Table 5.5: Molecular models with $v_{\rm turb} = 0.1$ km s^{-1} that satisfy the criteria of undetectable emission and $N_{\rm H_2} \geq 10^{21}$ cm^{-2}. $N_{\rm H_2}$ is the peak H_2 column density, reached at time $t_{\rm high}$. The period of time during which $N_{\rm H_2} \geq 10^{21}$ cm^{-2} in each model is defined by $t_{\rm min}$ and $t_{\rm max}$.

Z ($Z_\odot$)	χ (Draine)	P/k (cm^{-3} K)	$N_{\rm H_2}$ (cm^{-2})	$t_{\rm high}$ (yr)	$t_{\rm min}$ (yr)	$t_{\rm max}$ (yr)
10^{0}	10^{-5}	10^{4}	2.9×10^{22}	2×10^{6}	0×10^{0}	1×10^{9}
10^{-1}	10^{-3}	10^{1}	1.4×10^{21}	9×10^{6}	8×10^{6}	1×10^{7}
10^{-1}	10^{-3}	10^{2}	2.6×10^{21}	4×10^{7}	1×10^{7}	1×10^{8}
10^{-1}	10^{-4}	10^{1}	2.5×10^{21}	5×10^{8}	1×10^{8}	1×10^{9}
10^{-1}	10^{-5}	10^{1}	2.7×10^{21}	6×10^{5}	0×10^{0}	1×10^{9}
10^{-1}	10^{-5}	10^{2}	2.7×10^{21}	0×10^{0}	0×10^{0}	1×10^{9}
10^{-1}	10^{-5}	10^{3}	3.1×10^{21}	2×10^{5}	0×10^{0}	1×10^{9}
10^{-1}	10^{-5}	10^{4}	7.0×10^{22}	5×10^{5}	0×10^{0}	1×10^{9}
10^{-2}	10^{-3}	10^{1}	5.0×10^{21}	9×10^{6}	4×10^{6}	1×10^{7}
10^{-2}	10^{-3}	10^{2}	4.0×10^{21}	8×10^{6}	4×10^{6}	1×10^{7}
10^{-2}	10^{-3}	10^{3}	1.7×10^{21}	7×10^{7}	2×10^{7}	9×10^{7}
10^{-2}	10^{-4}	10^{1}	4.5×10^{21}	8×10^{7}	4×10^{7}	1×10^{8}
10^{-2}	10^{-4}	10^{2}	3.0×10^{21}	4×10^{8}	6×10^{7}	1×10^{9}
10^{-2}	10^{-4}	10^{3}	1.0×10^{21}	9×10^{8}	8×10^{8}	9×10^{8}
10^{-2}	10^{-5}	10^{1}	3.0×10^{21}	9×10^{3}	0×10^{0}	1×10^{9}
10^{-2}	10^{-5}	10^{2}	2.9×10^{21}	0×10^{0}	0×10^{0}	1×10^{9}
10^{-2}	10^{-5}	10^{3}	3.1×10^{21}	2×10^{6}	0×10^{0}	1×10^{9}
10^{-2}	10^{-5}	10^{4}	4.6×10^{21}	7×10^{5}	0×10^{0}	1×10^{9}
10^{-3}	10^{-3}	10^{1}	1.2×10^{22}	1×10^{7}	5×10^{4}	1×10^{7}
10^{-3}	10^{-3}	10^{2}	1.1×10^{22}	1×10^{7}	2×10^{6}	1×10^{7}
10^{-3}	10^{-3}	10^{3}	6.8×10^{21}	9×10^{6}	3×10^{6}	1×10^{7}
10^{-3}	10^{-3}	10^{4}	4.0×10^{21}	3×10^{7}	5×10^{6}	8×10^{7}
10^{-3}	10^{-4}	10^{1}	1.1×10^{22}	1×10^{8}	2×10^{6}	1×10^{8}
10^{-3}	10^{-4}	10^{2}	1.0×10^{22}	9×10^{7}	8×10^{6}	1×10^{8}
10^{-3}	10^{-4}	10^{3}	7.8×10^{21}	2×10^{8}	2×10^{7}	1×10^{9}
10^{-3}	10^{-4}	10^{4}	3.0×10^{21}	9×10^{8}	5×10^{7}	1×10^{9}
10^{-3}	10^{-5}	10^{1}	1.1×10^{22}	9×10^{8}	0×10^{0}	1×10^{9}
10^{-3}	10^{-5}	10^{2}	8.1×10^{21}	1×10^{9}	0×10^{0}	1×10^{9}
10^{-3}	10^{-5}	10^{3}	3.1×10^{21}	1×10^{9}	0×10^{0}	1×10^{9}
10^{-3}	10^{-5}	10^{4}	1.7×10^{21}	4×10^{5}	0×10^{0}	1×10^{9}

Table 5.6: Molecular models with $v_{\rm turb} = 0.3$ km s^{-1} that satisfy the criteria of undetectable emission and $N_{\rm H_2} \geq 10^{21}$ cm^{-2}. $N_{\rm H_2}$ is the peak H_2 column density, reached at time $t_{\rm high}$. The period of time during which $N_{\rm H_2} \geq 10^{21}$ cm^{-2} in each model is defined by $t_{\rm min}$ and $t_{\rm max}$.

Z	χ	P/k	$N_{\rm H_2}$	$t_{\rm high}$	$t_{\rm min}$	$t_{\rm max}$
($Z_\odot$)	(Draine)	(cm^{-3} K)	(cm^{-2})	(yr)	(yr)	(yr)
10^{-1}	10^{-3}	10^{1}	2.0×10^{21}	5×10^{6}	5×10^{6}	1×10^{7}
10^{-1}	10^{-3}	10^{2}	2.3×10^{21}	1×10^{8}	7×10^{6}	1×10^{8}
10^{-1}	10^{-4}	10^{1}	3.4×10^{21}	9×10^{8}	4×10^{7}	1×10^{9}
10^{-2}	10^{-3}	10^{1}	5.6×10^{21}	9×10^{6}	3×10^{6}	1×10^{7}
10^{-2}	10^{-3}	10^{2}	4.4×10^{21}	9×10^{6}	3×10^{6}	1×10^{7}
10^{-2}	10^{-3}	10^{3}	1.5×10^{21}	3×10^{7}	5×10^{6}	1×10^{8}
10^{-2}	10^{-4}	10^{1}	5.1×10^{21}	7×10^{7}	3×10^{7}	1×10^{8}
10^{-2}	10^{-4}	10^{2}	5.5×10^{21}	2×10^{8}	4×10^{7}	1×10^{9}
10^{-2}	10^{-5}	10^{1}	5.3×10^{21}	1×10^{9}	4×10^{8}	1×10^{9}
10^{-2}	10^{-5}	10^{2}	1.7×10^{21}	1×10^{9}	5×10^{8}	1×10^{9}
10^{-3}	10^{-3}	10^{1}	1.2×10^{22}	9×10^{6}	0×10^{0}	1×10^{7}
10^{-3}	10^{-3}	10^{2}	1.2×10^{22}	1×10^{7}	2×10^{5}	1×10^{7}
10^{-3}	10^{-3}	10^{3}	6.0×10^{21}	9×10^{6}	3×10^{6}	1×10^{7}
10^{-3}	10^{-3}	10^{4}	1.9×10^{21}	7×10^{6}	5×10^{6}	1×10^{8}
10^{-3}	10^{-4}	10^{1}	1.3×10^{22}	1×10^{8}	0×10^{0}	1×10^{8}
10^{-3}	10^{-4}	10^{2}	9.3×10^{21}	9×10^{7}	2×10^{6}	1×10^{8}
10^{-3}	10^{-4}	10^{3}	3.9×10^{21}	7×10^{7}	3×10^{7}	1×10^{9}
10^{-3}	10^{-4}	10^{4}	2.2×10^{21}	6×10^{8}	8×10^{7}	1×10^{9}
10^{-3}	10^{-5}	10^{1}	1.2×10^{22}	1×10^{9}	0×10^{0}	1×10^{9}
10^{-3}	10^{-5}	10^{2}	1.0×10^{22}	1×10^{9}	2×10^{7}	1×10^{9}
10^{-3}	10^{-5}	10^{3}	3.5×10^{21}	6×10^{8}	3×10^{8}	1×10^{9}

Table 5.7: Molecular models with $v_{\rm turb} = 0.5$ km s^{-1} that satisfy the criteria of undetectable emission and $N_{\rm H_2} \geq 10^{21}$ cm^{-2}. $N_{\rm H_2}$ is the peak H_2 column density, reached at time $t_{\rm high}$. The period of time during which $N_{\rm H_2} \geq 10^{21}$ cm^{-2} in each model is defined by $t_{\rm min}$ and $t_{\rm max}$.

Z	χ	P/k	$N_{\rm H_2}$	$t_{\rm high}$	$t_{\rm min}$	$t_{\rm max}$
($Z_\odot$)	(Draine)	(cm^{-3} K)	(cm^{-2})	(yr)	(yr)	(yr)
10^{-1}	10^{-3}	10^{1}	1.5×10^{21}	1×10^{7}	9×10^{6}	1×10^{7}
10^{-1}	10^{-3}	10^{2}	2.8×10^{21}	6×10^{7}	8×10^{6}	1×10^{8}
10^{-1}	10^{-4}	10^{1}	3.9×10^{21}	6×10^{8}	9×10^{7}	1×10^{9}
10^{-2}	10^{-3}	10^{1}	4.0×10^{21}	1×10^{7}	4×10^{6}	1×10^{7}
10^{-2}	10^{-3}	10^{2}	5.3×10^{21}	1×10^{7}	4×10^{6}	1×10^{7}
10^{-2}	10^{-3}	10^{3}	1.3×10^{21}	2×10^{7}	6×10^{6}	1×10^{8}
10^{-2}	10^{-4}	10^{1}	3.8×10^{21}	1×10^{8}	4×10^{7}	1×10^{8}
10^{-2}	10^{-4}	10^{2}	5.7×10^{21}	4×10^{8}	5×10^{7}	1×10^{9}
10^{-2}	10^{-5}	10^{1}	3.4×10^{21}	1×10^{9}	4×10^{8}	1×10^{9}
10^{-2}	10^{-5}	10^{2}	2.2×10^{21}	1×10^{9}	6×10^{8}	1×10^{9}
10^{-3}	10^{-3}	10^{1}	9.4×10^{21}	1×10^{7}	0×10^{0}	1×10^{7}
10^{-3}	10^{-3}	10^{2}	8.0×10^{21}	1×10^{7}	2×10^{5}	1×10^{7}
10^{-3}	10^{-3}	10^{3}	5.1×10^{21}	9×10^{6}	3×10^{6}	1×10^{7}
10^{-3}	10^{-3}	10^{4}	1.1×10^{21}	5×10^{6}	5×10^{6}	9×10^{7}
10^{-3}	10^{-4}	10^{1}	1.1×10^{22}	1×10^{8}	0×10^{0}	1×10^{8}
10^{-3}	10^{-4}	10^{2}	8.4×10^{21}	1×10^{8}	2×10^{6}	1×10^{8}
10^{-3}	10^{-4}	10^{3}	3.9×10^{21}	8×10^{7}	2×10^{7}	1×10^{9}
10^{-3}	10^{-5}	10^{1}	1.0×10^{22}	1×10^{9}	0×10^{0}	1×10^{9}
10^{-3}	10^{-5}	10^{2}	8.3×10^{21}	1×10^{9}	8×10^{6}	1×10^{9}
10^{-3}	10^{-5}	10^{3}	3.3×10^{21}	9×10^{8}	3×10^{8}	1×10^{9}

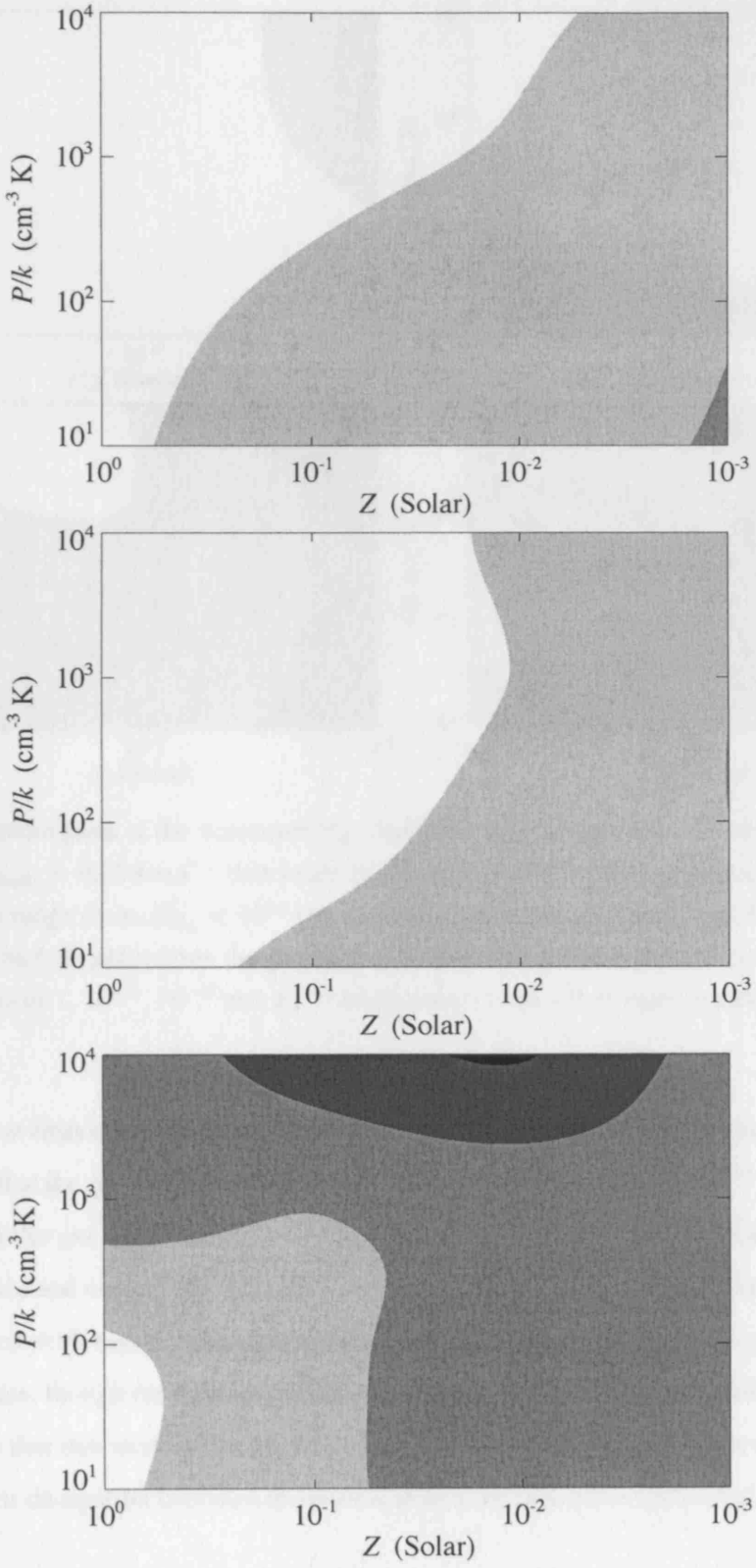

Figure 5.1: Contour plots of the maximum H_2 column density produced by initially molecular cloud models with $v_{\rm turb} = 0.05$ km s^{-1} that meet the criteria of undetectable emission (see Section 5.3). Contour levels range from $N_{H_2} < 10^{21}$ cm^{-2} (white), through 10^{21}, 10^{22} and 10^{23} cm^{-2}, to $N_{H_2} \geq 10^{24}$ cm^{-2} (black). The three plots show the pressure-metallicity plane of the parameter space considered, for incident radiation field strengths of 10^{-3}, 10^{-4} and 10^{-5} Draine (from top to bottom).

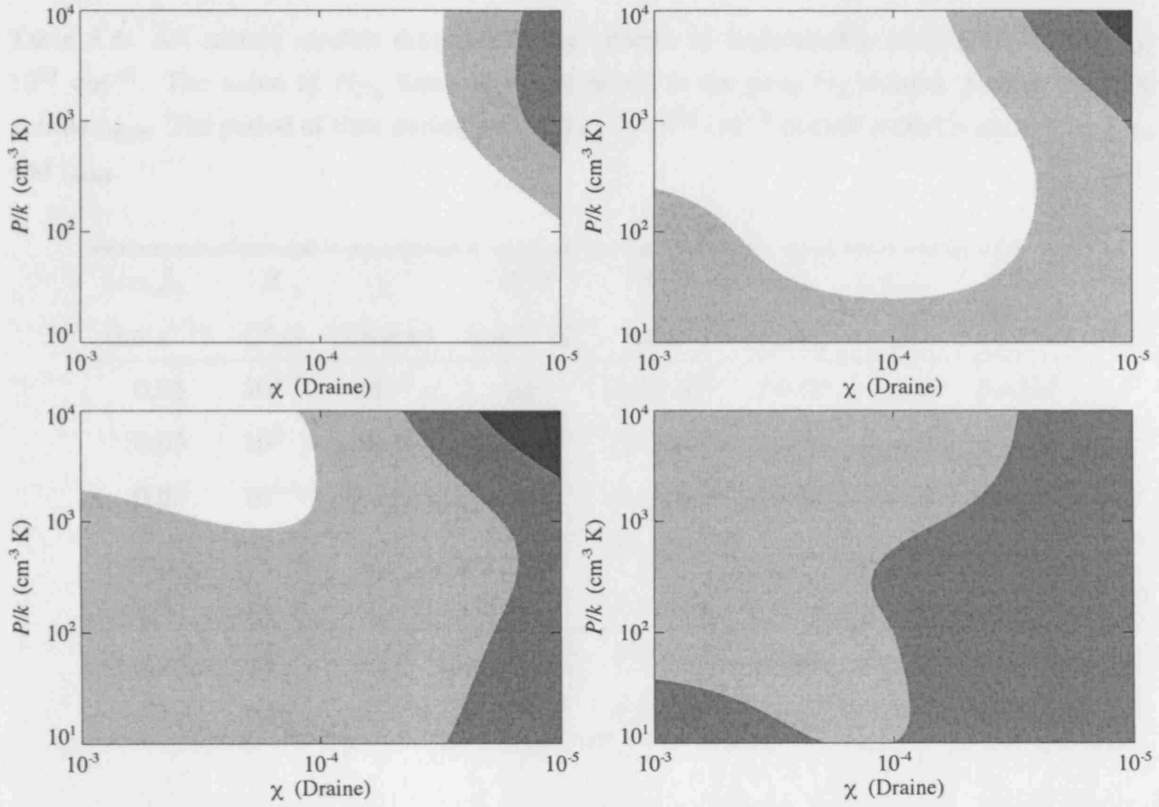

Figure 5.2: Contour plots of the maximum H_2 column density produced by initially molecular cloud models with $v_{\rm turb} = 0.05$ km s^{-1} that meet the criteria of undetectable emission (see Section 5.3). Contour levels range from $N_{\rm H_2} < 10^{21}$ cm^{-2} (white), through 10^{21}, 10^{22} and $N_{\rm H_2} \geq 10^{23}$ cm^{-2} (dark-grey). The four plots show the pressure-radiation plane of the parameter space considered, for metallicities of 1, 10^{-1}, 10^{-2} and 10^{-3} times Solar (from left to right, top to bottom).

reason that these lines dominate, rather the [C II] and [O I] fine structure lines that typically govern the cooling, is that the gas temperatures in these clouds are too low to excite the C^+ and O transitions. The heating of the gas at the cloud surface is dominated by H_2 formation and photodissociation, whilst turbulence and cosmic-ray ionization become important heating mechanisms deeper into the cloud. In models with higher radiation field strengths, PAH photoelectric heating plays a role near the cloud surface, though the reduced metallicity and the corresponding reduction in grain number density means that this mechanism plays a lesser role than in PDRs at Solar metallicity. Heating due to turbulent dissipation becomes the dominant heating process at higher turbulent velocities.

5.4.2 Initially atomic clouds

From Table 5.8 it can be seen that there are significantly fewer models for which the gas is initially atomic that can produce appreciable quantities of hidden molecular gas. This is mainly due to the

Table 5.8: All atomic models that satisfy the criteria of undetectable emission and $N_{H_2} \geq 10^{21}$ cm^{-2}. The value of N_{H_2} listed for each model is the peak H_2 column density, reached at time t_{high}. The period of time during which $N_{H_2} \geq 10^{21}$ cm^{-2} in each model is defined by t_{min} and t_{max}.

v_{turb} (km s^{-1})	Z ($Z_\odot$)	χ (Draine)	P/k (cm^{-3} K)	N_{H_2} (cm^{-2})	t_{high} (yr)	t_{min} (yr)	t_{max} (yr)
0.05	10^0	10^{-5}	10^3	1.8×10^{21}	2×10^8	2×10^8	1×10^9
0.05	10^0	10^{-5}	10^4	2.9×10^{22}	2×10^7	2×10^7	1×10^9
0.05	10^{-1}	10^{-5}	10^3	2.1×10^{21}	1×10^9	9×10^8	1×10^9
0.05	10^{-1}	10^{-5}	10^4	7.4×10^{22}	3×10^8	2×10^8	1×10^9
0.05	10^{-2}	10^{-5}	10^4	1.1×10^{21}	1×10^9	1×10^9	1×10^9
0.1	10^0	10^{-5}	10^4	2.9×10^{22}	2×10^7	2×10^7	1×10^9
0.1	10^{-1}	10^{-5}	10^3	1.5×10^{21}	1×10^9	1×10^9	1×10^9

relatively long time-scales required for molecular hydrogen formation under the physical conditions being considered here. However, despite this limitation, there still exists a well-defined region of parameter space within which atomic gas can evolve to form large column densities of molecular gas whilst remaining undetectable in emission by the usual tracers.

In all the models listed in Table 5.8, the radiation field strength is the lowest considered in the parameter space (10^{-5} Draine) and the pressures are among the highest (10^3 or 10^4 cm^{-3} K). There is some spread in metallicity, but there are no clouds with turbulent velocities above 0.1 km s^{-1} that have $\geq 10^{21}$ cm^{-2} of H_2. The peak H_2 column density is 7.4×10^{22} cm^{-2}, some 20 times smaller than the largest column density obtained by clouds evolving from molecular gas. None of the initially atomic clouds reach $N_{H_2} \geq 10^{21}$ cm^{-2} until they have existed for 20 Myr or longer; several of the cloud models do not obtain significant H_2 column densities until 1 Gyr has passed. The heating and cooling of the gas is governed by the processes discussed in the previous section, although the heating due to the formation of H_2 is more significant in these models, since the hydrogen is initially atomic.

5.5 Conclusions

We have conducted a large study of the parameter space associated with regions where the radiation field is weak relative to that in the Solar vicinity in order to search for conditions that give rise to significant quantities of molecular gas with emission strengths that are comparable to the lower limits considered in standard surveys. Having explored parameter space to identify the time-dependent cloud models that satisfy these limits, we selected those models in which a significant column density of molecular hydrogen, $N_{H_2} \geq 10^{21}$ cm^{-2} was reached.

We find that there is a large region within the parameter space that meets these requirements, resulting in clouds that might contain a significant mass of molecular gas whilst remaining effectively undetectable or at least not particularly noticeable in surveys. This region is characterized by low turbulent velocities ($\leq$0.1 km s^{-1}), low radiation fields ($\leq 10^{-4}$ Draine), normal to low metallicities ($\sim$1–10^{-2} $Z_{\odot}$) and intermediate pressures ($\sim 10^{3}$–10^{4} cm^{-3} K). Clouds forming from molecular gas under these conditions are capable of maintaining large amounts of H_2 without becoming detectable in emission. Initially atomic gas can also form significant column densities of molecular material with undetectable emission, but the time-scales required are much longer (>10 Myr).

Sternberg et al. (2002) conducted a study of PDRs in which they assumed the present metagalactic radiation field to be incident on clouds in work on minihaloes composed of cold dark matter of the variety considered in many cosmological studies and on compact high velocity H I clouds. As mentioned above, the radiation field that they assumed is of comparable strength at 1000 Å to fields for which we found large amounts of dark molecular gas to exist. Hence, there is some overlap between their work and mine. However, their emphasis is on H I clouds detectable in 21 cm emission, whereas the focus of this study is on the possible existence of dark molecular gas with substantial enough column densities to serve as reservoirs for potential star formation. They address observations of H I clouds having total hydrogen column densities of an order of magnitude or more below those considered here. Of interest here is whether regions of much higher column density may harbour sufficient molecular gas to become sites of stellar birth while they remain hidden in current surveys. Molecular dark matter existing in regions far away from bright stars may also lead to future star formation in some galaxies, occurring significantly beyond the currently detected boundaries of those galaxies.

Finally, we note that an H_2 column density of 10^{21} cm^{-2} distributed evenly over a disc with a radius of 40 kpc would correspond to a mass of 10^{11} $M_{\odot}$, sufficient to be of dynamical importance

in some galaxies. Thus, at least part of the dark matter problem for the Milky Way galaxy might be resolved by baryonic matter in the form of currently undetected molecular clouds at high Galactocentric radius.

A means of placing limits on the product of the covering factor of this type of molecular dark matter and the mean surface area per galaxy over which it is distributed would be through millimetre-wave absorption observations of other galaxies similar to those made by Liszt & Lucas (1998) to study diffuse clouds in our galaxy. Observations towards many background sources would almost certainly be required to set meaningful limits on that product, as a detection rate of about 4 optical QSO absorption systems per unit redshift at a redshift of $\sim$1 implies that intervening galaxies must have radii of almost 100 kpc if they are randomly oriented discs (e.g. Sargent et al. 1979). Zwaan & Prochaska (2006) have argued that a redshift interval of $\Delta z \approx 100$ has been covered in the CORALS survey of radio-selected quasars (Ellison et al. 2001), whereas a Δz range on the order of 3300 near $z = 0$ should be required to discover a high H_2 column density absorber at the present epoch, if H_2 has the sort of distribution in galaxies that is inferred from the BIMA SONG maps of CO in nearby galaxies (Helfer et al. 2003).

CHAPTER 6

OTHER APPLICATIONS OF THE UCL_PDR CODE

6.1 The chemistry of transient microstructure in the diffuse interstellar medium

The work presented in this section is based on the paper by Bell et al. (2005).

6.1.1 Introduction

Observational evidence for microstructure on a Solar-system scale in the diffuse interstellar medium has been accumulating for the last three decades. Measurements include very long baseline interferometry (VLBI) of H I 21 cm absorption towards extragalactic sources (Dieter et al. 1976; Diamond et al. 1989; Davis et al. 1996), absorption of atomic lines towards transversely moving pulsars (Frail et al. 1994), absorption differences towards stellar binaries (Meyer & Blades 1996; Lauroesch et al. 2000) and towards multiple systems and clusters (Kemp et al. 1993; Langer et al. 1990; Lauroesch & Meyer 1999), and secular variations over intervals of a few years along the line of sight to single stars (Hobbs et al. 1991; Danks & Sembach 1995; Blades et al. 1997; Cha & Sembach 2000; Crawford et al. 2000; Price et al. 2000; Danks et al. 2001; Welty & Fitzpatrick 2001). Marscher et al. (1993) find secular changes in formaldehyde absorption towards extragalactic sources, the first report of molecular tracers of microstructure. Moore & Marscher (1995) infer structure on scales of order 10 AU, with number densities possibly larger than 10^6 cm^{-3}, from further formaldehyde observations towards extragalactic sources. They also find spatial variations

in formaldehyde and hydroxyl absorption line profiles towards the extended radio galaxy 3C 111. Lucas & Liszt (1993) and Liszt & Lucas (2000) have used similar observations to explore the range of chemistry in diffuse and translucent clouds. It is also well known (Falgarone et al. 1992) that structure at larger scales ($\sim$ 0.01 pc) exists in nearby clouds.

Crawford (2002) has recently detected absorption in lines of CH at the specific velocity (different to that of the surrounding medium) of a previously reported variable component in the line of sight to κ Vel. Using a simple chemical model, Crawford obtained a value for the number density of the CH-containing microstructure towards κ Vel that was consistent with the density inferred from measurements of the Ca I/Ca II ratio at the same velocity component: $n \sim 10^3$ cm^{-3}. The measured CH column density would require the path-length to be more than 1 order of magnitude larger than the assumed transverse size, supporting the view that the structure may be extended in the line of sight, either as a filament or a sheet.

The most detailed study of molecular microstructure to date has been made by Rollinde et al. (2003). These authors made spectroscopic observations of the runaway reddened star HD 34078 (whose velocity transverse to the line of sight is $\sim$100 km s^{-1}) over a 3-yr period, supplemented by data from earlier epochs, to probe the foreground cloud distributions of CH, CH$^+$, CN and DIB carriers on scales from 1–150 AU. Their results show that the CH column density increased by 20% in 10 yr while the CH$^+$ column density and two DIB strengths were unchanged. The CN column density shows a modest rise in this period.

Although some authors have argued that some of the radio evidence for microstructure is flawed by poor data handling (e.g. Stanimirović et al. 2003), the evidence in favour of the existence of microstructure now seems overwhelming. The general conclusion is that microstructure has a scale of 10–100 AU and has typical densities much larger than the ambient interstellar density. The transverse visual extinction is therefore very small and the gas in the structure can only be poorly shielded from the interstellar radiation field.

The origin of the microstructure has been the subject of intense study (e.g. Pety & Falgarone 2000; Gwinn 2001). Some authors argue that it cannot originate through non-magnetic hydrodynamics and it has been suggested that it may be excited in regions of high magnetic pressure by slow-mode magnetosonic waves (Hartquist et al. 2003). However it is formed, it is overpressured and must be transient. Rollinde et al. (2003) inferred from their observations that the variations were not the result of dense clumps passing through the line of sight. It is unclear whether these structures are extended, i.e. filamentary or sheet-like, or whether they are compact objects. Extended objects could have longer path-lengths along the line of sight, if the orientation is suitable, and therefore

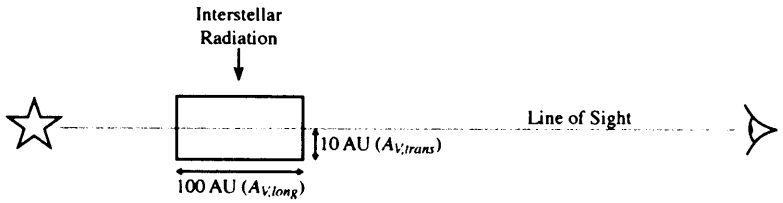

Figure 6.1: Model geometry of microstructure at the velocity of the variable component in the line of sight to κ Vel (different from that of the surrounding medium) with a depth transverse to the line of sight of 10 AU and an elongated length along the line of sight of 100 AU. The interstellar radiation field striking the microstructure transversely to the line of sight drives the chemistry in the microstructure, its intensity falling off with $A_{V,\mathrm{trans}}$. The contribution to column densities from species within the microstructure is calculated along the line of sight through the structure, over a visual extinction $A_{V,\mathrm{long}}$.

the constraints on density could be relaxed as compared with compact objects. The geometry may be related to the origin of these objects.

In this section we explore the chemistry that may arise in the conditions apparently appropriate for the transient microstructure: rapid transition from relatively low to relatively high density, low temperature, very low transverse visual extinction, and subject to the normal interstellar radiation and cosmic-ray fields. In Section 6.1.2, we describe the use of the UCL_PDR code in this work, and present in Section 6.1.3 our predictions of detectable chemistry as functions of time and depth into the slab. In Section 6.1.4, we describe the region of parameter space in which detectable molecular column densities might be found and discuss the relevance of possible detections to the geometry of the structure.

6.1.2 The model

We use the UCL_PDR code to model the region as a semi-infinite slab illuminated from one side; the density rises as a step function at the edge of the slab. We compute the chemistry as a function of time and transverse depth position within the slab, restricting our attention to the edge region (see Figure 6.1). What is unusual about this calculation compared to other studies of diffuse clouds is that the region of interest into the slab transversely to the line of sight is restricted to $\sim$ 10 AU and to a very short evolutionary age, typically less than 10^3 yr. These tiny spatial and time domains are usually ignored in studies of diffuse clouds (but note the models proposed by Cecchi-Pestellini

Table 6.1: Gas-phase elemental abundances used in the microstructure model (relative to total hydrogen nuclei).

He	7.5×10^{-2}	C	1.8×10^{-4}	N	8.5×10^{-5}
O	4.5×10^{-4}	Na	8.8×10^{-7}	Mg	5.1×10^{-6}
Si	8.2×10^{-7}	S	1.4×10^{-6}	Cl	1.1×10^{-7}
Ca	5.7×10^{-10}	Fe	6.2×10^{-7}		

& Dalgarno 2000 to account for H_3^+ and other species in the line of sight towards Cygnus OB2). The UCL_PDR code, however, is well adapted to such studies of early time and edge effects.

While the physical structure of the slab is assumed fixed, the chemistry within it will be strongly time- and depth-dependent. The gas-phase elemental abundances used in this work differ slightly from those typically used in the UCL_PDR code and so are listed in Table 6.1 (this study was conducted prior to the revision of the standard elemental abundances used in the current version of the code). The fraction of hydrogen initially contained in H_2 is unknown; the chemistry will depend strongly on this factor. We note that the structures are dense and, if set up as proposed by Hartquist et al. (2003), would be found in post-shock regions. Hence, it is plausible to assume a significant fraction of H_2 in the slab. We have arbitrarily set $n(H_2)/n = 0.4$, and we note that the chemical abundances predicted by the model should be proportional to this parameter. Since we are considering the *additional contribution* to molecular species produced by chemistry in the microstructure, all other molecular abundances are set to zero initially. The standard chemical network is used in the code (see Section 2.1.4). Freeze-out and mantle evaporation processes have been neglected due to the short time-scales over which these structures evolve and their low visual extinction. The filamentary or sheet-like nature of such objects is accounted for by assuming that the line of sight is within the slab and at a transverse depth of 10 AU from its surface (see Figure 6.1). Column densities are then simply proportional to the length of the line of sight within the slab.

Since the physical conditions within these regions are uncertain, a reasonably large range of parameter space is examined to provide a thorough investigation of microstructure chemistry. The effect of varying the slab density n (also referred to occasionally in this section as n_H) and age t, as well as the environmental parameters of incident radiation field strength and cosmic-ray ionization rate ζ are all considered, producing a four-dimensional grid of test parameters.

Observational estimates of microstructure density generally vary between $10^3 \leq n \leq 10^5$ cm^{-3},

with some indications of even higher densities. We have explored the model chemistry for this density range, and have made some additional calculations for the higher densities suggested by the formaldehyde observations of Moore & Marscher (1995). Slab ages of 1–1000 yr are considered. Radiation strengths and cosmic-ray ionization rates of $\frac{1}{3}$, 1 and 3 times the standard interstellar values (1 Habing and 1.3×10^{-17} s^{-1}, respectively) are also considered.

6.1.3 Model results

The purpose of our study is to investigate whether there exists a parameter space of densities, radiation fields, cosmic-ray ionization rates and dimensions where molecules can be formed in the variable components, and also to determine the time-dependent nature of such structures. In the next two subsections we make predictions, based on our models, of the physical conditions and time-dependence of the microstructure, respectively.

In all the results reported here, we have assumed an elongation factor of 10; i.e. the path-length along the line of sight through the microstructure is 10× the transverse depth, 10 AU.

Physical characteristics of the microstructure

The results of our chemical model suggest that only a few molecular species are formed in large enough quantities in the proposed scenario to be potentially detectable. They include CH, CH_2, CO, C_2 and OH. In our model, these species are only produced in great enough quantities to be detectable under certain physical conditions (see Tables 6.2 and 6.3, and Figures 6.2 and 6.3). In Table 6.2 we list the column densities of CO, CH, C_2 and OH as a function of density and time at a transverse depth of 10 AU into the microstructure slab, corresponding to a transverse visual extinction of approximately 10^{-4} to 10^{-2} mag for number densities in the range 10^3 to 10^5 cm^{-3}, making the assumption that the elongation factor along the line of sight (described above) is 10. Column densities larger than 10^{11} cm^{-2} are shown in bold in Table 6.2, indicating a reasonable lower limit for molecular species that are potentially detectable. Assuming that the microstructure has a transverse spatial dimension of 10 AU, a minimum density of 10^4 cm^{-3} is necessary for most species to be detectable. Table 6.3 lists the column densities for Ca I and Ca II. Since atoms have stronger oscillator strengths than molecules, these species are detectable at lower column densities than the limit of 10^{11} cm^{-2} imposed in Table 6.2. Figures 6.2 and 6.3 show how the column densities of CO and CH behave as a function of density, time and radiation field. We find that CO is particularly sensitive to variations in the number density, and its column density can vary by over 2 orders of magnitude in the number density range considered here. Its sensitivity to the

Table 6.2: Column densities (cm^{-2}) for molecular species along the line of sight within a microstructure of transverse depth 10 AU and elongation factor 10 along the line of sight. The region is subject to standard interstellar radiation and particle fields of 1 Habing (1.6×10^{-3} erg cm^{-2} s^{-1}) and $\zeta = 1.3 \times 10^{-17}$ s^{-1}. Values in bold indicate potentially detectable abundances (with column densities $> 10^{11}$ cm^{-2}).

Species	Time	Density (cm^{-3})				
	(yr)	10^3	5×10^3	10^4	5×10^4	10^5
CO	1	2.11×10^6	1.22×10^8	3.04×10^{10}	$\mathbf{1.20 \times 10^{11}}$	$\mathbf{2.31 \times 10^{11}}$
CO	5	2.03×10^7	7.89×10^{10}	$\mathbf{1.42 \times 10^{11}}$	$\mathbf{3.35 \times 10^{11}}$	$\mathbf{1.26 \times 10^{12}}$
CO	10	4.72×10^7	8.52×10^{10}	$\mathbf{1.57 \times 10^{11}}$	$\mathbf{6.86 \times 10^{11}}$	$\mathbf{2.56 \times 10^{12}}$
CO	50	4.32×10^8	9.93×10^{10}	$\mathbf{2.87 \times 10^{11}}$	$\mathbf{2.87 \times 10^{12}}$	$\mathbf{1.15 \times 10^{13}}$
CO	100	9.54×10^8	3.31×10^{10}	$\mathbf{2.62 \times 10^{11}}$	$\mathbf{5.00 \times 10^{12}}$	$\mathbf{2.04 \times 10^{13}}$
CH	1	7.51×10^8	1.35×10^{10}	$\mathbf{3.74 \times 10^{11}}$	$\mathbf{6.49 \times 10^{11}}$	$\mathbf{1.14 \times 10^{12}}$
CH	5	1.84×10^9	$\mathbf{2.28 \times 10^{11}}$	$\mathbf{4.46 \times 10^{11}}$	$\mathbf{4.79 \times 10^{11}}$	$\mathbf{1.13 \times 10^{12}}$
CH	10	2.12×10^9	$\mathbf{1.37 \times 10^{11}}$	$\mathbf{3.06 \times 10^{11}}$	$\mathbf{4.52 \times 10^{11}}$	$\mathbf{1.02 \times 10^{12}}$
CH	50	2.84×10^9	2.87×10^{10}	$\mathbf{1.18 \times 10^{11}}$	$\mathbf{3.24 \times 10^{11}}$	$\mathbf{7.35 \times 10^{11}}$
CH	100	2.82×10^9	1.51×10^{10}	5.81×10^{10}	$\mathbf{2.77 \times 10^{11}}$	$\mathbf{6.04 \times 10^{11}}$
C_2	1	2.20×10^5	3.05×10^7	1.71×10^9	1.86×10^{10}	7.97×10^{10}
C_2	5	4.32×10^6	4.89×10^9	1.11×10^{10}	8.77×10^{10}	$\mathbf{4.71 \times 10^{11}}$
C_2	10	1.07×10^7	5.76×10^9	1.49×10^{10}	$\mathbf{1.79 \times 10^{11}}$	$\mathbf{8.78 \times 10^{11}}$
C_2	50	8.52×10^7	7.36×10^9	3.64×10^{10}	$\mathbf{5.50 \times 10^{11}}$	$\mathbf{1.77 \times 10^{12}}$
C_2	100	1.66×10^8	5.07×10^9	4.01×10^{10}	$\mathbf{6.09 \times 10^{11}}$	$\mathbf{1.47 \times 10^{12}}$
OH	1	3.23×10^7	4.92×10^8	$\mathbf{9.81 \times 10^{11}}$	$\mathbf{6.58 \times 10^{11}}$	$\mathbf{2.85 \times 10^{11}}$
OH	5	1.56×10^8	$\mathbf{8.13 \times 10^{11}}$	$\mathbf{1.05 \times 10^{12}}$	$\mathbf{2.96 \times 10^{11}}$	$\mathbf{4.10 \times 10^{11}}$
OH	10	3.01×10^8	$\mathbf{4.97 \times 10^{11}}$	$\mathbf{6.58 \times 10^{11}}$	$\mathbf{2.95 \times 10^{11}}$	$\mathbf{3.28 \times 10^{11}}$
OH	50	1.43×10^9	$\mathbf{1.25 \times 10^{11}}$	$\mathbf{2.66 \times 10^{11}}$	$\mathbf{1.72 \times 10^{11}}$	$\mathbf{2.42 \times 10^{11}}$
OH	100	1.98×10^9	1.51×10^{10}	9.12×10^{10}	$\mathbf{1.44 \times 10^{11}}$	$\mathbf{2.42 \times 10^{11}}$

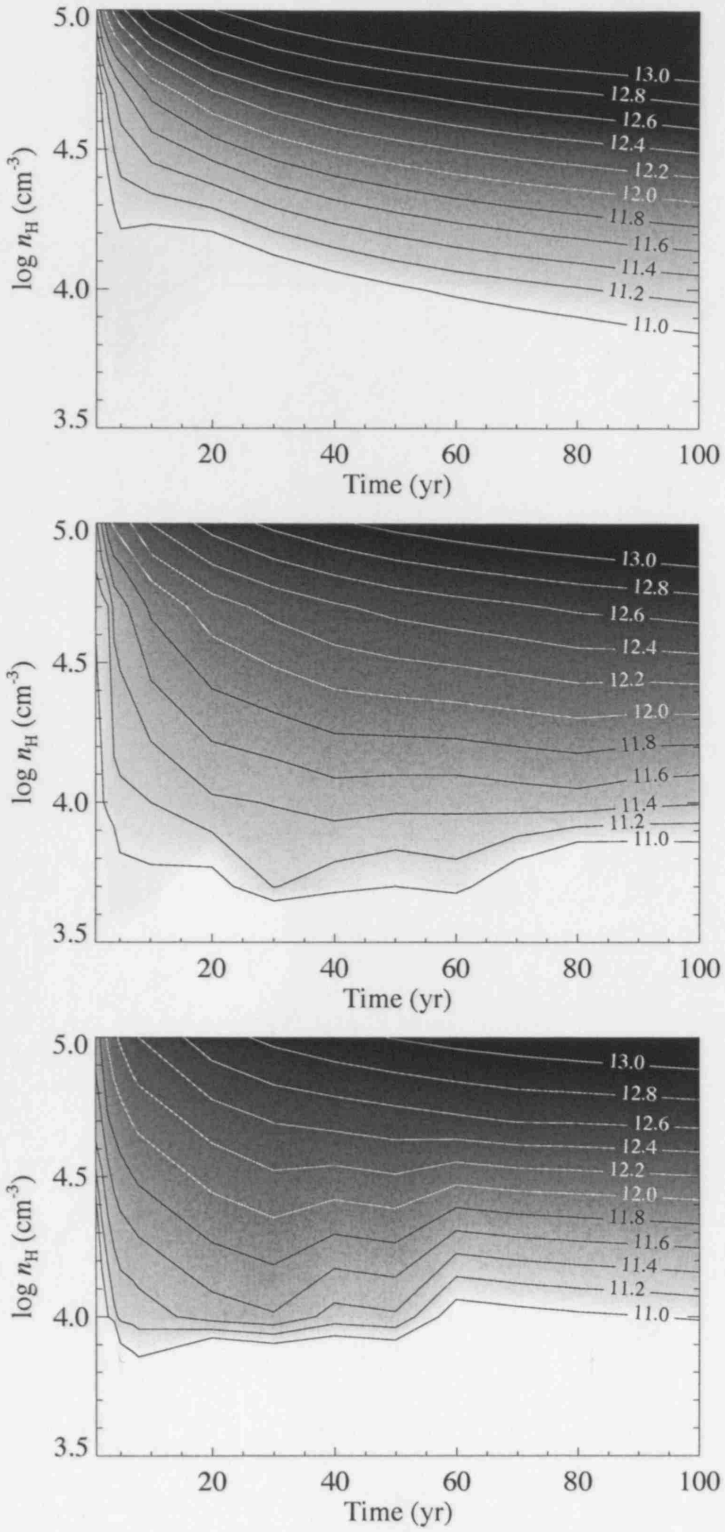

Figure 6.2: Contours of log CO column density as a function of density and time for a microstructure of transverse depth 10 AU, elongated by a factor of 10 along the line of sight, and a cosmic-ray ionization rate of $\zeta = 1.3 \times 10^{-17}$ s^{-1}. From top to bottom, the three figures are for incident radiation field strengths of $\frac{1}{3}$, 1 and 3 Habing, respectively.

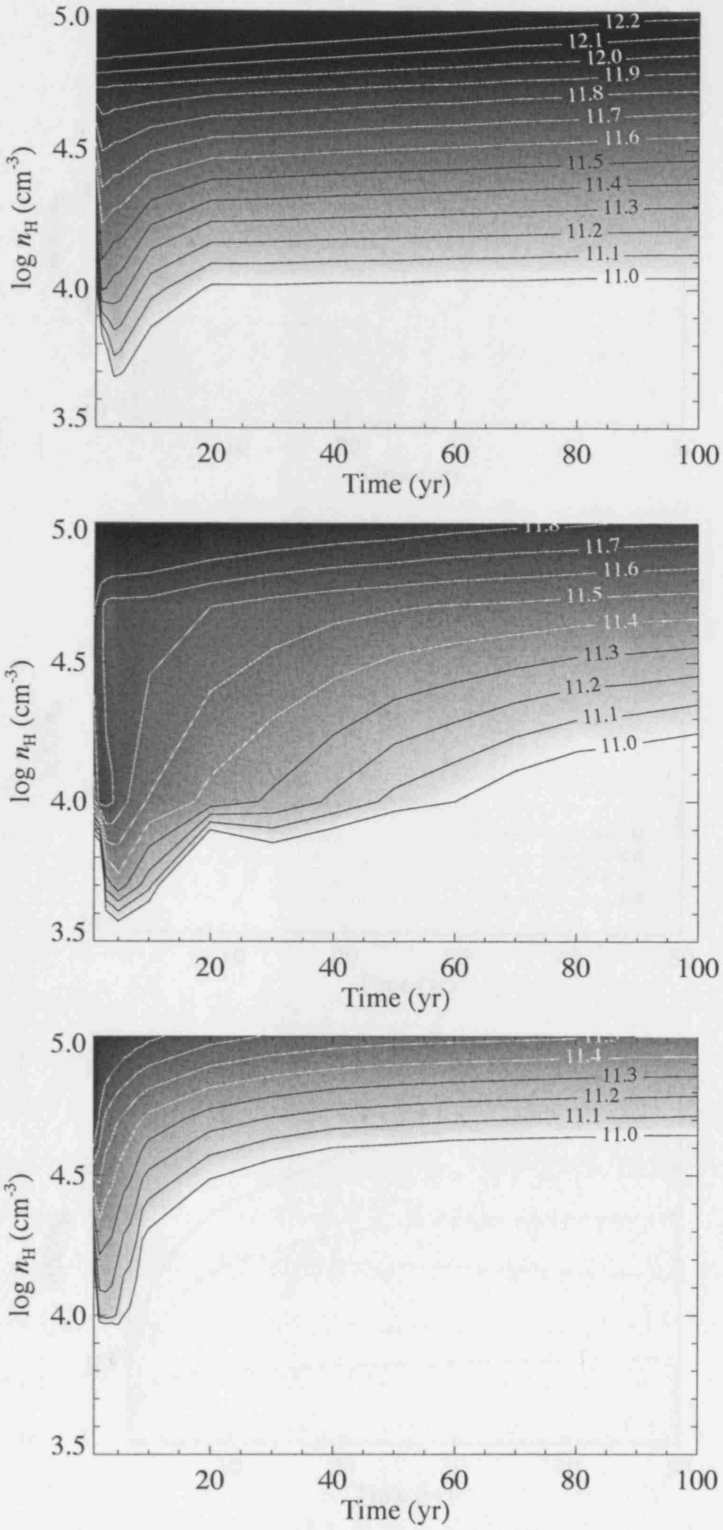

Figure 6.3: Contours of log CH column density as a function of density and time for a microstructure of transverse depth 10 AU, elongated by a factor of 10 along the line of sight, and a cosmic-ray ionization rate of $\zeta = 1.3 \times 10^{-17}$ s^{-1}. From top to bottom, the three figures are for incident radiation field strengths of $\frac{1}{3}$, 1 and 3 Habing, respectively.

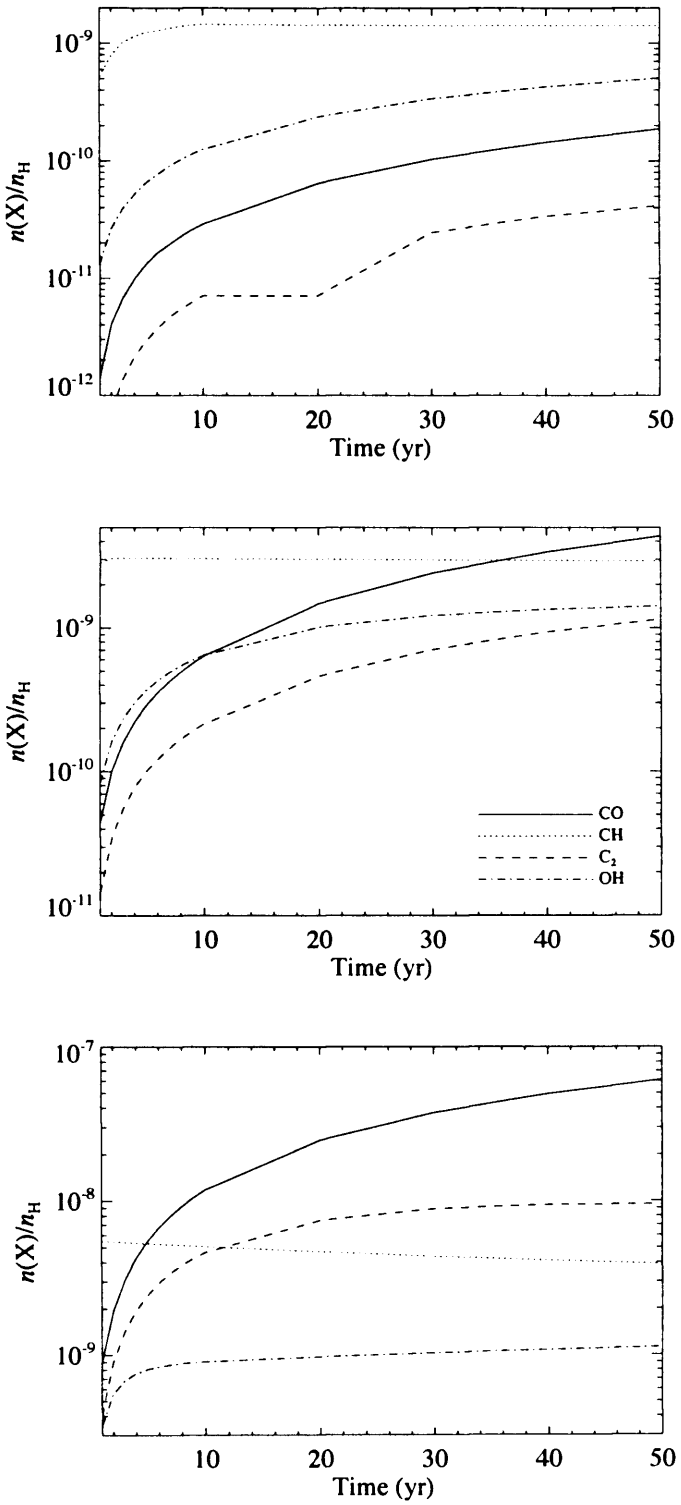

Figure 6.4: Fractional abundances of CO (solid line), CH (dotted), C_2 (dashed) and OH (dash-dot) at a transverse visual extinction of $A_{V,\mathrm{trans}} = 10^{-4}$ mag into the microstructure, subject to an incident radiation field strength of 1 Habing and a cosmic-ray ionization rate of $\zeta = 1.3 \times 10^{-17}$ s^{-1}. From top to bottom, the three figures are for microstructure densities of 10^3, 10^4 and 10^5 cm^{-3}, respectively.

Table 6.3: Column densities (cm^{-2}) for neutral and singly ionized calcium along the line of sight within a microstructure of transverse depth 10 AU and elongation factor 10 along the line of sight. The region is subject to standard interstellar radiation and particle fields.

Species	Time	Density (cm^{-3})				
	(yr)	10^3	5×10^3	10^4	5×10^4	10^5
Ca I	1	5.62×10^4	1.90×10^6	7.49×10^6	1.80×10^8	6.41×10^8
Ca I	5	2.75×10^5	9.28×10^6	3.63×10^7	8.20×10^8	2.73×10^9
Ca I	10	5.39×10^5	1.81×10^7	6.98×10^7	1.46×10^9	4.43×10^9
Ca I	50	2.36×10^6	7.38×10^7	2.64×10^8	3.19×10^9	6.26×10^9
Ca I	100	4.00×10^6	1.17×10^8	3.82×10^8	3.12×10^9	5.13×10^9
Ca II	1	1.10×10^9	4.30×10^9	1.02×10^{10}	5.50×10^{10}	1.13×10^{11}
Ca II	5	1.10×10^9	4.30×10^9	1.02×10^{10}	5.44×10^{10}	1.11×10^{11}
Ca II	10	1.17×10^9	4.82×10^9	9.39×10^9	5.38×10^{10}	1.01×10^{11}
Ca II	50	1.16×10^9	4.76×10^9	9.20×10^9	5.19×10^{10}	9.95×10^{10}
Ca II	100	1.16×10^9	4.72×10^9	9.08×10^9	5.17×10^{10}	1.01×10^{11}

radiation field is more subtle: at early times (< 20 yr) and low densities ($< 10^4$ cm^{-3}), a weak radiation field (< 1 Habing) yields a longer timescale (~ 100 yr) for the production of detectable CO. CH, on the other hand, shows a strong sensitivity to the radiation field employed. In fact, if the field is stronger than 1 Habing, CH can only remain detectable at high densities ($> 5 \times 10^4$ cm^{-3}). In general, CH is formed and then destroyed very quickly. These trends restrict the parameter space for which both CO and CH can be present in the microstructure *at the same time*. None of the species seem to have a strong dependence on the rate of cosmic-ray ionization employed.

The most remarkable result is that, even at the earliest times shown, if the number density is sufficiently high then potentially detectable column densities of the species listed above are attained. Thus, the high density drives a chemistry fast enough to overcome the losses due to the strong radiation field. Since the transverse visual extinctions considered are close to zero, the region is essentially unshielded. Note, e.g., that the total extinction along the line of sight toward κ Vel observed by Crawford (2002) is small [$E(B-V) = 0.11$] and that the transverse extinction at the variable component must be significantly less than this. By assuming that the transverse extinction is close to zero, we are therefore estimating the lower limit of the additional contribution to column

densities from species generated in the microstructure.

The adopted column density of H_2 is, however, sufficiently large to ensure that the H_2 photodissociation rate is too slow to cause significant loss of H_2 on the timescales considered here.

The fact that high densities are necessary in order to produce sufficiently large molecular abundances in the microstructure is consistent with the conclusions of Moore & Marscher (1995) who find that, if the molecular variability is indeed due to density structure, the number densities need to be at least 10^6 cm^{-3}. In fact, Marscher et al. (1993) and Moore & Marscher (1995) detect both H_2CO and OH in their time variability study. In our study, OH is present as long as the density is $> 5 \times 10^3$ cm^{-3} and does indeed show time variability (see Table 6.2). H_2CO, however, never reaches a high enough abundance to be detectable for the number densities considered here. In order to see whether densities as high as the ones considered by Moore & Marscher (1995) could produce significant amounts of H_2CO, we ran two more models at 10^6 and 10^7 cm^{-3} under standard interstellar conditions. We find that at 10^6 cm^{-3} H_2CO is only just barely close to the lower limit of detectability for times $\geq$ 500 yr, while at 10^7 cm^{-3}, H_2CO becomes detectable after only 50 yr. These models further support the Moore & Marscher (1995) findings.

Time-dependence of the chemistry

Tables 6.2 and 6.3, and Figure 6.4 show how the different species behave as a function of time. We now briefly discuss the time variability of each species for number densities $\geq 10^4$ cm^{-3}. CO takes ~5–10 yr to form in significant amounts, and its abundance increases steadily with time. For CO to be abundant, therefore, the microstructure would need to exist for at least 10 yr. CH, on the other hand, forms in less than 1 yr, but is subsequently destroyed (in part to form CO) within the first 100 yr. C_2 takes over 10 yr to form in detectable quantities, then survives in the gas for at least 300 yr, although its abundance starts to decline. OH behaves in a similar manner to CH in that it forms within 1 yr but starts being converted into other species almost immediately and by 500 yr its abundance is too low to be detectable. Ca II is present, confirming the detection of Crawford (2002) at the velocity of the microstructure. However, it cannot be used as a diagnostic test of the microstructure age because its abundance is invariant. Ca I, on the other hand, shows considerable time variability, though whether the variations are large enough to be detectable is less certain. Of course, these variations are not reflected in the column densities of Ca II, since its abundance is several orders of magnitude higher. The CO column density under appropriate parameter choices generally exceeds those of other molecular species. Thus, for a number density of 10^4 cm^{-3}, by 100 yr the CO column density has built up to 2.6×10^{11} cm^{-2}, while those for

CH and C_2 are 5.8×10^{10} and 4.0×10^{10} cm^{-2} respectively. Although the amounts by which CH, OH, C_2, etc. decline with time are very small and may therefore seem insignificant, they are indeed real and consistent with the gas phase chemistry that is taking place. The behaviour described above is expected for the usual gas phase chemical networks: CO and C_2 column densities increase monotonically over the time span considered here. A feed molecule for the networks producing CO and C_2 is CH, and its column density declines slightly over this period, showing that CH is being converted into other species; no significant loss of CH by photodissociation occurs in the time interval explored here.

In summary, for CO and C_2 to form, the microstructure needs to survive at least 10 yr. On the other hand, it cannot be much older than $\sim$ 50 yr if CH is indeed observed.

Unfortunately, detection of CO by absorption in its resonance line requires a UV spectrometer in an orbital observatory; none is currently available. However, CH and C_2 are detectable from the ground. It appears from this work that these molecules should have comparable abundances in transient microstructure of number density $\sim 10^4$ cm^{-3}.

6.1.4 Comparisons with observations and conclusions

This study was prompted in part by the molecular detection obtained by Crawford (2002) at the velocity (different to that of the surrounding medium) of previously reported microstructure in the line of sight toward κ Vel. Hence we now briefly compare our models with such observations. In Table 2 of Crawford (2002), the observed column densities of Ca I, Ca II (two velocity components) and CH are listed as, respectively, 3.2×10^9, 2.0×10^{11} and 6.2×10^{10}, 2.7×10^{11} cm^{-2}. If we assume an elongation factor of 10 along the line of sight and a gas density of the order of $\sim 10^5$ cm^{-3}, the observed CH column density can be easily reached at very early times ($\sim$ 10 yr) and maintained. If instead the density of the microstructure is closer to 10^4 cm^{-3} then we infer a maximum age for the microstructure of about 50 yr, after which most CH would be destroyed. Hence observations of CH indicate that such filamentary or sheet-like structures are likely to be younger than 50 yr. The observed Ca I and Ca II column densities can be produced in the model if the microstructure has a number density of $\sim 5 \times 10^4$ cm^{-3} and is older than 10 yr (see Table 6.3).

In order to further test the predicted molecular abundances, we compare them to high-resolution data obtained in a search for interstellar C_2 at the velocity of the variable component toward κ Vel using the Ultra-High-Resolution Facility (UHRF; Diego et al. 1995) at the Anglo-Australian Telescope (AAT). The final continuum signal-to-noise ratio was 480, but the Q(4) line was not detected. The resulting 3σ upper limit to the equivalent width of the Q(4) line was 0.09 mÅ,

yielding an upper limit to the $J = 4$ column density of $N(J = 4) \leq 1.95 \times 10^{11}$ cm^{-2} (using the oscillator strength adopted by Crawford 1997). At the high densities ($n = 10^3$–10^5 cm^{-3}) expected for these variable components, the rotational populations will be approximately thermal, and for $T \sim 100$ K we expect the total C_2 column density to be $N(C_2) \sim 4 \times N(J = 4)$ (e.g. van Dishoeck 1984). Therefore, these observations imply $N(C_2) \lesssim 10^{12}$ cm^{-2} in the variable interstellar component toward κ Vel. This is consistent with the model results given in Table 6.2 for $N_H \lesssim 10^5$ cm^{-3}. More sensitive searches for C_2 would appear to be worthwhile, as these would be able to constrain the model results at lower densities.

The best matching models for observations at the velocity of the variable component in the κ Vel line of sight seem therefore to be those for a young ($\sim$ 50 yr), transient ($<$ 100 yr), high density ($> 10^4$ cm^{-3}), small ($\sim$ 10 AU), slightly elongated (by about a factor of 10 along the line of sight) structure, immersed in an ambient radiation field.

The main result of this work is that essentially unshielded interstellar gas can develop detectable column densities of molecules on very short time-scales ($<$ 100 yr) for path-lengths on the order of 100 AU along the line of sight, if the density is $\sim 10^4$ cm^{-3} or higher. This time and density domain is a region of parameter space not previously explored. The calculations presented here are pseudo time-dependent, in that the slab structure is fixed. If the cause of such microstructure is indeed magnetohydrodynamic, then the filamentary objects likely to be responsible for the effects observed toward κ Vel and elsewhere are probably waves moving at magnetosonic sound speed.

6.2 Starburst models: An expanding supershell around a massive star cluster

The work presented in this section is based on the paper by Yao et al. (2006).

6.2.1 Introduction

The starburst phenomenon is a period of vigorous and unsustainable star formation, now believed to be commonplace in galaxies throughout the Universe (Madau et al. 1998). These bursts of massive star formation are known to inject large amounts of energy and material into the surrounding ISM through strong stellar winds and repeated supernova explosions. Such activity can have a dramatic effect on the host galaxy, significantly altering its structure and evolution, and may be responsible for much of the warm gas distribution within it. Understanding the properties of starbursts and their complex interaction with the surrounding ISM is therefore crucial to our understanding of galaxy

evolution as a whole.

Models have been able to infer the physical conditions of the gas and dust within starburst regions by comparison with emission line observations at far-infrared to millimetre wavelengths (e.g. Wild et al. 1992; Seaquist & Frayer 2000). However, none have been able to relate the observed emission line properties of the neutral gas to the age or star formation history of the starburst. In this work, a time-dependent model of an evolving starburst is developed to predict the FIR/submm/mm line emission of the gas, in the hope of achieving this goal. The model considers the expansion of a hot bubble of ionized gas around a young massive star cluster at the centre of a giant molecular cloud (GMC). During the expansion of this bubble, a thin, dense shell of swept-up interstellar gas is formed around it, with a PDR at the inner surface (see Figure 6.5). The model describes the dynamical evolution of this bubble/shell structure, the changing chemistry and temperature within the dense shell and the resulting emission lines of selected atomic and molecular species.

In the remainder of this section, the role of the UCL_PDR code in this work is described, the results of the swept-up shell model are briefly discussed and the gas temperatures and chemical abundances produced by the UCL_PDR code are presented. The subsequent use of a spherically symmetric, non-LTE radiative transfer code (SMMOL, Rawlings & Yates 2001) to calculate emission line intensities from the gas temperatures and abundances produced by the UCL_PDR code was carried out by others and so will not be discussed here, except when drawing conclusions about the project as a whole.

6.2.2 PDR model of an expanding shell

The FUV radiation from the central massive star cluster illuminates the inner surface of the swept-up shell, creating a PDR that is responsible for much of the FIR/submm/mm radiation from the region. The UCL_PDR code is used to calculate the gas temperature and chemical abundances within the shell as a function of depth and time, treating the shell as a semi-infinite slab of constant density and the incident FUV field as unidirectional and normal to the inner surface. The cooling within the PDR is therefore calculated assuming that emission only escapes from the inner surface of the shell, since it is assumed to be infinitely thick in the outward direction. Heating due to shocks is not included in the code, but the cosmic-ray ionization rate ζ is enhanced by a factor of 1.5 at later times ($t > 10$ Myr) to simulate the additional heating due to soft X-rays from the central star cluster. The main characteristics of the code are as described in Chapter 2, however, it has been subsequently modified to accept as an input the time-dependent FUV flux and shell density, determined by the methods outlined below.

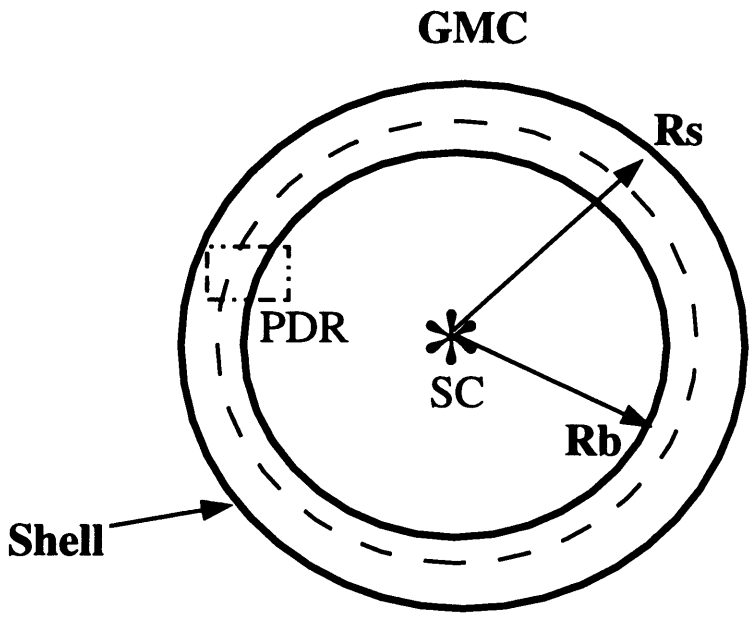

Figure 6.5: Schematic structure of an evolving GMC centrally illuminated by a compact young star cluster. R_s is the radius of the shell and R_b is the radius of the bubble. The PDR lies between the thin, dense swept-up shell and the ionized bubble interior. *Source: Yao et al. (2006).*

The total FUV flux generated by the central massive star cluster is calculated by integrating the flux density of the stellar population spectrum over the wavelength range 912 Å $< \lambda <$ 2400 Å at each time-step using STARBURST99, a time-dependent stellar population synthesis model developed by Leitherer et al. (1999). The details of the instantaneous burst model of star formation used to generate the time-dependent stellar population spectrum are not discussed here, since only the output of this model is used in connection with the UCL_PDR code. The FUV field strength G_0 (in units of the Habing field) that is incident on the inner surface of the shell is then given by:

$$G_0(t) = \frac{1}{(1.6 \times 10^{-3})} \frac{\int F_\nu(t) d\nu}{4\pi r_s^2(t)} \quad \text{[Habing]}, \tag{6.1}$$

where F_ν is the flux density of the stellar population spectrum and r_s is the radius of the shell, recalling that the Habing (1968) field is defined as having a flux of 1.6×10^{-3} erg s^{-1} cm^{-2} in the corresponding wavelength range.

The radius r_s and expansion velocity v_s of the shell are determined as a function of time from a standard dynamical model of the bubble/shell structure (see, e.g., Castor et al. 1975; Weaver et al. 1977; McCray & Kafatos 1987; Franco et al. 1990) and the shell is assumed to be supported by

thermal and microturbulent pressure. The gas temperature drops toward the outer surface of the shell as the FUV radiation incident on the inner surface is attenuated by the dust within it. Since the gas density n_s is assumed to be constant across the shell, the pressure is therefore lower at the outer surface. If the shell is also assumed to be in pressure equilibrium with the ambient ISM, its density can be determined by balancing the pressure at its outer surface with the ram pressure,

$$n_s(t) = \frac{n_a v_s^2(t)}{kT_s(t)/\mu + v_{turb}^2} \qquad [cm^{-3}], \tag{6.2}$$

where n_a is the ambient molecular gas density, T_s is the gas temperature at the outer surface of the shell, μ is the mean molecular weight, $\mu = 0.62\, m_H$, with m_H being the mass of the hydrogen atom, and v_{turb} is the turbulent velocity inside the shell. The thickness of the shell d_s (i.e., the distance between R_b and R_s in Figure 6.5) is determined at each time-step using the continuity equation (or mass conservation law),

$$d_s(t) = \frac{n_a r_s(t)}{3n_s(t)} \qquad [cm]. \tag{6.3}$$

The UCL_PDR code calculates the gas temperature in the shell by computing the chemistry and thermal balance self-consistently at each time- and depth-step, as described in Chapter 2. The temperature at the outer surface of the shell T_s is therefore determined by the code, based on the shell density and thickness. However, the outer surface temperature also appears in equation (6.2), used to determine the shell density, which, in turn, is used to determine the shell thickness (equation (6.3)). The three properties are therefore linked and the code must be run iteratively to converge on a solution to all three, with a difference in pressure between the outer shell and the ambient gas of $\leq$10% being used as the convergence criterion.

Table 6.4 summarizes the parameters used by the dynamical model, the STARBURST99 code and the UCL_PDR code to calculate the various properties of the expanding shell. In addition, the modified version of the UCL_PDR code assumes that all hydrogen is initially in H_2 at all depth-steps, as is appropriate for the interior of a GMC, and that the initial abundances for all other species are those produced by a single-point dark cloud model. The input parameters for the dark cloud model are $n = 4 \times 10^5$ cm^{-3}, $T_{GMC} = 10$ K, $G_0 = 1$ Habing and $A_V = 30$ mag. At subsequent time-steps, the abundances of all species are determined by the UCL_PDR code itself. In the next section, the results of the swept-up shell model are briefly discussed and the gas temperatures and chemical abundances produced by the UCL_PDR model are presented.

Table 6.4: Summary of the starburst model parameters used by the various codes involved.

Parameter		Adopted Value
Giant molecular cloud mass	$M_{\rm GMC}$	$10^7\ M_\odot$
Average cloud density	$n_{\rm GMC}$	$300\ {\rm cm}^{-3}$
Cloud core density	$n_{\rm core}$	$2000\ {\rm cm}^{-3}$
Ambient ISM density	$n_{\rm ISM}$	$30\ {\rm cm}^{-3}$
Star formation efficiency	η	0.25
Stellar mass	$M_\star$	$0.1 \leq M_\star \leq 120\ M_\odot$
Initial mass function	$dN/dM_\star$	$\propto M_\star^{-2.35}$
Metallicity	Z/Z_{odot}	1.0
PDR shell density	$n_{\rm s}$	$10^3 \leq n_{\rm s} \leq 10^7\ {\rm cm}^{-3}$
Incident FUV flux	G_0	$10 \leq G_0 \leq 10^8$ Habing
Starburst age	t	$0 \leq t \leq 10^8$ yr
Cosmic-ray ionization rate	ζ	$1.3 \times 10^{-17}\ {\rm s}^{-1}$
Turbulent velocity	$v_{\rm turb}$	$1.5\ {\rm km\,s}^{-1}$

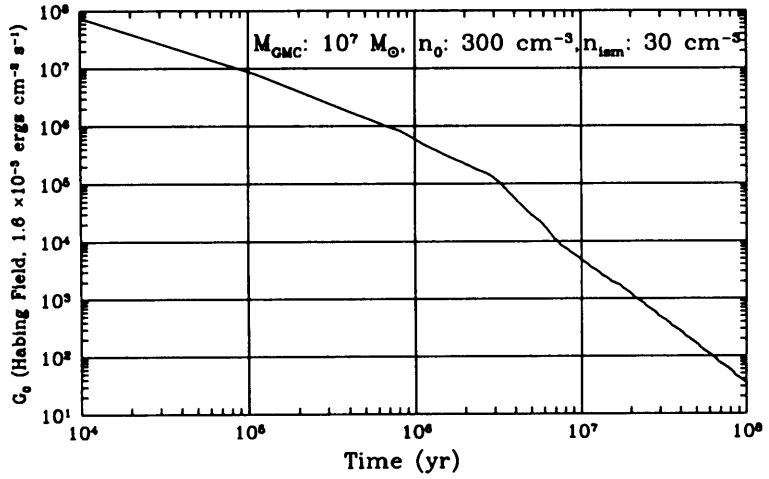

Figure 6.6: FUV radiation field strength G_0 (Habing) incident on the inner surface ($A_V = 0$) of the expanding shell as a function of time. *Source: Yao et al. (2006).*

6.2.3 Model results

Figure 6.6 shows the FUV radiation field strength G_0 incident on the inner surface of the shell, derived from the time-dependent stellar population synthesis data produced by the STARBURST99 code for an instantaneous burst of star formation (see Table 6.4 for details of the parameters used). The FUV field strength decreases from about 10^8 to 10^5 Habing over the first 4 Myr after the onset of star formation, by which time most of the massive O stars (>30 $M_\odot$) have terminated as supernovae. The field strength then decreases twice as fast to reach ~40 Habing at 100 Myr. Figure 6.7 shows the shell density n_s and thickness d_s as a function of time. The density and thickness of the shell are calculated using the dynamical model and the temperature structure determined by the UCL_PDR code, under the condition of pressure equilibrium between the outer surface of the shell and the ambient ISM, as discussed in the previous section. The shell density is seen to vary between 10^3 and 10^6 cm^{-3} over its evolution and the thickness of the shell changes from 10^{-3} to 10 pc over the course of the 100 Myr. Changes in the expansion velocity v_s and outer surface temperature T_s of the shell are relatively small during the H II expansion phase (during which time $n_a = n_{GMC}$, i.e. 300 cm^{-3}). This results in the fairly constant values of n_s and d_s seen at early times. The jump at $t \sim 2 \times 10^4$ yr marks the transition from the H II expansion phase to the stellar wind-dominated expansion phase. During the early period of this phase ($t < 0.8$ Myr), before the shell has swept up all the material in its parent GMC, the shell deceleration is compensated by the cooling in the shell to produce a second plateau in the shell density and thickness. After this period, the shell breaks free of the GMC and begins to expand into the more diffuse ISM ($n_a = n_{ISM}$, 30 cm^{-3}). The fall in ambient pressure causes the shell to expand and so become less dense (due to mass conservation). This relaxation of the shell continues through the snowplough phase of the expansion (for a full description of the various expansion phases, please see Yao et al. 2006).

Figures 6.8 and 6.9 show depth profiles for the temperatures and fractional abundances of the dominant species predicted by the UCL_PDR code for the expanding shell at several characteristic ages. The size of the shell changes with time and this is indicated by different maximum values of A_V in the various panels of both figures.

During the adiabatic expansion phase ($t < 7.5$ Myr), strong winds and supernova explosions compress the gas in the expanding shell, reaching densities $n_s > 10^4$ cm^{-3}, whilst the young and massive stars in the central cluster produce a strong FUV flux $G_0 > 10^4$ that heats the gas and dust within the shell to temperatures >1000 K (in the case of the gas; see the first 5 panels of Figure 6.8).

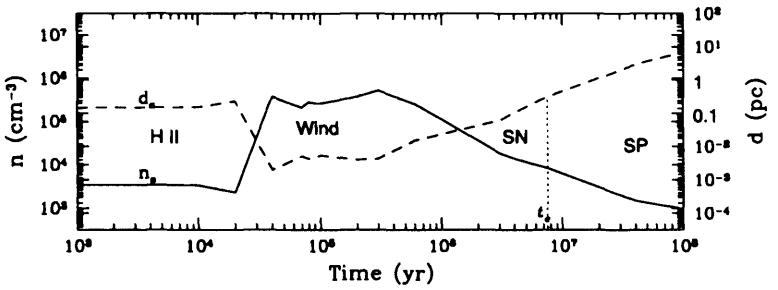

Figure 6.7: Shell density n_s (solid line) and thickness d_s (dashed line) as a function of time. The radiative cooling of the hot interior occurs at $t_c \approx 7.5$ Myr (dotted vertical line). *Source: Yao et al. (2006).*

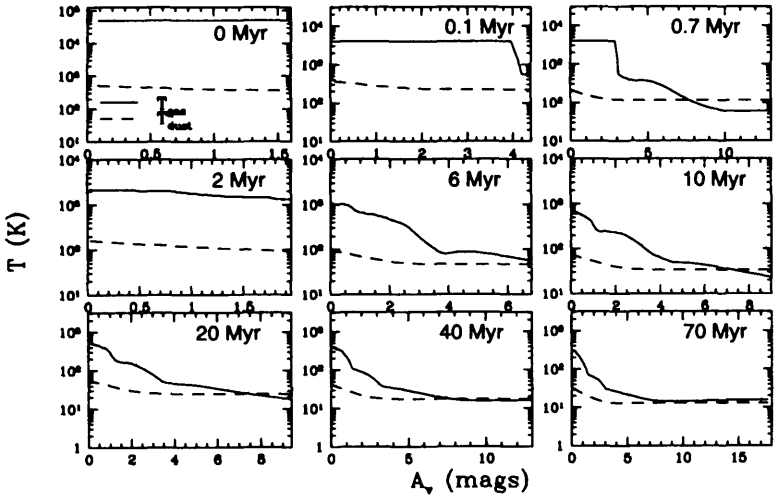

Figure 6.8: Time-dependent gas (solid line) and dust (dashed line) temperatures as a function of visual extinction A_V for the expanding shell. Note the different visual extinction ranges used in each panel. *Source: Yao et al. (2006).*

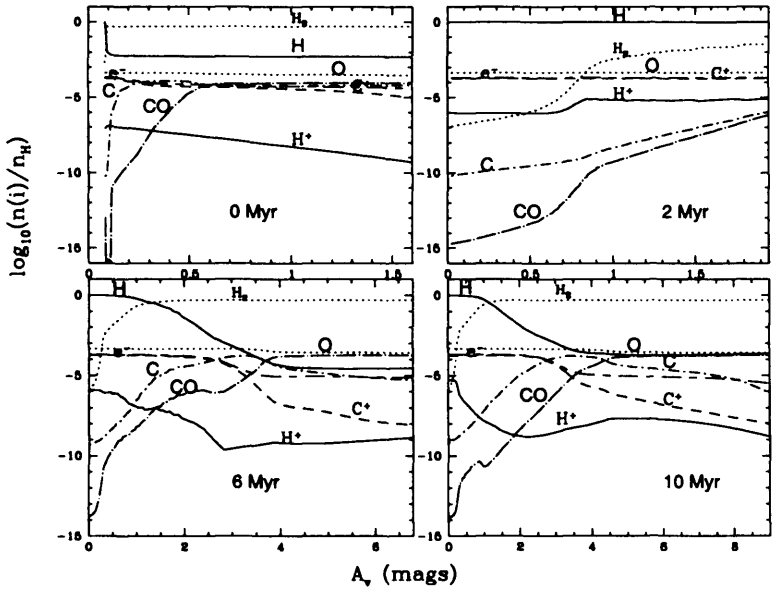

Figure 6.9: Time-dependent fractional abundances of the dominant species (H, H_2, H^+, C, C^+, O, CO and e^-), relative to total hydrogen nuclei, as a function of visual extinction A_V for the expanding shell. Note the different visual extinction ranges used in each panel. *Source: Yao et al. (2006).*

The initially molecular gas is quickly photodissociated at the onset of star formation, with most hydrogen in H and the bulk of carbon in C^+ at 2 Myr. However, the gas soon begins to return to molecular form, with H_2 abundances exceeding those of atomic H by ~6 Myr (see the bottom-left panel of Figure 6.9). At ~10 Myr, the shell has entered the snowplough, momentum-driven phase of expansion and the FUV field has dropped below 10^4 Habing, the shell density begins to decrease ($n_s < 10^4$ cm^{-3}) and the gas temperature in the shell falls to between 800 K at the inner surface and 20 K at the outer surface. By this time, the gas is mainly in molecular form again and the abundances of the dominant species show little variation at later times; the gas has effectively reached chemical equilibrium. As the shell continues to expand into the ambient ISM, the FUV field and the shell density both continue to decline and by 70 Myr the gas temperature is between 300 and 15 K.

6.2.4 Conclusions

A time-dependent model of the physical and chemical evolution of an expanding PDR shell surrounding a starburst region has been developed. The dynamical structure, FUV flux, shell density and thickness are all considered self-consistently and the evolving gas temperatures and

chemical abundances predicted by the UCL_PDR code have subsequently been used as the input to a radiative transfer code in order to produce model line ratios that can be compared to observations. As a result, the observed FIR/submm/mm emission properties of molecular and atomic gas in a starburst galaxy can be related to its age and star formation history.

My collaborators have then used the model to compare the predicted physical properties of the shell with observations of the expanding supershell centred around SNR 41.9+58 in the nearby starburst galaxy M 82. Very good agreement is found, implying that the expanding supershell is created by strong stellar winds and supernova explosions from a young star cluster at its centre. Predicted line ratios for various transitions of CO, HCN and HCO^+ agree with observations of the molecular gas in the central lobes of M 82 for a shell with an age of 3–7 Myr. However, atomic line ratios calculated by the model do not fit the observational data as well, with a best fit age much older than inferred from the molecular lines. This discrepancy is likely due to the fact that the atomic line emission is observed using a larger beam size and so covers a much larger region of the galaxy.

They have shown that the model also predicts values for the gas density and FUV field strength that are in agreement with other studies (e.g. Seaquist & Frayer 2000; Negishi et al. 2001) and molecular masses within the inner 600 pc that are compatible with previous observations (Wild et al. 1992). The model is now being developed further by L. Yao and collaborators to examine some of the parameters neglected in the current work in the hope of improving the fit. As it stands, the model highlights the important role time-dependent PDR codes can play in reproducing observed properties of dynamically evolving phenomena.

CHAPTER 7

CONCLUDING REMARKS AND PROPOSALS FOR FUTURE WORK

The work presented in this thesis describes the development of a time-dependent model of photon-dominated regions and its application to a variety of astrophysical problems. The model in question, the UCL_PDR code, has been described in Chapter 2, including the time-dependent capabilities it possesses, such as the ability to model structures whose density profiles vary with both time and cloud depth, or are subjected to time-varying radiation fields. The versatility of the code makes it a powerful and adaptable tool, which can be used to model many astrophysical phenomenon. Chapter 2 also discusses the participation of the UCL_PDR code in an international benchmarking effort, which highlighted the importance of reaching a consensus on the correct treatment of key physical and chemical processes and allowed previously undiscovered errors in the participating codes to be detected and resolved. As a result, the reliability of the UCL_PDR code has been established, at least in relation to other theoretical models, and the possible causes for disagreement between different codes have been identified.

The remaining chapters are devoted to the use of the UCL_PDR code to address several important issues in the study of the interstellar medium. The bulk of this work focuses on the difficulties that arise in trying to infer the distribution of molecular gas in galaxies. This stems from the unfortunate fact that molecular hydrogen, the most abundant molecule in space, is also one of the hardest to detect. In the face of this cosmic irony, alternative means must be found to determine the mass of molecular gas within distant regions. One such approach is the use of CO emission as a surrogate tracer of molecular gas. This technique has been commonplace for over twenty years, despite the fact that the CO-to-H_2 conversion factor, used to derive H_2 column density from observed CO(1–0)

line intensity, is known to vary. In Chapter 3, the variation of the CO-to-H_2 conversion factor, X_{CO}, has been considered in detail and its sensitivity to variation in physical parameters has been demonstrated. This study emphasises the importance of using values of X_{CO} that are appropriate to the environment being studied; the use of a canonical value for the conversion factor can lead to mass estimates that are an order of magnitude too high or too low under certain conditions. The value of X_{CO} is particularly sensitive to metallicity and cloud density, but also shows considerable variation in regions where the chemistry has not reached equilibrium.

Having firmly established the need for conversion factors that are appropriate to specific environments, such factors are provided in Chapter 4. A set of models have been constructed that represent the average interstellar conditions found within regular spiral galaxies, regions of starburst activity and low metallicity dwarf galaxies by fitting key emission line ratios observed in selected examples of these galaxy types. These best fit models have then been used to derive the appropriate values of X_{CO} for these environments. Furthermore, conversion factors have also been derived that allow molecular mass estimates to be inferred from higher transition lines of CO. It is hoped that these conversion factors can be used by observers to obtain more reliable mass estimates in the future.

Chapter 5 considers the possible existence of molecular gas under conditions that lead to little or no emission being detectable with current sensitivity limits. A large region of parameter space is found to exist that produces such conditions, characterised by low radiation field strengths, low metallicities and low levels of turbulence, These conditions may be found in the outer regions of galaxies and considerable quantities of hidden molecular gas might reside there, representing a reservoir of cold material for future star formation.

Finally, Chapter 6 discusses the application of the UCL_PDR code to two other problems. The first is the consideration of the chemistry that might arise in dense microstructure within the diffuse interstellar medium. It is found from this work that potentially observable column densities of certain molecular species might be present in small, dense microstructures. The second project attempts to model the time-dependent evolution of an expanding shell around a young massive star cluster. Predicted molecular line intensity ratios are found to be in good agreement with observations of the starburst galaxy M 82.

The overall conclusion that can be drawn from all of this work is that PDR codes, and in particular time-dependent PDR codes, can be used to model many interesting astrophysical phenomena and are capable of shedding light on their underlying properties. I feel that future work in this vein would prove very productive.

For instance, the success shown in fitting the observed line ratios in the centres of nearby galaxies (Chapter 4) suggests that more detailed considerations might yield further insight to the properties of the ISM within these objects. The high spatial resolutions achievable with the imminent arrival of the *Herschel* satellite and ALMA interferometer will allow external galaxies to be probed on much smaller scales and the properties of individual molecular clouds, rather than the average properties of large regions, will be able to be inferred.

Many more time-dependent problems spring to mind that could be modelled with the UCL_PDR code, three examples of which are evolving protoplanetary discs, expanding molecular envelopes within planetary nebulae and photoevaporating clumps in H II regions. Studying the time-dependent behaviour of such phenomena could prove to be interesting future projects and might help to solve some of the problems with current models.

Bibliography

Abel N. P., Ferland G. J., Shaw G., van Hoof P. A. M., 2005, ApJS, 161, 65

Abgrall H., Le Bourlot J., Pineau des Forêts G., Roueff E., Flower D. R., Heck L., 1992, A&A, 253, 525

Arimoto N., Sofue Y., Tsujimoto T., 1996, PASJ, 48, 275

Bakes E. L. O., Tielens A. G. G. M., 1994, ApJ, 427, 822

Bakes E. L. O., Tielens A. G. G. M., 1998, ApJ, 499, 258

Bates D. R., Spitzer L. J., 1951, ApJ, 113, 441

Bell T. A., Viti S., Williams D. A., Crawford I. A., Price R. J., 2005, MNRAS, 357, 961

Bell T. A., Roueff E., Viti S., Williams D. A., 2006a, MNRAS, 371, 1865

Bell T. A., Hartquist T. W., Viti S., Williams D. A., 2006b, A&A, in press

Belley J., Roy J.-R., 1992, ApJS, 78, 61

Bensch F., Leuenhagen U., Stutzki J., Schieder R., 2003, ApJ, 591, 1013

Bhat C. L., Mayer C. J., Wolfendale A. W., 1986, Phil. Trans. R. Soc. Lond., 319, 249

Black J. H., 1987, in Hollenbach D. J., Thronson H. A., eds, Interstellar Processes: Proceedings of the Symposium on Interstellar Processes, held in Grand Teton National Park, July 1986rocesses: proceedings of the symposium on interstellar processes, held in Grand Teton National Park, July 1986 Vol. 134 of Astrophysics and Space Science Library, Heating and cooling of the interstellar gas. Kluwer, Dordrecht, pp 731–744

Black J. H., Dalgarno A., 1976, ApJ, 203, 132

Black J. H., Dalgarno A., 1977, ApJS, 34, 405

Black J. H., van Dishoeck E. F., 1987, ApJ, 322, 412

Blades J. C., Sahu M. S., He L., Crawford I. A., Barlow M. J., Diego F., 1997, ApJ, 478, 648

Blitz L., Bloemen J. B. G. M., Hermsen W., Bania T. M., 1985, A&A, 143, 267

Bloemen H., 1989, ARA&A, 27, 469

Boger G. I., Sternberg A., 2005, ApJ, 632, 302

Bohlin R. C., Savage B. D., Drake J. F., 1978, ApJ, 224, 132

Bolatto A. D., Jackson J. M., Kraemer K. E., Zhang X., 2000, ApJ, 541, L17

Boselli A., Lequeux J., Gavazzi G., 2002a, A&A, 384, 33

Boselli A., Lequeux J., Gavazzi G., 2002b, Ap&SS, 281, 127

Brouillet N., Kaufman M., Combes F., Baudry A., Bash F., 1998, A&A, 333, 92

Brunt C. M., Heyer M. H., 2002, ApJ, 566, 289

Burke J. R., Hollenbach D. J., 1983, ApJ, 265, 223

Burton M. G., Hollenbach D. J., Tielens A. G. G. M., 1990, ApJ, 365, 620

Cardelli J. A., Clayton G. C., Mathis J. S., 1989, ApJ, 345, 245

Carruthers G. R., 1970, ApJ, 161, L81

Casoli F., Clausset F., Viallefond F., Combes F., Boulanger F., 1990, A&A, 233, 357

Castor J., McCray R., Weaver R., 1975, ApJ, 200, L107

Cecchi-Pestellini C., Dalgarno A., 2000, MNRAS, 313, L6

Cha A. N., Sembach K. R., 2000, ApJS, 126, 399

Cohen R. S., Dame T. M., Garay G., Montani J., Rubio M., Thaddeus P., 1988, ApJ, 331, L95

Colbert J. W., Malkan M. A., Clegg P. E., Cox P., Fischer J., Lord S. D., Luhman M., Satyapal S., Smith H. A., Spinoglio L., Stacey G., Unger S. J., 1999, ApJ, 511, 721

Combes F., 2000, in Combes F., Pineau des Forêts G., eds, Molecular Hydrogen in Space H_2 in Galaxies. Cambridge University Press, Cambridge, pp 275–283

Contursi A., Kaufman M. J., Helou G., Hollenbach D. J., Brauher J., Stacey G. J., Dale D. A., Malhotra S., Rubio M., Rubin R. H., Lord S. D., 2002, AJ, 124, 751

Crawford I. A., 1997, MNRAS, 290, 41

Crawford I. A., 2002, MNRAS, 334, L33

Crawford I. A., Howarth I. D., Ryder S. D., Stathakis R. A., 2000, MNRAS, 319, L1

Dahmen G., Hüttemeister S., Wilson T. L., Mauersberger R., 1998, A&A, 331, 959

Dalgarno A., McCray R. A., 1972, ARA&A, 10, 375

Dalgarno A., McCray R. A., 1973, ApJ, 181, 95

Dame T. M., Hartmann D., Thaddeus P., 2001, ApJ, 547, 792

Danks A. C., Sembach K. R., 1995, AJ, 109, 2627

Danks A. C., Walborn N. R., Vieira G., Landsman W. B., Gales J., García B., 2001, ApJ, 547, L155

Davis R. J., Diamond P. J., Goss W. M., 1996, MNRAS, 283, 1105

de Jong T., 1972, A&A, 20, 263

de Jong T., 1977, A&A, 55, 137

de Jong T., Dalgarno A., Boland W., 1980, A&A, 91, 68

de Vaucouleurs G., de Vaucouleurs A., Corwin J., Buta R. J., Paturel G., Fouque P., 1991, Third Reference Catalogue of Bright Galaxies. Vol. 1–3, Springer-Verlag, New York

Diamond P. J., Goss W. M., Romney J. D., Booth R. S., Kalberla P. M. W., Mebold U., 1989, ApJ, 347, 302

Dickman R. L., 1978, ApJS, 37, 407

Dickman R. L., Snell R. L., Schloerb F. P., 1986, ApJ, 309, 326

Diego F., Fish A. C., Barlow M. J., Crawford I. A., Spyromilio J., Dryburgh M., Brooks D., Howarth I. D., Walker D. D., 1995, MNRAS, 272, 323

Dieter N. H., Welch W. J., Romney J. D., 1976, ApJ, 206, L113

Digel S., Bally J., Thaddeus P., 1990, ApJ, 357, L29

Douglas A. E., Herzberg G., 1941, ApJ, 94, 381

Draine B. T., 1978, ApJS, 36, 595

Draine B. T., Bertoldi F., 1996, ApJ, 468, 269

Draine B. T., Lee H. M., 1984, ApJ, 285, 89

Dufour R. J., 1984, in van den Bergh S., de Boer K. S., eds, Proc. IAU Symp. 108, Structure and Evolution of the Magellanic Clouds The composition of H II regions in the Magellanic Clouds. Kluwer, Dordrecht, pp 353–360

Dumke M., Nieten C., Thuma G., Wielebinski R., Walsh W., 2001, A&A, 373, 853

Dyson J. E., Williams D. A., 1997, The Physics of the Interstellar Medium, 2nd edn. Institute of Physics Publishing, Bristol

Ellison S. L., Yan L., Hook I. M., Pettini M., Wall J. V., Shaver P., 2001, A&A, 379, 393

Engelbracht C. W., Rieke M. J., Rieke G. H., Latter W. B., 1996, ApJ, 467, 227

Falgarone E., Puget J.-L., Perault M., 1992, A&A, 257, 715

Federman S. R., Glassgold A. E., Kwan J., 1979, ApJ, 227, 466

Ferland G. J., Korista K. T., Verner D. A., Ferguson J. W., Kingdon J. B., Verner E. M., 1998, PASP, 110, 761

Field G. B., Somerville W. B., Dressler K., 1966, ARA&A, 4, 207

Fitzpatrick E. L., 1999, PASP, 111, 63

Flannery B. P., Roberge W., Rybicki G. B., 1980, ApJ, 236, 598

Flower D. R., Launay J. M., 1985, MNRAS, 214, 271

Flower D. R., Le Bourlot J., Pineau des Forêts G., Roueff E., 1994, A&A, 282, 225

Frail D. A., Weisberg J. M., Cordes J. M., Mathers C., 1994, ApJ, 436, 144

Franco J., Tenorio-Tagle G., Bodenheimer P., 1990, ApJ, 349, 126

Frerking M. A., Langer W. D., Wilson R. W., 1982, ApJ, 262, 590

Fuente A., García-Burillo S., Gerin M., Teyssier D., Usero A., Rizzo J. R., de Vicente P., 2005, ApJ, 619, L155

Fuente A., García-Burillo S., Gerin M., Rizzo J. R., Usero A., Teyssier D., Roueff E., Le Bourlot J., 2006, ApJ, 641, L105

García-Burillo S., Guélin M., Cernicharo J., 1993, A&A, 274, 123

García-Burillo S., Martín-Pintado J., Fuente A., Neri R., 2001, ApJ, 563, L27

Gardiner L. T., Noguchi M., 1996, MNRAS, 278, 191

Garnett D. R., Shields G. A., Peimbert M., Torres-Peimbert S., Skillman E. D., Dufour R. J., Terlevich E., Terlevich R. J., 1999, ApJ, 513, 168

Gerin M., Phillips T. G., 2000, ApJ, 537, 644

Giovanelli R., Haynes M. P., Kent B. R., Perillat P., Saintonge A., Brosch N., Catinella B., Hoffman G. L., Stierwalt S., Spekkens K., Lerner M. S., Masters K. L., Momjian E., Rosenberg J. L., Springob C. M., 2005, AJ, 130, 2598

Glassgold A. E., Langer W. D., 1974, ApJ, 193, 73

Glassgold A. E., Langer W. D., 1975, ApJ, 197, 347

Gould R. J., Salpeter E. E., 1963, ApJ, 138, 393

Green S., Chapman S., 1978, ApJS, 37, 169

Green S., Thaddeus P., 1976, ApJ, 205, 766

Guélin M., Zylka R., Mezger P. G., Haslam C. G. T., Kreysa E., 1995, A&A, 298, L29

Güsten R., 1989, in Morris M., ed., Proc. IAU Symp. 136, The Center of the Galaxy No. 136, Gas and dust in the inner few degrees of the galaxy (review). Kluwer, Dordrecht, pp 89–106

Gwinn C. R., 2001, ApJ, 561, 815

Habing H. J., 1968, Bull. Astron. Inst. Netherlands, 19, 421

Hartmann J., 1904, ApJ, 19, 268

Hartquist T. W., Falle S. A. E. G., Williams D. A., 2003, Ap&SS, 288, 369

Heger M. L., 1919, Lick Observatory Bulletin, 10, 59

Heikkilä A., Johansson L. E. B., Olofsson H., 1999, A&A, 344, 817

Helfer T. T., Thornley M. D., Regan M. W., Wong T., Sheth K., Vogel S. N., Blitz L., Bock D. C.-J., 2003, ApJS, 145, 259

Herbst E., Leung C. M., 1989, ApJS, 69, 271

Ho L. C., Filippenko A. V., Sargent W. L. W., 1997, ApJS, 112, 315

Hobbs L. M., Ferlet R., Welty D. E., Wallerstein G., 1991, ApJ, 378, 586

Hollenbach D. J., McKee C. F., 1979, ApJS, 41, 555

Hollenbach D. J., Salpeter E. E., 1970, J. Chem. Phys., 53, 79

Hollenbach D. J., Salpeter E. E., 1971, ApJ, 163, 155

Hollenbach D. J., Takahashi T., Tielens A. G. G. M., 1991, ApJ, 377, 192

Hollenbach D. J., Tielens A. G. G. M., 1999, Reviews of Modern Physics, 71, 173

Hollenbach D. J., Werner M. W., Salpeter E. E., 1971, ApJ, 163, 165

Israel F. P., 1997, A&A, 328, 471

Israel F. P., 2005, A&A, 438, 855

Israel F. P., Baas F., 2001, A&A, 371, 433

Israel F. P., Baas F., 2002, A&A, 383, 82

Israel F. P., Baas F., 2003, A&A, 404, 495

Israel F. P., Tilanus R. P. J., Baas F., 2006, A&A, 445, 907

Jansen D. J., van Dishoeck E. F., Black J. H., Spaans M., Sosin C., 1995, A&A, 302, 223

Jura M., 1974, ApJ, 191, 375

Kalberla P. M. W., Kerp J., Haud U., 2000, in Combes F., Pineau des Forêts G., eds, Molecular Hydrogen in Space The galactic dark matter halo: Is it H_2?. Cambridge University Press, Cambridge, pp 297–300

Kamp I., Bertoldi F., 2000, A&A, 353, 276

Kamp I., van Zadelhoff G.-J., 2001, A&A, 373, 641

Kaufman M. J., Wolfire M. G., Hollenbach D. J., Luhman M. L., 1999, ApJ, 527, 795

Kemp S. N., Bates B., Lyons M. A., 1993, A&A, 278, 542

Kennicutt R. C., 1989, ApJ, 344, 685

Knaap H. F. P., van den Meijdenberg C. J. N., Beenakker J. J. M., van de Hulst H. C., 1966, Bull. Astron. Inst. Netherlands, 18, 256

Knauth D. C., Andersson B.-G., McCandliss S. R., Moos H. W., 2003, ApJ, 596, L51

Kramer C., Mookerjea B., Bayet E., García-Burillo S., Gerin M., Israel F. P., Stutzki J., Wouterloot J. G. A., 2005, A&A, 441, 961

Langer G. E., Prosser C. F., Sneden C., 1990, AJ, 100, 216

Lauroesch J. T., Meyer D. M., 1999, ApJ, 519, L181

Lauroesch J. T., Meyer D. M., Blades J. C., 2000, ApJ, 543, L43

Lawrence A., 2001, MNRAS, 323, 147

Le Bourlot J., Pineau des Forêts G., Roueff E., Flower D. R., 1993a, A&A, 267, 233

Le Bourlot J., Pineau des Forêts G., Roueff E., 1993b, in Alloin D., Stasinska G., eds, Proc. 3rd DAEC Workshop, The Feedback of Chemical Evolution on the Stellar Content of Galaxies No. 3, Sensitivity of the co/h2 ratio on the physical conditions in external galaxies. Observatoire de Paris, Paris, pp 142–146

Le Petit F., Nehmé C., Le Bourlot J., Roueff E., 2006, ApJS, 164, 506

Le Petit F., Roueff E., Le Bourlot J., 2002, A&A, 390, 369

Le Teuff Y. H., Millar T. J., Markwick A. J., 2000, A&AS, 146, 157

Lee H.-H., Herbst E., Pineau des Forêts G., Roueff E., Le Bourlot J., 1996, A&A, 311, 690

Leitherer C., Schaerer D., Goldader J. D., Delgado R. M. G., Robert C., Kune D. F., de Mello D. F., Devost D., Heckman T. M., 1999, ApJS, 123, 3

Lequeux J., Peimbert M., Rayo J. F., Serrano A., Torres-Peimbert S., 1979, A&A, 80, 155

Liszt H. S., Lucas R., 1998, A&A, 339, 561

Liszt H., Lucas R., 2000, A&A, 355, 333

Lloyd C., 2003, in Metcalfe L., Salama A., Peschke S. B., Kessler M. F., eds, The Calibration Legacy of the ISO Mission ESA SP-481, The ISO LWS beam profile. European Space Agency, Noordwijk, pp 399–402

Lucas R., Liszt H. S., 1993, A&A, 276, L33

Lundgren A. A., Wiklind T., Olofsson H., Rydbeck G., 2004, A&A, 413, 505

Madau P., Pozzetti L., Dickinson M., 1998, ApJ, 498, 106

Madden S. C., 2002, Ap&SS, 281, 247

Madden S. C., Poglitsch A., Geis N., Stacey G. J., Townes C. H., 1997, ApJ, 483, 200

Magnani L., Chastain R. J., Kim H. C., Hartmann D., Truong A. T., Thaddeus P., 2003, ApJ, 586, 1111

Malhotra S., Kaufman M. J., Hollenbach D., Helou G., Rubin R. H., Brauher J., Dale D., Lu N. Y., Lord S., Stacey G., Contursi A., Hunter D. A., Dinerstein H., 2001, ApJ, 561, 766

Maloney P., 1990, in Thronson Jr. H. A., Shull J. M., eds, Proc. 2nd Teton Conf., The Interstellar Medium in Galaxies Vol. 161, Mass determinations from co observations. Kluwer, Dordrecht, pp 493–523

Maloney P., Black J. H., 1988, ApJ, 325, 389

Mao R. Q., Henkel C., Schulz A., Zielinsky M., Mauersberger R., Störzer H., Wilson T. L., Gensheimer P., 2000, A&A, 358, 433

Marscher A. P., Moore E. M., Bania T. M., 1993, ApJ, 419, L101

Martin P. G., Mandy M. E., 1995, ApJ, 455, L89

Martin P. G., Schwarz D. H., Mandy M. E., 1996, ApJ, 461, 265

Mathis J. S., 1990, ARA&A, 28, 37

Mathis J. S., Rumpl W., Nordsieck K. H., 1977, ApJ, 217, 425

Matsushita S., Kohno K., Vila-Vilaro B., Tosaki T., Kawabe R., 1998, ApJ, 495, 267

Matsushita S., Sakamoto K., Kuo C.-Y., Hsieh P.-Y., Dinh-V-Trung Mao R.-Q., Iono D., Peck A. B., Wiedner M. C., Liu S.-Y., Ohashi N., Lim J., 2004, ApJ, 616, L55

Mauersberger R., Henkel C., Walsh W., Schulz A., 1999, A&A, 341, 256

McCray R., Kafatos M., 1987, ApJ, 317, 190

McDowell M. R. C., 1961, The Observatory, 81, 240

McKellar A., 1940, PASP, 52, 187

Meijerink R., Spaans M., 2005, A&A, 436, 397

Melnick G., Gull G. E., Harwit M., 1979, ApJ, 227, L29

Meyer D. M., Blades J. C., 1996, ApJ, 464, L179

Meyer D. M., Jura M., Cardelli J. A., 1998, ApJ, 493, 222

Millar T. J., Farquhar P. R. A., Willacy K., 1997, A&AS, 121, 139

Moore E. M., Marscher A. P., 1995, ApJ, 452, 671

Morata O., Girart J. M., Estalella R., 2005, A&A, 435, 113

Morris M., Lo K. Y., 1978, ApJ, 223, 803

Nakai N., Kuno N., Handa T., Sofue Y., 1994, PASJ, 46, 527

Negishi T., Onaka T., Chan K.-W., Roellig T. L., 2001, A&A, 375, 566

Nieten C., Dumke M., Beck R., Wielebinski R., 1999, A&A, 347, L5

Nikola T., Geis N., Herrmann F., Madden S. C., Poglitsch A., Stacey G. J., Townes C. H., 2001, ApJ, 561, 203

Noordermeer E., van der Hulst J. M., Sancisi R., Swaters R. A., van Albada T. S., 2005, A&A, 442, 137

Osterbrock D. E., 1974, Astrophysics of Gaseous Nebulae. W. H. Freeman and Co., San Francisco

Osterbrock D. E., 1989, Astrophysics of Gaseous Nebulae and Active Galactic Nuclei. University Science Books, California

Papadopoulos P. P., Thi W.-F., Viti S., 2002, ApJ, 579, 270

Peng R., Langer W. D., Velusamy T., Kuiper T. B. H., Levin S., 1998, ApJ, 497, 842

Pety J., Falgarone É., 2000, A&A, 356, 279

Pfenniger D., Combes F., Martinet L., 1994, A&A, 285, 79

Prasad S. S., Huntress W. T., 1980, ApJS, 43, 1

Press W. H., Teukolsky S. A., Vetterling W. T., Flannery B. P., 1992, Numerical recipes in Fortran. The art of scientific computing, 2nd edn. Cambridge University Press, Cambridge

Price R. J., Crawford I. A., Barlow M. J., 2000, MNRAS, 312, L43

Rawlings J. M. C., Yates J. A., 2001, MNRAS, 326, 1423

Regan M. W., Thornley M. D., Helfer T. T., Sheth K., Wong T., Vogel S. N., Blitz L., Bock D. C.-J., 2001, ApJ, 561, 218

Richardson K. M., Wolfendale A. W., 1988, A&A, 203, 289

Röllig M., Abel N. P., Bell T. A., Bensch F., Black J. H., Ferland G. J., Jonkheid B., Kamp I., Kaufman M. J., Le Bourlot J., Le Petit F., Meijerink R., Morata O., Ossenkopf V., Roueff E., 2006a, A&A, submitted

Röllig M., Ossenkopf V., Jeyakumar S., Stutzki J., Sternberg A., 2006b, A&A, 451, 917

Rollinde E., Boissé P., Federman S. R., Pan K., 2003, A&A, 401, 215

Rosolowsky E., Blitz L., 2005, ApJ, 623, 826

Rosolowsky E., Engargiola G., Plambeck R., Blitz L., 2003, ApJ, 599, 258

Rubio M., Lequeux J., Boulanger F., 1993, A&A, 271, 9

Russell R. W., Melnick G., Gull G. E., Harwit M., 1980, ApJ, 240, L99

Russell R. W., Melnick G., Smyers S. D., Kurtz N. T., Gosnell T. R., Harwit M., Werner M. W., 1981, ApJ, 250, L35

Sakamoto K., Okumura S. K., Ishizuki S., Scoville N. Z., 1999, ApJS, 124, 403

Sakamoto S., 1996, ApJ, 462, 215

Sakamoto S., 1999, ApJ, 523, 701

Sandage A., Tammann G. A., 1975, ApJ, 196, 313

Sargent W. L. W., Young P. J., Boksenberg A., Carswell R. F., Whelan J. A. J., 1979, ApJ, 230, 49

Savage B. D., Mathis J. S., 1979, ARA&A, 17, 73

Savage B. D., Sembach K. R., 1996, ARA&A, 34, 279

Schilke P., Carlstrom J. E., Keene J., Phillips T. G., 1993, ApJ, 417, L67

Schinnerer E., Böker T., Emsellem E., Lisenfeld U., 2006, ApJ, 649, 181

Schwering P. B. W., Israel F. P., 1989, A&AS, 79, 79

Scoville N. Z., Yun M. S., Clemens D. P., Sanders D. B., Waller W. H., 1987, ApJS, 63, 821

Seaquist E. R., Frayer D. T., 2000, ApJ, 540, 765

Seaquist E. R., Lee S. W., Moriarty-Schieven G. H., 2006, ApJ, 638, 148

Shaw G., Ferland G. J., Abel N. P., Stancil P. C., van Hoof P. A. M., 2005, ApJ, 624, 794

Smith A. M., 1973, ApJ, 179, L11

Smith P. A., Brand P. W. J. L., Mountain C. M., Puxley P. J., Nakai N., 1991, MNRAS, 252, 6P

Smoker J. V., Keenan F. P., Polatidis A. G., Mooney C. J., Lehner N., Rolleston W. R. J., 2000, A&A, 363, 451

Snow T. P., Rachford B. L., Figoski L., 2002, ApJ, 573, 662

Sodroski T. J., Odegard N., Dwek E., Hauser M. G., Franz B. A., Freedman I., Kelsall T., Wall W. F., Berriman G. B., Odenwald S. F., Bennett C., Reach W. T., Weiland J. L., 1995, ApJ, 452, 262

Sofia U. J., Cardelli J. A., Guerin K. P., Meyer D. M., 1997, ApJ, 482, L105

Solomon P. M., Rivolo A. R., Barrett J., Yahil A., 1987, ApJ, 319, 730

Sorai K., Nakai N., Kuno N., Nishiyama K., Hasegawa T., 2000, PASJ, 52, 785

Spitzer L., 1948, ApJ, 107, 6

Spitzer L., Drake J. F., Jenkins E. B., Morton D. C., Rogerson J. B., York D. G., 1973, ApJ, 181, L116

Spitzer L., Jenkins E. B., 1975, ARA&A, 13, 133

Stacey G. J., Jaffe D. T., Geis N., Genzel R., Harris A. I., Poglitsch A., Stutzki J., Townes C. H., 1993, ApJ, 404, 219

Stanimirović S., Weisberg J. M., Hedden A., Devine K. E., Green J. T., 2003, ApJ, 598, L23

Stecher T. P., Williams D. A., 1967, ApJ, 149, L29

Sternberg A., Dalgarno A., 1989, ApJ, 338, 197

Sternberg A., Dalgarno A., 1995, ApJS, 99, 565

Sternberg A., McKee C. F., Wolfire M. G., 2002, ApJS, 143, 419

Storey J. W. V., Watson D. M., Townes C. H., 1979, ApJ, 233, 109

Störzer H., Stutzki J., Sternberg A., 1996, A&A, 310, 592

Strong A. W., Mattox J. R., 1996, A&A, 308, L21

Suchkov A., Allen R. J., Heckman T. M., 1993, ApJ, 413, 542

Sutton E. C., Phillips T. G., Masson C. R., 1983, ApJ, 275, L49

Swings P., Rosenfeld L., 1937, ApJ, 86, 483

Taylor S. D., Hartquist T. W., Williams D. A., 1993, MNRAS, 264, 929

Telesco C. M., Joy M., Dietz K., Decher R., Campins H., 1991, ApJ, 369, 135

Tielens A. G. G. M., Hollenbach D., 1985a, ApJ, 291, 722

Tielens A. G. G. M., Hollenbach D., 1985b, ApJ, 291, 747

Tully R. B., 1988, Nearby Galaxies Catalog. Cambridge University Press, Cambridge

van de Hulst H. C., 1948, in Centennial Symposia No. 7 in Harvard Observatory Monographs, Evolution and physics of solid particles. Harvard Observatory, Cambridge, MA, p. 73

van Dishoeck E. F., 1984, PhD thesis, Univ. Leiden

van Dishoeck E. F., Black J. H., 1986, ApJS, 62, 109

van Dishoeck E. F., Black J. H., 1988, ApJ, 334, 771

Vermeij R., van der Hulst J. M., 2002, A&A, 391, 1081

Wakelam V., Castets A., Ceccarelli C., Lefloch B., Caux E., Pagani L., 2004, A&A, 413, 609

Walker M., Wardle M., 1998, ApJ, 498, L125

Walter F., Brinks E., de Blok W. J. G., Thornley M. D., Kennicutt R. C., 2005, in Braun R., ed., Extra-Planar Gas Vol. 331 of ASP Conf. Ser., First results from THINGS: The HI Nearby Galaxy Survey. Astronomical Society of the Pacific, San Francisco, p. 269

Weaver R., McCray R., Castor J., Shapiro P., Moore R., 1977, ApJ, 218, 377

Weliachew L., Casoli F., Combes F., 1988, A&A, 199, 29

Welty D. E., Fitzpatrick E. L., 2001, ApJ, 551, L175

Welty D. E., Fowler J. R., 1992, ApJ, 393, 193

Westerlund B. E., 1990, A&A Rev., 2, 29

White G. J., Ellison B., Claude S., Dent W. R. F., Matheson D. N., 1994, A&A, 284, L23

Wild W., Harris A. I., Eckart A., Genzel R., Graf U. U., Jackson J. M., Russell A. P. G., Stutzki J., 1992, A&A, 265, 447

Williams J. P., Blitz L., Stark A. A., 1995, ApJ, 451, 252

Wilson C. D., 1995, ApJ, 448, L97

Wilson C. D., Combes F., 1998, A&A, 330, 63

Wilson C. D., Olofsson A. O. H., Pagani L., Booth R. S., Frisk U., Hjalmarson Å., Olberg M., Sandqvist A., 2005, A&A, 433, L5

Wolfire M. G., Hollenbach D., Tielens A. G. G. M., 1989, ApJ, 344, 770

Wolfire M. G., Hollenbach D., Tielens A. G. G. M., 1993, ApJ, 402, 195

Wolfire M. G., McKee C. F., Hollenbach D. J., Tielens A. G. G. M., 2003, ApJ, 587, 278

Wolfire M. G., Tielens A. G. G. M., Hollenbach D., 1990, ApJ, 358, 116

Yao L., Bell T. A., Viti S., Yates J. A., Seaquist E. R., 2006, ApJ, 636, 881

Young J. S., Scoville N. Z., 1991, ARA&A, 29, 581

Zaritsky D., Kennicutt J., Huchra J. P., 1994, ApJ, 420, 87

Zwaan M. A., Prochaska J. X., 2006, ApJ, 643, 675